MODELLING ELASTICITY-RELATED EFFECTS IN INTERFACES

PHASE FIELD CRYSTAL STUDIES OF

STRAIN-MEDIATED EFFECTS IN THE THERMODYNAMICS

AND KINETICS OF INTERFACES

By

JONATHAN STOLLE

B.Eng Engineering Physics, McMaster University
M.Sc Physics, McGill University

A Thesis
Submitted to the School of Graduate Studies
in Partial Fulfilment of the Requirements
for the Degree
Doctor of Philosophy

McMaster University

DOCTOR OF PHILOSOPHY (2013) (Physics and Astronomy)	McMaster University Hamilton, Ontario
TITLE:	Phase Field Crystal Studies of Strain-Mediated Effects in the Thermodynamics and Kinetics of Interfaces
AUTHOR:	Jonathan Stolle, B.Eng. (McMaster University), M.Sc. (McGill University)
SUPERVISOR:	Nikolas Provatas
NUMBER OF PAGES:	xii,117

ABSTRACT

In this dissertation, the Phase Field Crystal (PFC) Method is used to study a number of problems in which interfaces and elastic effects play important roles in alloys. In particular, the three topics covered in this work are grain boundary thermodynamics in alloys, dislocation-mediated formation of clusters in binary and ternary alloys, and solutal effects in explosive crystallization. Physical phenomena associated with grain boundaries, such as Read-Shockley-like behaviour and Gibbs adsorption theorem, were shown to be accurately captured in both PFC- and XPFC-type models. In fact, a connection between the solute segregation behaviour and physical properties of the system—such as energy of mixing, mismatch, and undercooling—were shown. Also, grain boundary premelting was investigated. It was shown how solute can change the disjoining potential of a grain boundary and a mechanism for hysteresis in grain boundary premelting was discussed. Regarding the phenomenon of cluster formation, a general coexistence approach and a nucleation-like approach were used to describe the mechanism consistently with observations; the process is facilitated by lowering the energy increase associated with it. The final phenomenon studied was explosive crystallization. It was shown that the temperature oscillations due to unsteady motion of an interface could be captured with PFC-type models and that this behaviour leaves patterns, such as solute traces, in the material. The versatility of this PFC formalism was demonstrated by capturing the underlying physics and elucidating the role of misfit strain in altering interface oscillations during explosive crystallization. Finally, it was demonstrated in all projects how PFC model parameters relate to coarse-grained material properties, thereby connecting these phenomena on larger scales to atomistic-scale properties.

ACKNOWLEDGEMENTS

Recalling the thought, "I would maintain that thanks are the highest form of thought, and that gratitude is happiness doubled by wonder," by G. K. Chesterton, I would like to take the time to thank the many people who contributed to the completion of the dissertation and my PhD studies. To start, I would like to thank my supervisor, Nikolas Provatas, who accepted me into his research group as a research associate when I was struggling to finish my master's thesis. Nearly 5 years later, I have nearly completed my doctoral studies with him thanks to his willingness to give me a chance in his research group, his support, and his guidance along the way. Throughout the course of the studies, thanks to him I was introduced to many interesting ideas, some of which we chose to investigate together and solve with the help of his academic advice.

I would also like to thank current and past members of the research group, commonly known as the Advanced Centre for Serious Research (ASCR), including: M. G.; P.G.; M.A.; S.G. (maybe); D.M.; N.F.; R.A.; H.A.; E.R., for work on premelting in PFC; T.P.; J.B.; V.F., with whom I collaborated productively; the McGill crowd (G.K.,H.A.,B.J.,M.S.); and two members, H.H. and N.O-O., who were at roughly the same stage of studies, with whom I was able to work, and who were able to identify with being in a PhD program. You all provided great support during the couse of my studies including but not limited to academic collaboration and being friends—the lab coats, basement office, and parties. I would also like to thank Prof. Jeff Hoyt for his insights into materials science and his advice as a supervisory committee member, and members of his research group, Team Hoyt, for helping make Computational Materials Science at McMaster a great place to be.

There are many people I would like to thank who helped with many things pertaining to graduate studies. First I would to thank the other members of my supervisory committee, Profs. A.-C. Shi and B. Gaulin. In the Physics and Astronomy department I would also like to thank Prof. Dalnoki-Veress, Prof. Chen, Hua, Tina, Mara, Cheryl, Rosemary, Liz, Prof. McKay, Profs. Haugen and Mascher (from Eng Phys), Prof Hughes, Alex, Andy, Jake, and for help with various aspects of my program, as well as many others including fellow graduate students, who helped make me feel welcome in the department. I would also like to thank Ed, Nanci, Diana, and Jane in the Materials Science and Engineering Department and members in the McGill Physics Department for their help.

There were many others with whom I collaborated outside of the university including, but not limited to Profs K. Elder and Z.-F. Huang, whose insights into a number of problems I encountered were most welcome. I would also like to thank NSERC and McMaster University for financial support. For technical support I would like to thank RHPCS, and Compute Canada (especially Clumeq, now part of Calcul Quebec, Sharcnet, Westgrid, Scinet) for technical support.

Because work is only just one part of life, I would also like to thank others who helped make my life more balanced including my friends (especially, J.-I. S., D.L., M.M., M.C., R.S.) and those with whom I particpated in a wide variety of activities including intramurals, LTS, GCM (LW), MACSA and NSS (PBART), and those who helped with publishing the graduate student newsletter, Condensed Matter. On this note, I would like to in particular thank my girlfriend Sabrina for her love, friendship, and support over the last few months of writing my thesis and who it has been wonderful to meet (GSDHDGDL). I look forward to seeing what the future brings.

Finally, I would like to all of my family for their love and support throughout my studies and in life in general. I would like to thank in particular my parents, who raised me and are always there for me, and my brother, who though at times a nuissance, has also done a fair bit to help too, and my sister.

There are also many other people who helped me these past 5 years who I have not listed, but your help is still very much appreciated. These last few years have been part of a fulfilling journey and it is just one step in my life (and career path). Where life will take me, I do not know, but with the current direction in my life, this calls to mind a journal entry by Lewis Fry Richardson: "I would like to spend the first half of my life under the strict discipline of physics, and afterwards to apply that training to researches on living things."

Contents

List of Figures

List of Contributions

1. Jonathan Stolle, and Nikolas Provatas. Characterizing Solute Segregation and Grain Boundary Energy in a Binary Alloy Phase Field Crystal Model. *In Press in Computational Materials Science*, 2013.

2. Tara Power, Elizabeth Rowan, Jonathan Stolle, Jeff Hoyt, and Nikolas Provatas. A Monte Carlo and PFC study of Grain Boundary Premelting: a comparison. *Draft in Progress, 2013.*

3. Nana Ofori-Opoku, Jonathan Stolle, Zhi-Feng Huang, and Nikolas Provatas. Amplitude models for structural transformations derived from structural phase-field-crystal models. *Phys. Rev. B.*, 88: 104106 2013.

4. Vahid Fallah, Nana Ofori-Opoku, Jonathan Stolle, Nikolas Provatas, and Shahrzad Esmaeili. Simulation of early-stage clustering in ternary metal alloys using the phase field crystal method. *Acta Materialia*, 61:3653-3666, 2013.

5. Vahid Fallah, Jonathan Stolle, Nana Ofori-Opoku, Shahrzad Esmaeili, and Nikolas Provatas. Phase-field crystal modeling of early stage clustering and precipitation in metal alloys. *Phys. Rev. B*, 86:134112, 2012.

Author's Contribution

All of the work presented in this dissertation relates to significant contributions made by me in the development of each of the topics. On the topic of grain boundary thermodynamics, I was the primary contributor to the study of the energetics and solute segregation properties of grain boundaries in binary alloys. I wrote the first draft of 1 and revised it with the advice of my coauthor (and supervisor) and referees of it. I also developed the model used for the work on grain boundary premelting, provided guidance and worked on the theoretical analysis of the problem, some of which will be included in 2. Regarding the project on the formation of clusters, I developed various theoretical models used to understand the problem and provided guidance to the main investigator in the simulations. In reference 5, I contributed the framework for a phase-coexistence argument for solute-rich cluster regions in the matrix parent phase and the framework for a nucleation-like argument for the effect dislocations on the formation of clusters, and proofread the manuscript. In reference 4, I generalized the theoretical analyses to a ternary alloy and proofread the manuscript. Finally, all aspects of the work on explosive crystallization was done by me under the guidance of my supervisor. In terms of my work on amplitude models, the three main topics presented in this thesis use aspects of it. In terms of my contribution to 3, I used an alternate approach to developing the coarse-grained amplitude models, which helped with a broader understanding of the problem. I also helped proofread the manuscript.

Chapter 1

Introduction

1.1 Overview

In condensed matter physics problems, interfaces can play an important role in determining the physical behaviour and properties of materials. It is well-known that they provide an energy barrier for nucleation, interact with other defects in the material, influence electrical conductivity, and can control how a reaction front proceeds, depending on the processes happening at the interface. In many systems, interfacial widths are on the order of nanometers, while the processes occur on diffusive time scales. For these time and length scales, the Phase Field Crystal (PFC) formalism is appropriate.

As well, stress can affect a material in such a way that it modulates or even strongly changes how physical features manifest themselves. Some elastic effects on interfaces are easily described on a mesoscopic or even macroscopic scale. These include the Asaro-Tiller-Grinfeld instability [1, 19] and stress-related solute diffusion and segregation in a a material. However, if the stress fields result from the location of individual atoms and if the effects of the individual atoms do not average out on a larger scale, then the atomisitc details must be studied. The PFC formalism also naturally incorporates elasticity in solids, so it is also a good candidate to study elastic effects in interfaces.

The thesis is organized as follows. In the rest of the introductory chapter, the three topics studied in this thesis, relating to the above-mentioned physics are introduced; these topics are the thermodynaimcs of grain boundaries, the formation of clusters in early stage precipitation, and explosive crystallization. In Chapter 2, the PFC formalism is introduced and described, which is the main approach to studying the physical problems in this thesis. Chapter 3 presents new results on grain boundary thermodynamics in PFC-type models of alloys, including grain boundary premelting. In Chapter 4, defect-mediated cluster formation in a PFC-type formalism is demonstrated. In Chapter 5, a PFC-type model is developed and its coarse-grained analogue is used to study explosive crystallization. The conclusions are found in Chapter 6.

1.2 Interfaces in Alloys

The first area of physics that is presented in this thesis concerns interfacial thermodynamics. Interfaces are an important part of the microstructure of materials, along with dislocations and vacancies, which make important contributions to the material properties. These defects also contribute an excess of free energy to the material. As the material tends towards equilibrium by reducing its free energy, the amount of defects changes, meaning that the material properties change as well. The first focus of this thesis is on a particular kind of interface, the grain boundary.

Grain boundaries, which have been studied since at least the early 20^{th} century [20], are among

the most important defects in metals. They provide sinks and sources for dislocations, sites favourable for nucleation of new phases, and their distribution, energy, and composition affect various material properties, such as material strength and electrical conductivity. In alloys, the presence of solute can change how the above effects manifest themselves, such as grain boundary energy, which is changed by solute segregating to them [21, 22, 23, 24, 25]. As well, the presence of solute provides additional degrees of freedom, which can allow new phenomena to occur. One of the new phenomena which occurs is solute drag, in which the grain boundary mobility is reduced in the material due to the presence of solute [22, 26, 27]. Another material property strongly affected by solute segregation is grain boundary wetting [22, 28, 29, 3].

Two of the most commonly studied grain boundary properties are grain boundary energy and solute distribution [22, 21], which will be focused on this thesis. Others, such as excess grain boundary volume are well-studied as well [30]. Grain boundary energy has been well-studied in pure materials [31, 32, 33] and alloys [21, 33]. To understand these properties, early theories postulated that the regions between grain boundaries was some sort of amorphous cement between the grains [20, 32]. A big advance in the quantitative understanding of grain boundary energy was made when Read and Shockley derived a dislocation-model of grain boundaries [33]. The Read-Shockley relation, which first appeared in Ref. [33], has been verified experimentally for pure materials [31, 32] and dilute alloys [33]. It is not only useful for low angles (approximately less than 15°), its intended range of validity [31, 33], but for a much larger range of angles as well [31, 32, 33]. The Peierls-Nabarro and Van der Merwe models [22] and some simple geometric and thermodynamic models are quite popular as well [22, 24].

Computational studies have been used to complement theoretical and experimental grain boundary studies, as these methods can probe details that are not accessible to either of the other methods [22]. To study grain boundary energy in pure materials, molecular dynamics (MD) [34], lattice statics (LS) [35], and a number of density functional theory (DFT) and other atomistic approaches have also been used [22]. To study grain boundary segregation, computational approaches have been applied as well. These include phase field (PF) models [3, 36], monte carlo (MC) simulations [23, 37], and molecular dynamics (MD) [23, 25].

The phase-field crystal (PFC) model is of particular interest to studying grain boundary properties. Because it is an atomistic-scale model, it naturally includes elasticity and atomistic defects, which can be important to resolve when considering finer details of premelting, such as the structure of dislocation cores [1, 38]. Also, because it is a temporarly-coarse-grained model, it operates on diffusive time scales, allowing simulations to be done of thermodynamic processes and relatively slow kinetic processes [1]. It has already provided substantial insight into studying grain boundary energy and excess density in pure materials [1, 38, 39, 40]. This model has also been recently applied to grain boundary properties in alloys in the work of [16] and [41].

1.2.1 Thermodynamics of Interfaces

In studying the thermodynamics of interfaces, it is important to be able to define quantities which accurately describe the relevant physical properties of the system. The interfacial properties are well-defined in terms of excess quantities, which was first discovered by Gibbs; roughly speaking, an excess quantity is how much energy/concentration/volume the interface has compared to the bulk state of the system [22]. The most physical of these is interfacial energy, which must be a constant for a given system because of the first law of thermodynamics. The other excess quantities, depend on how the thermodynamics of the system is analysed; among these quantities are excess concentration and excess volume. Cahn pioneered an approach for defining the excess quantities. In his approach, the Gibbs-Duhem relations are used to describe the material on either side of the interface and for the interface:

$$Ad\gamma = -S^{gb}dT + V^{gb}dp - \sum_i N_i^{gb} d\mu_i$$

$$\begin{aligned} 0 &= -S^1 dT + V^1 dp - \sum_i N_i^1 d\mu_i \\ 0 &= -S^2 dT + V^2 dp - \sum_i N_i^2 d\mu_i \end{aligned} \tag{1.1}$$

where A is the area of the interface, γ is the interfacial surface tension, S is entropy, T is temperature, V is volume, p is pressure, μ_i are the chemical potentials corresponding to eachred atomic species, of which there are N_i, where ^{gb} refers to a volumetric thermodynamic quantities times the surface area of the interface, and ^{i} refers to the amount of material in each phase i, where $i = 1, 2$ [22]. There are 3 equations and 5 unknown differential quantities, so choosing to use the N_i^j as reference quantities, the above equations can be simplified into the following equation:

$$d\gamma = -S^{ex} dT + V^{ex} dp \tag{1.2}$$

where $X^{ex} = X^{gb} - X^1/N_1^1 N_1^{gb} - (N_2^{gb} - N_2^1/N_1^1 N_1^{gb})(X^2 - X^1/N_1^1 N_1^2)/(N_2^2 - N_2^1/N_1^1 N_1^2)$ for all extensive thermodynamic quantities X. From Eq. 1.2, Gibbs adsorption theorem in differential form can be derived. For example, at constant pressure:

$$\left(\frac{\partial \gamma}{\partial T}\right)_p = -S^{ex} \tag{1.3}$$

Eq. 1.3 can be integrated to find γ. γ can be found in an equivalent way by applying a Gibbs' dividing surface—an imaginary surface through which one states that material 1 is one side of it and material 2 on the other. Drawing the surface anywhere, the following is always true:

$$A\gamma = E^{xs} - S^{xs} T + V^{xs} p - \sum \mu_i N_i \tag{1.4}$$

where E refers to the internal energy of the system, $X^{xs} = X - (X_1 + X_2)$, where X is any macroscopic quantity defined in the above equation [22].

Grain boundaries are treated exactly the same as other interfaces. They can also easily be described by Gibbs' adsorption theorem. In fact, when both grains are thermodynamically equivalent, then there is only 1 phase present in Eqs.1.1. In this instance, Eq. 1.2 can be written as:

$$d\gamma_{gb} = -S^{ex} dT + V^{ex} dp - N_2^{ex} d\mu_2 \tag{1.5}$$

where $X^{ex} = X^{gb} - X^1/N_1^1 N_1^{gb}$. Eq.1.5 can be simplified into the Gibbs adsorption theorem, which is often written as follows because T and p are easily controlled thermodynamic parameters:

$$\left(\frac{\partial \gamma_{gb}}{\partial \mu_2}\right)_{T,p} = -N_2^{ex} \tag{1.6}$$

Similarly for Eq. 1.4, if we set $V^{xs} = 0$, then:

$$A\gamma_{gb} = E^{xs} - S^{xs} T - \sum_i \mu_i N_i \tag{1.7}$$

where $X^{xs} = X - X_1$, where X is any macroscopic quantity defined in the above equation. Many different combinations of thermodynamic variables can be chosen depending on what is convenient for the analysis. For example, instead of eliminating μ_1, p might be eliminated instead. Instead of Eq. 1.5, the following equation is gotten

$$d\gamma_{gb} = -S^{ex} dT - N_1^{ex} d\mu_1 - N_2^{ex} d\mu_2 \tag{1.8}$$

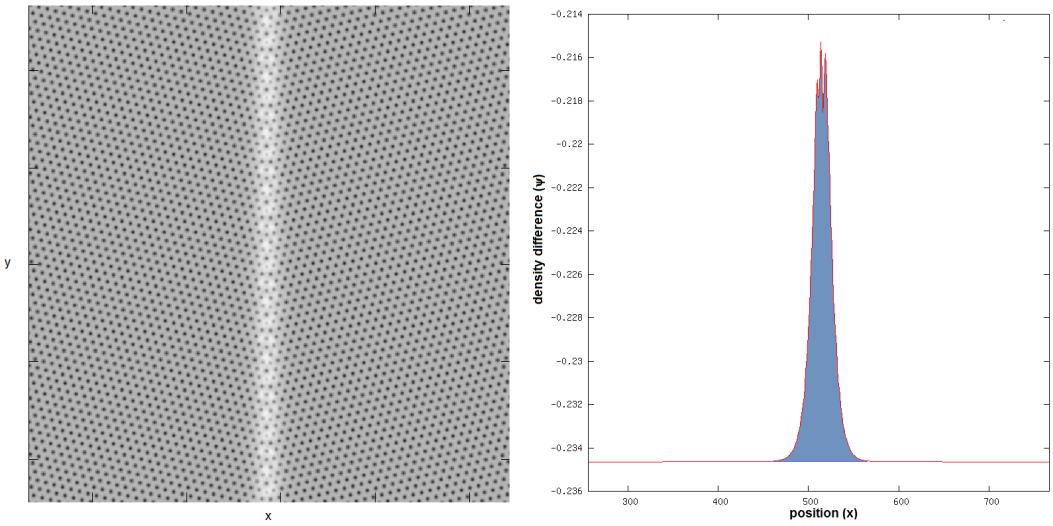

Figure 1.1: Normalized density difference field, $\psi = (\rho_2 - \rho_1)/\rho_0$, for a 2D grain boundary simulation *(left frame)* and averaged normalized density difference $\bar{\psi} = \int \psi dy$ with position x *(right frame)*. The shaded area in the right frame is the excess Γ_{ψ}^{ex} for the grain boundary, if total density, $\rho_1 + \rho_2$, is constant everywhere. ρ_1 is the volume density of species 1 and ρ_2 is the volume density of species 2.

where $X^{ex} = X^{gb} - X^1/V_1^1 V_1^{gb}$. From Eq. 1.8, it can be deduced that

$$\left(\frac{\partial \gamma_{gb}}{\partial \mu_z}\right)_{T,\mu_y} = -N_z^{ex} \tag{1.9}$$

where N_y and N_z have a functional dependence on N_1 and N_2—e.g., a linear combination such as $N_y = N_1 + N_2$ and $N_z = N_1 - N_2$. An illustration of an excess quantity in a grain boundary if is given in Fig. 1.1.

For a given material, grain boundary energy follows a distinct relation depending on the misorientation (a description of how the crystals are oriented with respect to each other) and inclination (a quantification of which interfaces of the crystals meet at the boundary) of the two grains with respect to each other [22]. For low angle grain boundaries, which can be described as an array of dislocations, the Read-Shockley relation describes the grain boundary energy γ_{gb} for a pure material in terms of the material properties and misorientation, θ:

$$\gamma_{gb} = E_0 \theta (A - \ln(\theta)) \tag{1.10}$$

where E_0 is related to the elastic constants and Burgers vector of the dislocation, and A is related to the core energy [33]. Curiously, this relation can be fit to higher angles as well, which is useful for studying many systems [1]. In fact, this approach was originally fit to dilute alloy data by Ref. [33] and this form can be reasonably fit to other datasets. In Fig. 1.2, we show a number of grain boundary data energy datasets fit to the Read-Shockley reation from Ref. [1].

1.2.2 Grain boundary Premelting

As mentioned above, grain boundaries provide a site for the nucleation of new phases. One instance in which this is important is grain boundary premelting—when at temperatures below the melting

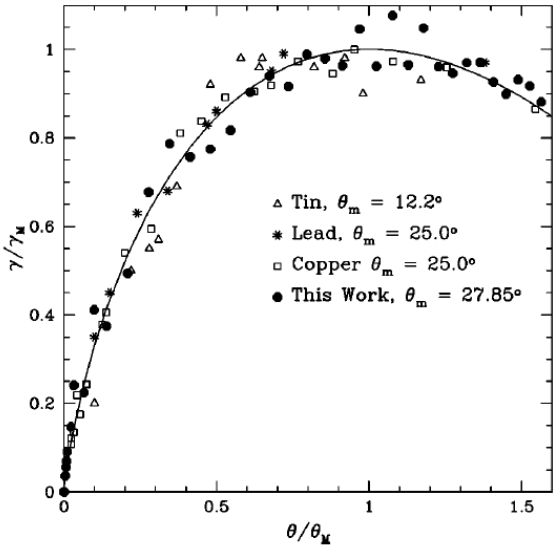

Figure 1.2: Normalized grain boundary energy γ_{gb}/γ_m vs. normalized misorientation angle θ/θ_m for a number of different data sets, where γ_m is the maximum grain boundary energy and θ_m is the angle at which the maximum energy occurs. From Ref. [1]

point, a liquid layer forms at a grain boundary. This problem is of practical significance because of the phenomenon of hot-tearing. In hot tearing, a worked metal is deformed because it is unable to resist shear stresses at the grain boundary [38]. Examples of premelting in grain boundaries are given in Fig. 1.3.

Grain boundary premelting has been observed experimentally in both alloys and pure materials (for examples of these studies see, [22] and for more recent ones, see [28, 42, 43, 44]). For alloys, premelting can occur under a relatively wide range of conditions when compared with premelting in a pure material, which occurs only very close to the melting point, T_m (typically $\sim 0.999T_m$). Since the 1980's, computational studies have provided additional insights to the experimental studies. An early computational study of premelting was done by Kikuchi and Cahn, who demonstrated a logarithmic divergence in the thickness of the wetted layer [45]. This observation is consistent with observing premelting of pure materials in a very narrow range [22]. More recent investigations have included PF, MD, MC, and PFC approaches and combinations thereof.

Among the PF approaches, three in particular stand out: a study of the inverse problem by Rappaz et al [46], that of Mishin et al [29] and that of Wang et al [3]. From simple thermodynamics considerations, the sign of $\gamma_{gb} - 2\gamma_{sl}$, where γ_{sl} is the solid liquid surface tension, might be expected to give a good indication as to whether or not the grain boundary premelts [46]. If $\gamma_{gb} > 2\gamma_{sl}$, it might be expected that a dry (no liquid layer) grain boundary be less stable than a wetted one (repulsive grain boundary). If $\gamma_{gb} < 2\gamma_{sl}$, a dry boundary would be expected to be more stable. However, all three studies suggested that the physics was not so simple; in fact, Refs.[29, 3] found that a common scenario was for grain boundaries to be attractive at large distances (the material needs to be overheated to melt completely), but repuslive at small distances (that is, the grains resist closing completely). In the latter two papers, a hysteresis is even observed in the premelting behaviour for certain kinds of grain boundaries; at the same temperature interfaces of different liquid thickness can exist. In Ref [3], this effect is observed to be stronger in alloys, as is expected from the results of experiments, in which it is much easier to observe evidence of premelting in alloys than in pure materials [22]. However, there were 2 major limitations of the above-mentioned premelting studies. The studies were one-dimensional, meaning that the interfaces were assumed to be stable to

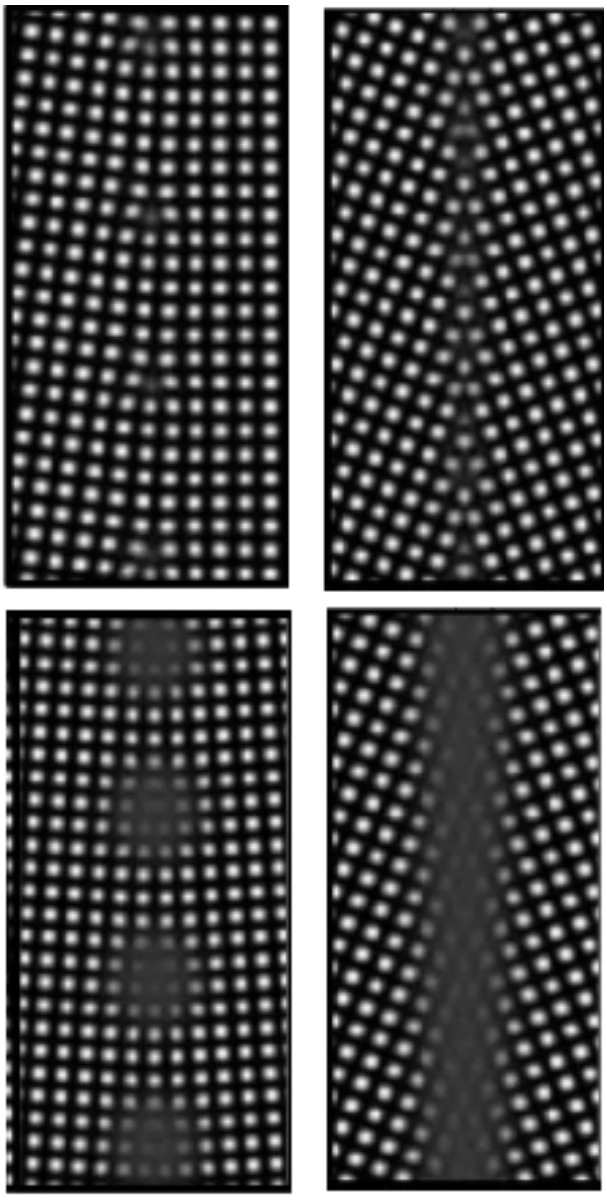

Figure 1.3: Top frames - Low angle grain boundary *(left)* and high angle grain boundary *(right)*. Bottom frames - Premelting of dislocations in low angle grain boundary *(left)* and premelted high angle grain boundary *(right)*. Adapted from Ref. [2]. The premelted dislocations do not completely prevent the material from resisting shear stresses, while the premelted high angle grain boundary can.

any perturbation, which might not be true as the solidifcation study of Ref. [46] shows that structure forms in the interface as crystals coalesce. Also, effects due to the discreteness of the interface structure cannot be easily taken into account in PF model.

To analyse atomistic structure of the interface, atomistic models such as LS, MD, and MC are needed. Shortly after the pioneering study of Ref. [45], molecular dynamics studies were applied to study premelting [47]. More recently, some MD studies were conducted by Hoyt et al [48, 49, 50] for premelting in pure Nickel, while Williams and Mishin did MC simulations for copper silver alloys [51]. It is important to note that some studies have been recently done where the results of MD have been compared to models of the relatively new PFC formalism [52, 53].

PFC studies of grain boundary premelting were conducted by Berry et al [2] and Mellenthin et al [38]. In the former study, the premelting behaviour of low-angle and high-angle boundaries were analysed. For low to intermediate angles, the dislocations in the boundary behaved as nucleation sites for liquid formation, while the high angle grain boundary was wet more or less uniformly [2]. In the latter study, a dislocation pairing mechanism was discovered, in which neighbouring premelted dislocations fuse together when they grow large enough [38]. For certain intermediate angle boundaries hysteresis was exhibited in their premelting behaviour because of this mechanism [38]. In another study, comparisons of the PFC model to a related amplitude model explained how disjoining pressure in the PFC model is related to the decay of various amplitude modes of the density [54]. In addition to the studies solely dealing with PFC models, there are two significant studies in which PFC and MD models are compared. In Ref. [52] it was shown that the dislocation pairing mechanism also occurs in MD and is related to elastic and core effects in the material. Later another study followed in which premelting behaviour PFC simulations, PFC amplitude simulations, and MD simulations were compared and the MD model was used to help tune the PFC model to give a more realistic model for BCC iron [53]. Although most of the computational studies using atomistic techniques have been done for pure materials, work has been recently done on premelting behaviour in binary alloys using the phase field crystal (PFC) model for a generic double lens alloy [17] and monte carlo (MC) simulations for aluminum magnesium[55].

Thermodynamics of Grain boundary premelting

Premelting can manifest itself in many different ways depending on the type of grain boundary. Small liquid pools can form at a grain boundary. These considerations take aside us into nucleation theory, which will be covered in section 1.3. Instead this section will focus on a general formalism to describe some general features about premelting.

The free energy of uniformly wetted grain boundary is:

$$F = F_s + F_l + V = A(w-h)f_s + Ahf_l + V(h) \tag{1.11}$$

where A is the surface area of the grain boundary, h is the width of the liquid layer, f_s is the solid free energy density, f_l is the liquid free energy density, $V(h)$ is the disjoining potential, whose limits are $V(0) = \gamma_{gb}$ and $V(\infty) = 2\gamma_{sl}$ [46, 48, 38]. In early theories of grain boundary premelting, the following ansatz was used for disjoining potential:

$$V(h) = 2\gamma_{sl} + (\gamma_{gb} - 2\gamma_{sl}) \exp(-h/\delta) \tag{1.12}$$

where δ is the decay length of the interaction force between the two grains, which is on the order of the size of the interface thickness [46, 48, 38]. According to this theory, it was suggested that grain boundary premelting essentially just happened for replusive grain boundaries while lower energy grain boundaries can be overheated to metastable states.

Although the conclusions are roughly correct, in that high energy grain boundaries typically premelt and lower energy ones typically do not, the disjoining potential is somewhat more complicated. High energy grain boundaries typically have a repulsive disjoining potential and can be fit

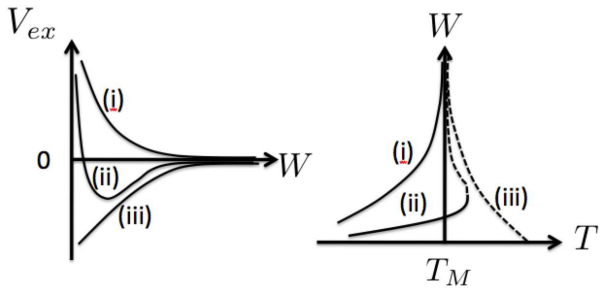

Figure 1.4: The disjoining potential, $V(W)$ vs. width, W, for (i) repulsive, (ii) attractive-repulsive and (iii) attractive grain boundaries *(left)*. The corresponding grain boundary width vs. temperature, T *(right)*. The dashed lines in the right plot are unstable widths; that is, such a boundary will either degree completely melt or shrink to a smaller stable width. From Ref. [3].

by a single exponential. However, lower energy grain boudaries are usually more complex. They often display attractive behaviour at large distances and replusive behaviour at short distances. The disjoining potential of such grain boundaries can be fit to two exponentials:

$$V(h) = 2\gamma_{sl} + C_1 \exp(\lambda_1 h) + C_2 \exp(\lambda_2 h) \tag{1.13}$$

where $C_1 + C_2 = (\gamma_{gb} - 2\gamma_{sl})$ and λ_1 and λ_2 are fitting constants [48], which Ref. [54] related to the rates of decay of various density wave modes. Schematic disjoining potential curves and the related wetting layer width vs. temperature plots can be seen in Fig. 1.4

To determine the disjoining potential, as a function of width, the width needs to be defined. In phase field simulations, it is straightforward to determine the width, which can be defined as the distance between the points where the order parameter is halfway between the solid and liquid values [3]. It can also be defined as the distance between the peaks in the grand potential profile of the interface [29]. In MD simulations, an order parameter based on the positions of neighbours of an atom can be defined [55] and then a method analogous to Reg. [3] can be used. Ref. [38] related the excess mass of the interfacial region to an effective amount of grain boundary liquid content, with the following relations:

$$\begin{aligned} \Gamma_n^{ex} &= \frac{1}{A}\int_V n - n_s d\vec{r} \\ h &= \frac{\Gamma_n^{ex}}{n_l - n_s} \end{aligned} \tag{1.14}$$

where A is the area of grain boundary, V is the volume of the system, n_s is the average density of the solid, n_l is the average density of the liquid, and h is the width of the boundary.

1.3 Cluster Formation

Clusters are small regions in an alloy material, in which excess solute gathers as precursors to a phase transition. In fact, they are coherent structures preceding the formation of GP zones; that is, they are the first of many stages in the formation of precipitates, which have a significant impact on the mechanical properties of the alloy [14, 56]. Clusters have been studied by various experimental techniques, such as 3D atom probe tomography [57, 58, 59, 60], transmission electron microscopy [61, 62, 58, 59, 60], and positron annhilitation spectroscopy [63, 59] in mainly Al-based alloys

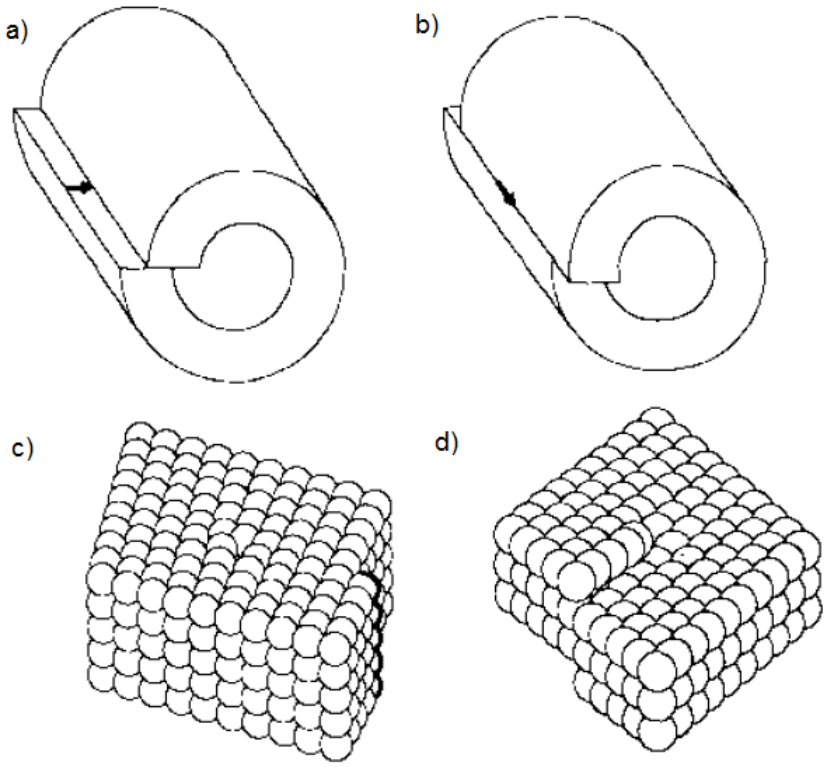

Figure 1.5: Illustrations of edge *(left frames a, c)* and screw dislocations *(left frames b, d)* in terms of material distortion *(top frames a, b)* and in terms of how atoms in the crystal are positioned *(bottom frames c, d)*. The arrows in *(top frames)* show how the crystal has been distorted. Adapted from [4].

(Mg, Cu, and Si are common alloying elements). Currently, it is believed that defects, such as excess vacancies or dislocation loops facilitate the formation of these clusters by providing a region into which the solute atoms, which are different in size from the solvent atoms, can easily move [61, 57, 59, 60].

To understand the mechanism of cluster formation better, computation techniques can be used. Because of the length scales involved, atomistic simulations are needed. However, this phenomenon has only been addressed directly with the PFC formalism [14, 18, 64] because of the temporal and/or spatial scales limitations of other atomistic computational techniques such as CDFT, MD, and MC. To understand the computational (and experimental) studies of cluster formation, dislocation theory and nucleation theory need to be understood.

1.3.1 Dislocations and Solute Segregation

Dislocations occur when there is a misalignment between the atoms of 2 perfect crystals which meet each other. There are two basic kinds: screw dislocations, in which half a plane of neighbouring atoms is shifted parallel with respect to a first set of atoms, and edge dislcoations, an half extra plane of atoms is found in a crystal. Most dislocations are an intermediate combination of the two basic types. Illustrations of both ideal types can be found in Fig. 1.5. Because the focus of this thesis is on 2D structures and screw dislocations cannot be found in 2D, subsequent discussion of dislociations will only concern itself with edge dislocations.

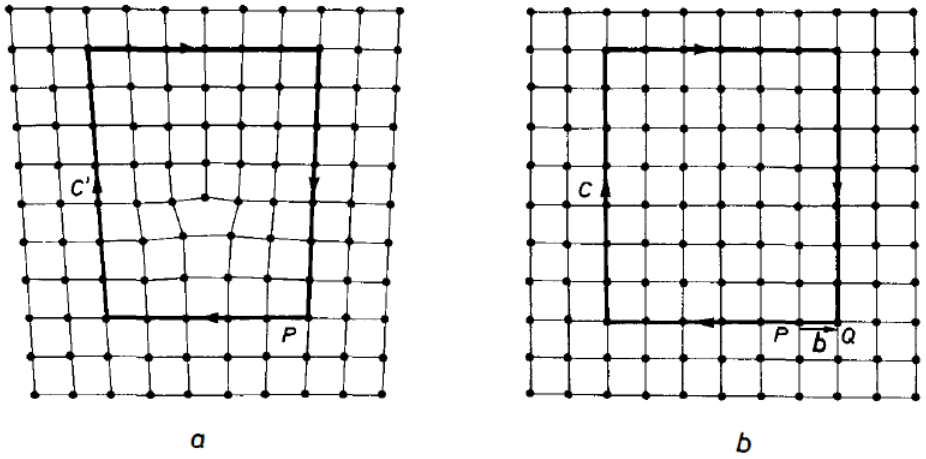

Figure 1.6: Schematic of a Burger's vector in a square lattice with a dislocation. In the left image, a circuit C' is drawn around the dislocation to the original point clockwise. If this same circuit is placed in a perfect crystal, then an extra step, $-\vec{b}$ needs to be added to complete the circuit. $\vec{b}$ is the Burger's vector. From [4].

Stress and Energy around a Dislocation

The presence of a dislocation induces strain fields and strain fields. In cylindrical coordinates (r, ϕ, z) , the stress fields, σ_{ij}, in an isotropic medium are:

$$\begin{aligned} \sigma_{rr} = \sigma_{\phi\phi} &= \frac{-Gb\sin\phi}{2\pi(1-\nu)r} \\ \sigma_{r\phi} &= \frac{-Gb\cos\phi}{2\pi(1-\nu)r} \\ \sigma_{zz} &= \frac{-Gb\nu\sin\phi}{\pi(1-\nu)r} \end{aligned} \tag{1.15}$$

where ν is the Poisson ratio of the material, G is the shear modulus, and b is the magnitude of the Burgers vector [65]. The Burger's vector, $\vec{b}$, is determined formally by a Frank circuit [4], which is illustrated in Fig. 1.6.

The above equations are only valid outside of the core region. In the core region, nonlinear effects dominate. Integrating Eq.1.15 over the strain field, with integration cut-offs at the core radius, r_0, and another at the effective size of the system, R, (e.g., grain size, average dislocation distance) results in the energy of a dislocation:

$$E_{dislocation} = A\ln\left(\frac{R}{r_0}\right) \tag{1.16}$$

where $A = \frac{Gb^2}{4\pi(1-\nu)}$ [66]. Eq. 1.10 can be derived by integrating over the elastic energy of a line of dislocations in a low angle boundary and adding the core energies to that result.

Segregation around a dislocation

As would be expected on physical grounds, the stress field can cause solute segregation in alloys because larger atoms can be better accommodated in regions of tension, while smaller atoms can be

better accomodated in regions of compression. In [65], the deviation of the concentration field, c, about its average c_0 in a substitutional alloy is derived:

$$c - c_0 = \chi\eta\sigma_{kk} \tag{1.17}$$

where $\sigma_{kk} = \sigma_{xx} + \sigma_{yy} + \sigma_{zz}$, η is the mismatch between the two atomic species, and

$$\frac{1}{\chi} = \rho_0 \frac{\partial M_{1d}}{\partial c} \approx \frac{\rho_0 RT}{c}\left(1 + \frac{\partial \ln \gamma_1}{\partial c}\right) \tag{1.18}$$

where R is the universal gas constant, T is the temperature of the system, ρ_0 is the density of the system, $M_{12} = \mu_1 - \mu_2$, μ_c is the chemical potential of the concentration, μ_{c0} is the chemical potential of matrix phase when the system is pure, and $\gamma_1 = \exp(\mu_c/RT\mu_{c0})$ is the activity of the solute species [67].

Because the solute atoms have moved to accomodate the stress fields, the stress fields are decreased. To account for this decrease, the so-called open system elastic constants are typically used:

$$\begin{aligned} G_{os} &= G \\ \nu_{os} &= \frac{\nu - \eta^2\chi E}{1 + \eta^2\chi E} \\ E_{os} &= \frac{E}{1 + \eta^2\chi E} \\ K_{os}^{-1} &= K^{-1} + 9\chi\eta^2 \end{aligned} \tag{1.19}$$

where K is the bulk modulus, E is the Young's modulus of the system, and os respresents the open-system elastic constants [65].

Substituting the open system elastic constants into Eq. 1.15 gives:

$$\begin{aligned} \sigma_{rr} = \sigma_{\phi\phi} &= \frac{-Gb(1 + \chi\eta^2 E)\sin\phi}{2\pi(1 - \nu + 2\chi\eta^2 E)r} \\ \sigma_{r\phi} &= \frac{-Gb(1 - \nu + \chi\eta^2 E)\cos\phi}{2\pi(1 - \nu + 2\chi\eta^2 E)r} \\ \sigma_{zz} &= \frac{-Gb(\nu - \chi\eta^2 E)\sin\phi}{\pi(1 - \nu + 2\chi\eta^2 E)r} \end{aligned} \tag{1.20}$$

Substituting Eqs 1.20 (with the appropriate coordinate transformation) into Eq. 1.17 results in a solute distribution known as the Cottrell atmosphere, which is shown in Fig 1.7:

$$c - c_0 = \frac{-\chi\eta Gb(1 + v)\sin\phi}{\pi(1 - \nu + 2\chi\eta^2 E)r} \tag{1.21}$$

When considering a ternary alloy, the equations for the open system elastic constants somewhat more complicated. Although [68] suggested corrections to the work of [65], the approximation by [65] is sufficiently accurate to be used:

$$\frac{1}{\chi_N} = \rho_0 \left|\frac{\partial M_{1k}}{\partial c_j}\right| \tag{1.22}$$

where $||$ denotes the determinant of a matrix whose components depend on the chemical potential differences of the solvent species with the other species in the system, M_{1k}, and c_j is the concentration with respect to which this chemical potential difference is differentiated. Also, in a ternary

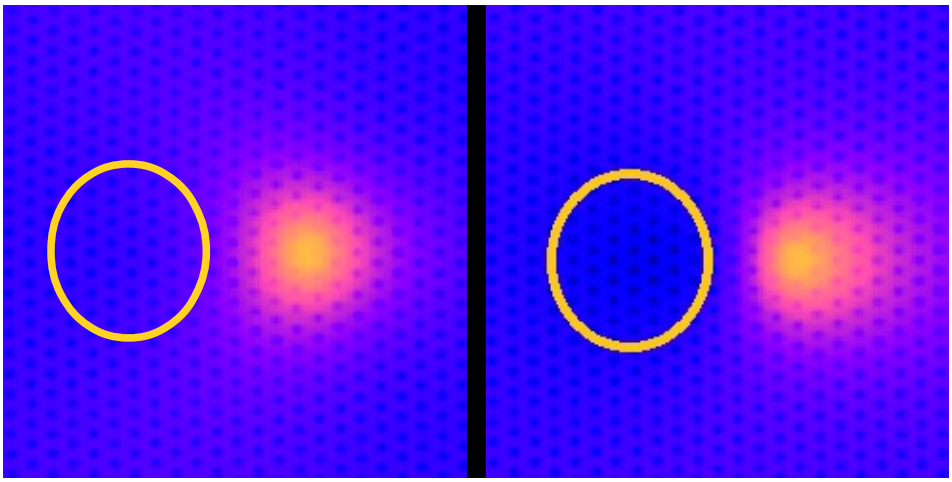

Figure 1.7: Images of a dislocation in a binary alloy without mismatch *(left)* and with mismatch *(right)* between the atomic species. Blue is low solute concentration, while yellow and red are high solute concentration in the images. Without misfit, solute only segregates to the core. With misfit, the larger solute atoms move to regions under tension, while they move away from regions under compression. The concentration difference between the two images is most noticeable in the yellow circle and in the change of shape of the solute field around the core. From [5].

alloy, the quantity $\eta^2\chi$ in the above equations is replaced by:

$$\frac{\eta_2^2 \frac{\partial M_{13}}{\partial c_3} + \eta_3^2 \frac{\partial M_{12}}{\partial c_2} + \eta_2\eta_3 \left(\frac{\partial M_{12}}{\partial c_3} + \frac{\partial M_{13}}{\partial c_2} \right)}{\left| \frac{\partial M_{1k}}{\partial c_j} \right|} \tag{1.23}$$

1.3.2 Nucleation Theory

Homogeneous Nucleation

In classical nucleation theory, a particle of a particular shape is assumed to grow in a material. If it grows in the bulk of a material, the process is known as homogeneous nucleation. Assuming a new phase of spherical shape with radius, R, then the free energy change in the system, ΔF, is:

$$\Delta F = \frac{4\pi}{3} R^3 \Delta f + 4\pi R^2 \gamma \tag{1.24}$$

where $\Delta f = f_2 - f_1$ is the free energy density difference of the new phase (2) and original phase (1) and γ is the interfacial energy between the phases [69]. A new phase has nucleated when any increase in size of the new phase decreases the free energy; that is, $dF/dR < 0$. Radius at which the free energy no longer increases, the critical radius, R_c is found by differentiating Eq. 1.24 and setting that value to 0:

$$\frac{dF}{dR} = 4\pi R^2 \Delta f + 8\pi\gamma R = 0 \Rightarrow R_c = -\frac{2\gamma}{\Delta f} \tag{1.25}$$

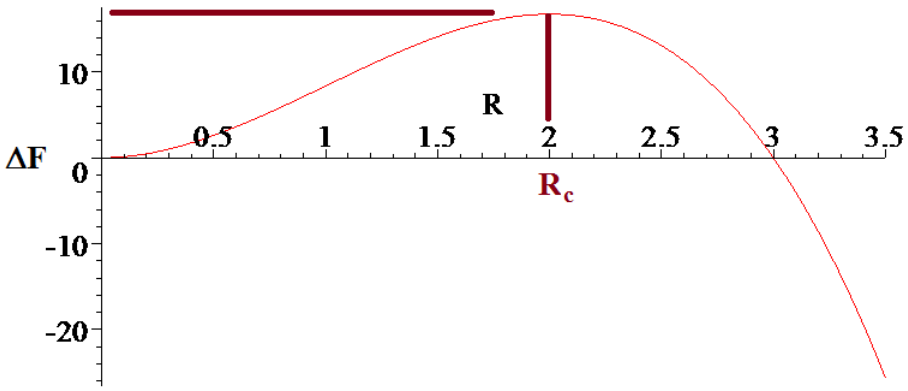

Figure 1.8: Plot of Eq.1.24 for $\Delta f = -1$, $\gamma = 1$. Labelled are the critical radius $R_c = 2$ and the critical work of formation, $W_c = 16\pi/3 \approx 16.8$.

Below this size, the new phase particle is known as a cluster or embryo [69]. The free energy at R_c is the critical work of formation, W_c, [69], also referred to as the nucleation barrier, and is equal to:

$$W = \frac{16\pi\gamma^3}{3\Delta f^2} \tag{1.26}$$

The results are similar for an alloy, except that the relevant thermodynamic potential is the grand potential [69]. An illustration of the free energy in Eq. 1.24 are shown in Fig. 1.8.

Elastic Effects on Nucleation

In Eq. 1.24, it is assumed that the only factors contributing to the excess free energy of the forming nucleus are the surface energy and thermodynamic driving force. However, if a coherent precipitate forms when the lattice parameter of the two phases is different, then by necessity, there is elastic energy. In [69], the additional free energy of the system in 3D is shown to be:

$$\Delta F_{el} = \frac{4\pi}{3} R^3 (\Delta f_e) = \frac{4\pi}{3} R^3 (6 G_1 A \delta^2) \tag{1.27}$$

where $A = \frac{3K_2}{3K_2+4G_1}$, G_1 is the shear modulus of the original phase, K_2 is the bulk modulus of the precipitate phase, and δ is the misfit strain in the nucleating particle. Eq. 1.27 means that the total free energy of the system is:

$$\Delta F = \frac{4\pi}{3} R^3 (\Delta f + 6 G_1 A \delta^2) + 4\pi R^2 \gamma \tag{1.28}$$

As can be seen according to Eq. 1.28, the elastic energy increases the nucleation barrier, as shown in Fig. 1.9. In fact, the elastic energy in forming a certain material could cause a less thermodynamically favourable state to be nucleated which is closer in structure to the original state. Essentially, this is one of the mechanisms which allows GP zones to be favoured during the early stages of precipitate formation in various Al-Cu alloy [56].

Dislocation-aided nucleation

Dislocations and other defects can aid nucleation of a new phase. When a nucleus forms on a defect, the process is known as heterogeneous nucleation. Often, heterogeneous nucleation is energeti-

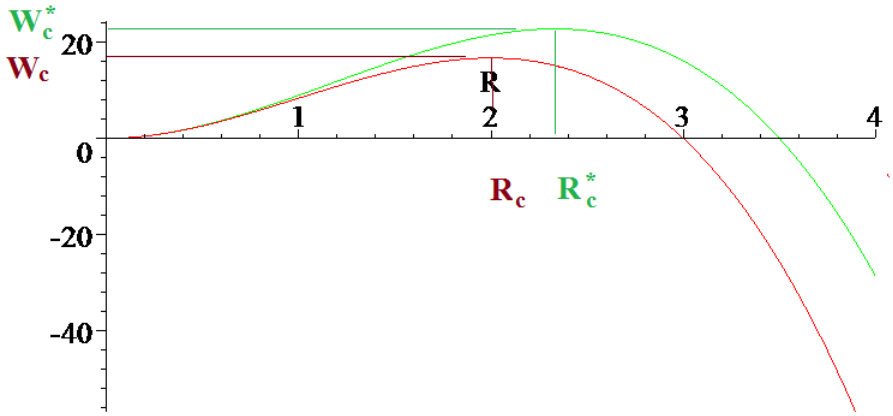

Figure 1.9: Plot of Eq.1.28 for $\Delta f = -1, \gamma = 1, \Delta f_e = 0$ *(dark red)*, $\Delta f = -1, \gamma = 1, \Delta f_e = 1/7$ *(light green)*. Labelled are the critical radius R_c and the critical work of formation, W_c. A $*$ denotes the values for the curve with strain energy contributions, while the unsuperscripted terms correspond to those of Fig 1.8.

cally more favourable than homogeneous nucleation and therefore occurs more often [69]. For this section, only nucleation on an edge dislocation will be considered.

For an incoherent precipitate nucleating around an edge dislocation, the precipitate is assumed to grow stress free around the dislocation core. According to [69, 6] the free energy difference per unit length of a cylindrical precipitate of radius, R, growing around a dislocation is:

$$W = \pi R^2 \Delta f + 2\pi\gamma R^2 - A \ln R + const \tag{1.29}$$

where

$$A = \frac{Gb^2}{4\pi(1-\nu)}$$

where G is the shear modulus of the initial (parent) phase, b is the length of the Burgers vector of the dislocation, and ν is the Poisson ratio of the material. Two scenarios can result, depending on the parameter

$$\alpha = \frac{-2A\Delta f}{\pi\gamma^2}$$

which determines if the free energy curve has a local mininum for finite R. If $\alpha < 1$, then there is a finite size concentration atomsphere around the dislocation, which approximates a Cottrell atmosphere [69, 6]. For precipitation to occur, an energy barrier needs to be overcome. If $\alpha > 1$, then nucleation occurs without an energy barrier; that is, the decrease in elastic energy and the decrease in bulk free energy of the system are always greater than the increase in free energy due to surface area. These scenarios are illustrated in Fig. 1.10.

1.4 Explosive Crystallization

Explosive crystallization is a phenomenon, in which a metastable amorphous phase crystallizes very quickly because the latent heat released raises the temperature of the system around the interface and allows a self-sustaining reaction to take place [10, 70]. It was first observed in 1855 by Gore in Sb thin films [71]. With the experiments done over the next century, ripple or wave-like oscillations were observed in the rather thin films, but not in thicker films [72, 7], as can be observed in Fig. 1.11. Starting in the late 1960's and into the 1980's, explosive crystallization was studied in other

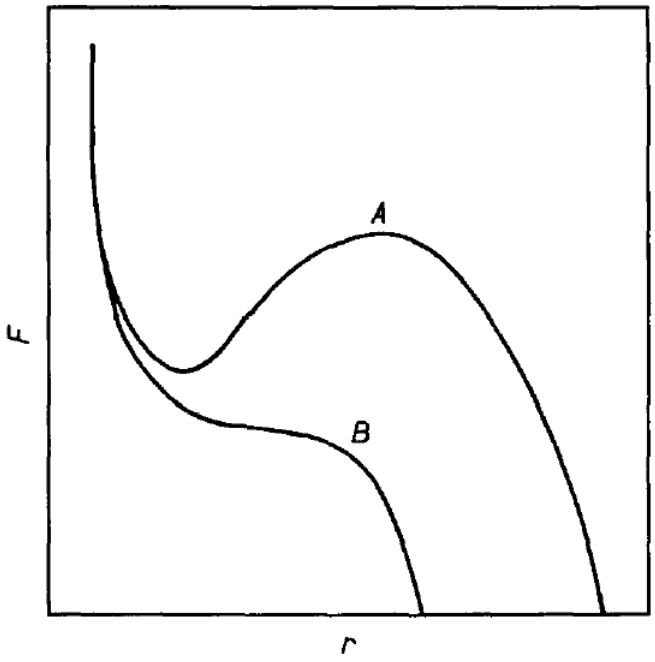

Figure 1.10: Schematic of Eq.1.29 for $\alpha < 1$ *(A)* and $\alpha > 1$ *(B)*. From [6].

materials such as Ge [73, 74, 75], Si [76, 9, 77], and Sb-based semiconductors [8]. Once again, the undulating patterns were observed in these newer materials of which an example is shown in Fig. 1.12. These oscillations even caused impurity segregation patterns in the material [9], an important effect when considering the importance of local impurity to semiconduction.

Because of the importance of avoiding amorphous to crystalline phase transitions in certain applications, such as solar cell and other semiconductor device fabrication, this phenomenon is still commonly studied [70, 78]. Some of the techniques used to study the effects of explosive crystallization are transmission electron microscopy (TEM) and atomic force microscopy (AFM) [79], dynamic TEM [80, 78] and tracking of the interface with a light microscope and a CCD camera [70]. Traditionally the resulting patterning was studied after the reaction (e.g., [79]), though now the dynamic techniques allow the reaction to be studied as it proceeds (e.g., [70, 78]).

It was understood that in the steady state reaction the rate at which latent heat was released was balanced by various heat losses from the interface [8, 75]. To describe the undulations seen in systems undergoing explosive crystallization, the first conistent theory was proposed by Refs. [81, 10], in which a thermal instability leading to temporal oscillations of the reaction front temperature was found to occur. This work was then extended to include the effects laser driven processes, in which the type of instability was found to vary depending on the speed at which at the reaction progressed; beyond the steady state case, two kinds of instabilities could occur, which were the oscillatory pattern observed in explosive crystallization and a more traditional Mullins and Sekera-type spatial instability [82]. Although the models were considered for the highly idealized case of a complete reaction, incomplete crystallization was found to support the phenomenon as well [83]. Another important theoretical contribution was considering the effect an intermediate liquid layer has on the reaction [70].

In addition to the sharp interface studies listed above, simulations can be done to provide additional insight into the mechanisms involved. Phase-field-like reaction-diffusion models have been shown to reproduce the thermal instability, while allowing other effects, such as those relating to

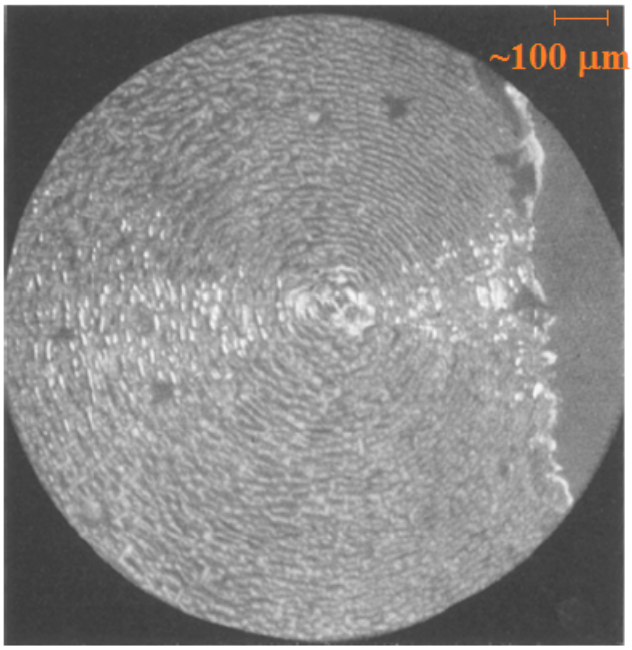

Figure 1.11: Oscillations from explosive crystallization as indicated by alternating layers of lighter and darker material in tapered Sb sample. Adapted from [7].

mass transport, to be studied [11]. In fact, a connection between the sharp interface models and diffuse interface reaction-diffusion models was shown by Ref. [11]. Also, a number of molecular dynamics studies have been done to study rapid solidification of semiconductor materials by Refs. [84, 85, 86, 87, 88]. Although these studies are unable to produce the thermal oscillations because they can only be done for very short time and length scales, they allow for computation of constitutive relations (such as the relation linking the velocity of the interface to its temperature) and the details of particular atomic processes, such as crystallization from an amorphous material directly or from a precursor liquid state. Refs [84, 87] even study solutal effects in rapid solidification such as partitioning and ways in which dopants can halt the reaction in Si- and Ge-based materials.

As noted by [9], the oscillations can cause patterns in solute distribution in the system. A scan of relating to the composition of the material is shown in Fig. 1.13. Although the patterning of impurities being has not typically been the focus of explosive crystallization studies, much work has been done in studying a related phenomenon, banded structures in metal alloys and other materials, from theoretical, experimental, and computational perspectives [89, 90, 91, 92, 93, 94, 95, 96]. These studies have found a strong effect of concentration on the velocity of the material through undercooling. That being said, the work of Ref. [92] also considered the thermal effects, which could be used to consider banding and the unduluations in the explosive crystallization as part of a more general class of oscillatory phenomena.

1.4.1 Phenomenological Description of Explosive Crystallization

Steady State

To work out the basic physics of explosive crystallization in a thin film of pure material, only the temperature field in the system along with an expression for the temperature-dependent kinetics of a sharp interface are needed. In the work of Ref. [10], the temperature field is treated in the comoving

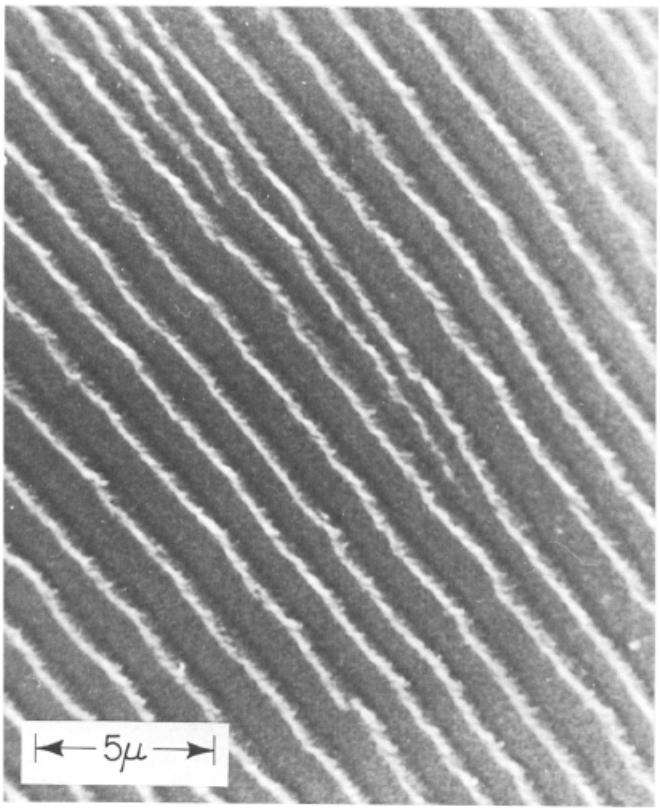

Figure 1.12: Oscillations from explosive crystallization in GaSb. From [8].

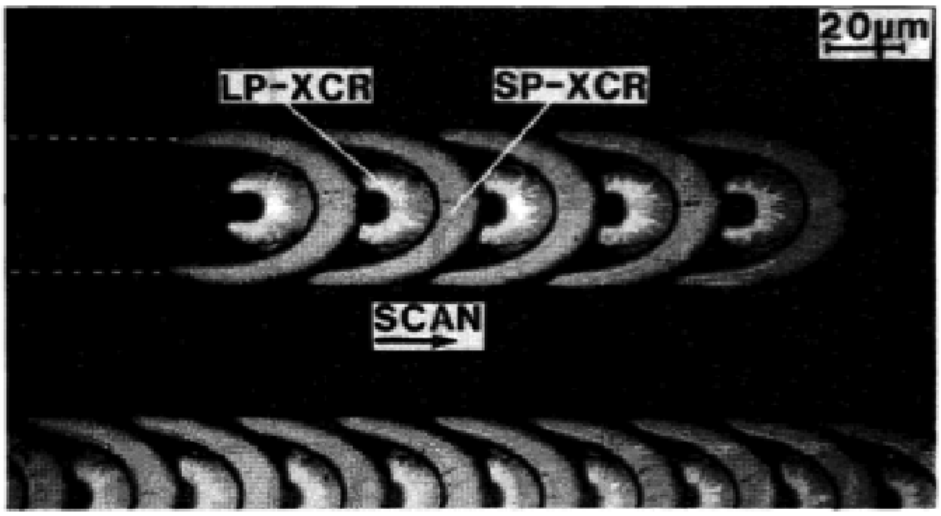

Figure 1.13: Periodic patterning of Solute in Explosive Crystallization of Si with impurities (Sb^+ and As^+). From [9].

reference frame, where the interface velocity is dependent on the peak temperature, T^b, as given by:

$$V(T^b) = V_0 \left[1 - \exp\left(\frac{L}{k_B}\left(\frac{1}{T^b} - \frac{1}{T_M}\right)\right)\right] \exp\left(-\frac{E_a}{k_B T^b}\right) \tag{1.30}$$

where V_0 is a constant, T_M is the melting temperature of the material, L is the latent heat released on crystallization, E_a is the activation energy of atomic diffusion, and k_B is the Boltzman constant. Eq. 1.30 is interpreted as a product of a mobility (rightmost Arrhenius function) and thermodynamics driving force (square brackets). Although many modes of growth are possible (solid phase epitaxy, solid phase nucleation, liquid phase epitaxy, liquid phase nucleation), considering just a single growth mode gives a good understanding of instability causing the oscillation [70]; for example, Eq. 1.30 corresponds to liquid phase epitaxy.

To determine how the temperature field evolves, there are three main contributions which need to be considered: heat diffusion, heat losses through the substrate, and the latent heat generated at the interface. With these considerations in mind, the temperature, T, generated by the heat released from the interface evolves according to the following equation in a 1D reference frame with coordinate, x, moving with the interface at velocity, V:

$$\frac{\partial T}{\partial t} = M_T \frac{\partial^2 T}{\partial x^2} + V\frac{\partial T}{\partial x} - \Gamma(T - T_0) + qV\delta(x) \tag{1.31}$$

where M_T is the diffusivity of the heat field, $\Gamma(T - T_0)$ is Newton's law of cooling, where Γ is a constant describing how quickly heat losses occur and T_0 is the substrate temperature, and $qV\delta(x)$ represents the latent heat released by an infinitely sharp interface, where $q = L/C$ and C is the heat capacity of the material [10]. Solving the above partial differential equation (PDE), for a steady state solution, means that

$$\frac{\partial T}{\partial t} = 0 \tag{1.32}$$

and so Eq. 1.31 can be written as:

$$0 = M_T \frac{\partial^2 T}{\partial x^2} + V\frac{\partial T}{\partial x} - \Gamma(T - T_0) + qV\delta(x) \tag{1.33}$$

Because Eq. 1.33 is a linear equation and the t-dependence of the parameters is being neglected, it can be simplified by substituting a sample solution $T(x) = \Delta T \exp(\lambda x) + T_0$ into it, which gives the following equation for λ:

$$\begin{aligned} 0 = & \quad M_T\lambda^2 + V\lambda - \Gamma \\ \lambda = & \quad \frac{-V \pm \sqrt{V^2 - 4M_T\Gamma}}{2M_T} \end{aligned} \tag{1.34}$$

Because of the δ function, there is a different solution for $x > 0$ from $x < 0$. The boundary conditions at $x = \pm\infty$ are $T = T_0$, which means that

$$\begin{aligned} \lambda_+ &= \frac{-V + \sqrt{V^2 + 4M_T\Gamma}}{2M_T}, x < 0 \\ \Rightarrow \lambda_- &= \frac{-V - \sqrt{V^2 + 4M_T\Gamma}}{2M_T}, x > 0 \end{aligned} \tag{1.35}$$

Integrating Eq. 1.33 an infinitesimal distance around the delta function in the temperature equation

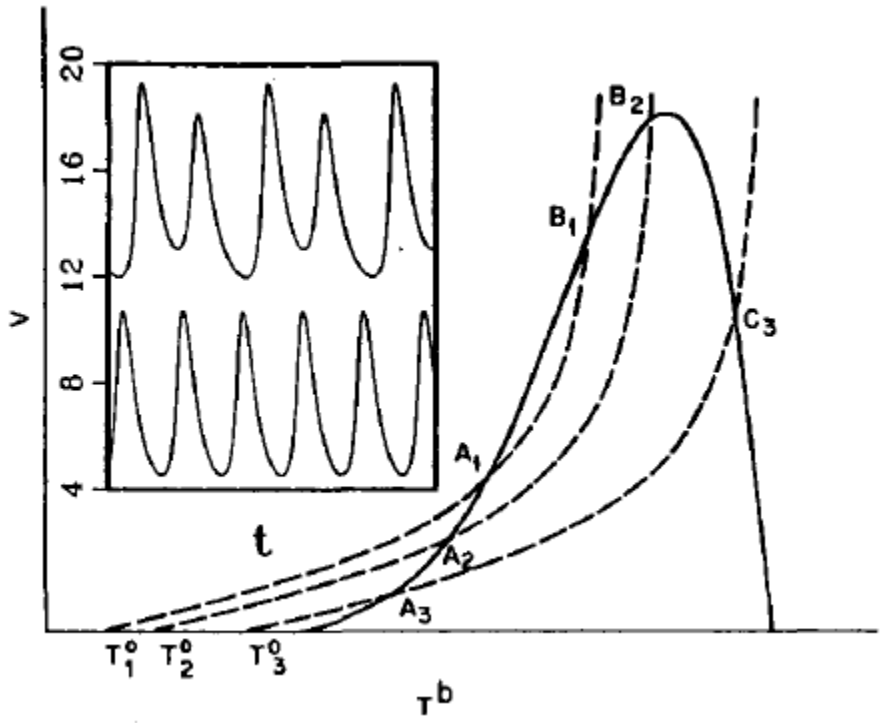

Figure 1.14: Determination of steady state velocity, $V = V_{ss}$, and interface temperature T^b for 3 substrate temperatures, T_1^0, T_2^0, T_3^0 by the intersection of the dashed curves, Eq. 1.36, with the solid nose-shaped curve, Eq. 1.30. Not all solutions are stable; solutions labelled A_i or B_1 are unstable and result in extinguished or oscillatory solutions respectively. Inset - Various oscillatory solutions of velocity V in time t about the steady state velocity, V_{ss}. The period-2 solution has no offset, while the period-4 solution is offset by 8 units on the graph. From Ref. [10].

gives the following boundary condition at $x = 0$:

$$0 = \left(M_T \frac{\partial T}{\partial x} \right)_{x=0-}^{x=0+} + qV$$

By substituting in $T = T_0 + \Delta T \exp(\lambda x)$ and using Eq. 1.35, the following condition is obtained for the steady state velocity, $V = V_{ss}$, in terms of the interface temperature, $T(x = 0) = T^b$:

$$V_{ss} = \frac{2\sqrt{M_T \Gamma}}{\sqrt{(q/\Delta T_{ss})^2 - 1}} \tag{1.36}$$

where $\Delta T_{ss} = T^b - T_0$. Simultaneously solving Eq. 1.36 and Eq. 1.30 allows V_{ss} and T^b to be determined, as illustrated in Fig. 1.14.

Oscillations

Steady state solutions exist as long as Eq. 1.36 and Eq. 1.30 can be solved simultaneously. However, even in these instances a steady state solution might not be realized. The reaction may go through from transitory oscillations and then stop or it might continue by propagating in an unsteady fashion,

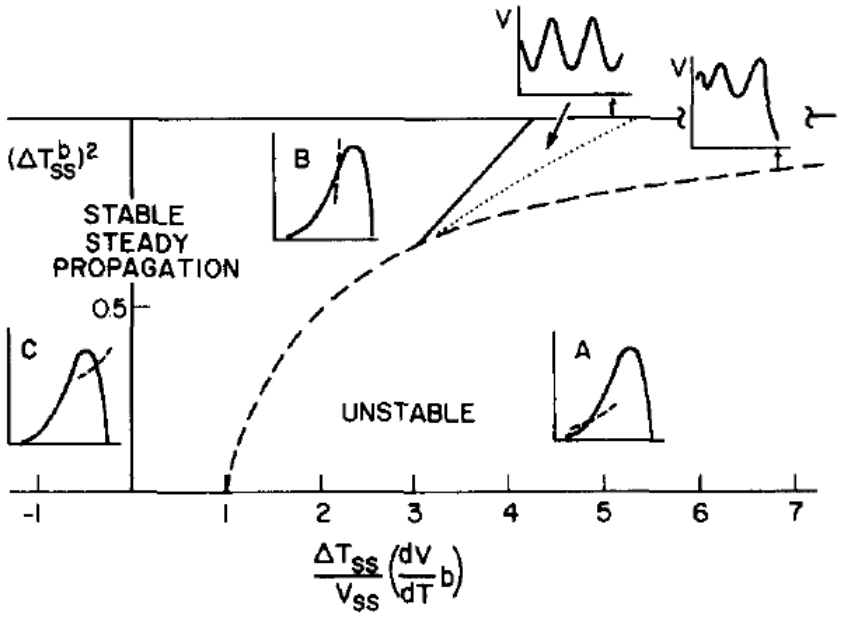

Figure 1.15: Phase diagram for stability of steady state solution for different α and β. Insets show the type of solution that can be observed, while the regions with labels A, B, and C correspond to the types of solutions labelled as such in Fig. 1.14. From Ref. [10].

for which V might have the form of the solutions shown in the inset of Fig. 1.14. The focus of this section is to describe when deviations from the steady state solution occur.

To determine how an oscillation occurs, the stability of the initial steady state solution described above needs to be analysed. Two parameters suffice to describe when an oscillation will occur in the sharp interface model, the non-dimensional slope

$$\alpha \equiv \frac{\Delta T_{ss}}{V_{ss}} \frac{\partial V(T^b)}{\partial T^b}\bigg|_{T_{ss}} \tag{1.37}$$

and the squared steady state non-dimensional temperature difference,

$$\beta \equiv \left(\frac{\Delta T_{ss}}{q}\right)^2 = \left[\frac{4\Gamma M_T}{V_{ss}^2} + 1\right]^{-1} \tag{1.38}$$

where $\Delta T_{ss} = T^b - T_0$, where T^b is the steady state interface temperature, and the $V(T^b)$ used for differentiation is determined from Eq. 1.30. As a general rule, if α is small, then the corresponding steady state solution is stable, and if it is large, then the steady state solution is unstable. If β is small, that is $\beta < 2/3$ for an α at which front propagation is unstable, then the reaction eventually dies out. However, if β is relatively large, that is $\beta > 2/3$, then there is the possibility of a self-sustaining oscillating reaction front for intermediate α, while at large α the front propagation dies out. The details of this linear stability analysis can be found in the appendix C, in which it is shown under which conditions the interface becomes unstable. A phase diagram illustrating the behaviour of the reaction front is shown in Fig. 1.15.

Beyond these basic regimes of steady state reaction propagation, no propagation of the front, and an oscillatory propagation of the front, the oscillating modes of the front propagation can period

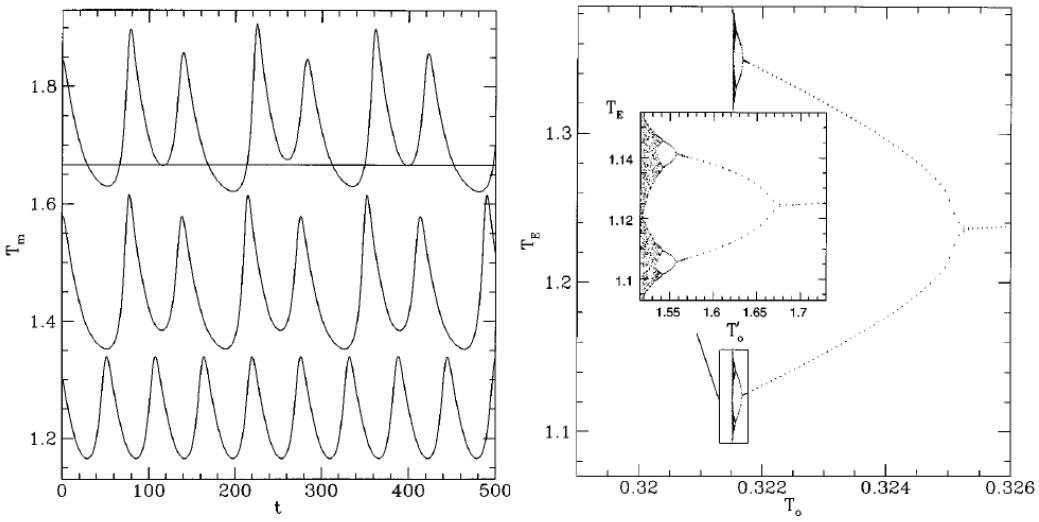

Figure 1.16: Left - Maximum temperature in the system, T_m, as the reaction front proceeds. The period-4 and period-8 oscillations are shifted so that all of the curves are distinguishable. Right - Bifurcation diagram for extremal temperatures of system, T_E, against substrate temperature T_0, in a reaction diffusion model. Inset - Zoom-in on one branch of the bifurcation diagram, where $T_0' = (T_0 - 0.32) \times 1000$. Adapted from Ref. [11] in which the simulation parameters can be found.

double into period-4, period-8 oscillations and even chaotic oscillations. As shown in Fig. 1.16, the diffuse reaction diffusion model of [11] also supports higher order oscillations from which a bifurcation diagram of the extremal temperatures, T_E, in an oscillation of the maximum temperature of the system, T_m, at a given time can be drawn. It should be noted that in the sharp interface limit, there is a 1-to-1 correspondence between T_m and V on the left hand side of the nose-shaped curve because of Eq. 1.30.

Chapter 2

Phase Field Crystal Model

2.1 Introduction

The phase field crystal (PFC) model was originally developed to simulate phase transitions involving crystalline systems on atomic length scales and diffusive time scales. It borrowed from various pattern formation models, in which a relatively simple form for a free energy functional is used to simulate periodic structures in a system under a certain parameter regime [39]. This and a further study, Ref. [1], showed that this model was successfully able to incorporate many common features of crystalline systems, which include solild phase elasticity, grain boundary energy, grain growth, and crack formation, as well as correct solid-liquid phase behaviour during phase transitions. The original model, however, needed to be altered to describe dynamic elastic effects more correctly; this was achieved by introducing "quasi-phonons", as demonstrated in [97, 98].

After developing the model more completely through phenomenological approaches, a more systematic study showed how the PFC model relates to classical density functional theory (CDFT) [12]. In CDFT, atomistic properties of the system, such as its atomic correlation functions, are used to derive a free energy, from which the mesoscopic and macroscopic properties of a system can in principle be determined [99]. The time and length scales on which these dynamic simulations can be applied in metallic systems are limited with this method because the real density distribution is sharply peaked at the lattice positions [99]. The PFC model overcomes this limitation by smoothing the atomic density fields, thus compromising the quantitative nature of the model compared to CDFT. Despite this difference, various attempts have been made to make the PFC model more quantitative. For example, the density distribution fields in the PFC model can be related to a convolution of the real density distribution fields; e.g., Ref. [100]. As well, a number of quantitative studies have been done on surface tension, grain boundary energy, premelting, and elastic constants; see [101, 40, 102, 103]. As well, there are many examples of studies, which demonstrate the capability of PFC obtaining quantitative results, though they were not directed towards studying the properties of a particular material. Some examples of such work include the nucleation during solidification studies of [104], [105], [106] and the premelting work of [38]. Finally, the use of quasi-phonons by [97, 98] was also shown to emerge from solid hydrodynamics in the limit of long wavelengths and time scales [107].

One major limitation of the original PFC model is the limited number of crystal structures resulting from it. For the most part, the crystal structures which were produced in the simulations were those whose structure is strongly dominanted by a single peak in the two-point correlation function; that is, hexagonal close-packed structures (HCP) in 2D (which are "rods" in 3D) and body-centered cubic (BCC) in 3D (see [1, 101]). Some exceptions to these structures are those formed at high densities in the PFC model, where higher order resonances of the nonlinear terms allow for multipeak structures (see [104]). Early attempts to control structures with two dominant modes were

accomplished by [108, 109]. However, an entirely new paradigm, the XPFC paradigm developed by [110, 111], allows for arbitrary structures to be simulated more readily than the aforementioned approaches. With this method, it is straightforward to simulate systems with realistic phase diagrams. In this paradigm, the correlation function is represented by a number of Gaussian peaks in Fourier space, each of which represents the spacing of the dominant atomic planes, which will be described in section 2.4. These peaks vary with temperature according to a Debye-Waller factor. Nonetheless, even with these designed structures, simulating properties of defects accurately is a challenge. The work of Ref. [112] describes some of the challenges in obtaining correct crystal structures and defect properites in XPFC, PFC, and CDFT models.

PFC simulations are not only limited to pure materials; they have also been extended to alloys. Starting with the simple binary model in [39], it was not until [12] that binary alloy models were placed on rigorous ground. The XPFC model has also been extended to binary alloys by Greenwood et al [113]. Spinodal decomposition [12], eutectic growth [12, 104, 113], thin film patterning [114, 115], solute trapping [116], the Kirkendall effect [117], grain boundary energy [16], cluster formation ([14]), and solute drag ([41]) are among the applications that have been studied with this model. Besides being able to capture atomic scale spatial details on diffusive time scales, one of the big advantages of PFC-type models is that they self-consistently capture elasticity effects without having to specify further details, including mismatch between atomic species, which was important in many of the studies mentioned above. [118] have extended the XPFC model to systems with more components. Eutectic formation and the early stages of precipitate formation have been studied with a ternary model and the behaviour of cluster formation has been contrasted with the ternary model [18, 118].

Although longer spatial and temporal scales can be simulated with PFC-type models than CDFT models, one strong disadvantage in PFC models is still the size of the spatial domains which can be simulated; they are typically limited to having linear dimensions in the 10 or maybe 100 nm range because the models need roughly 8 points per linear dimension to resolve the atoms [119]. One method that has been considered to preserve the physics contained in the PFC model while allowing for larger systems sizes to be simulated is the PFC amplitude model, in which the density fields are described by an average density field and complex amplitude fields, in which both phase and elasticity/defect related information are stored. In fact there is a complex amplitude field for each reciprocal lattice vector being simulated in the density field [119]. With this formalism, successful simulations have been performed for much larger systems on an adaptive mesh [120, 121]. Refs. [119], [122], and [19] have also shown how the PFC amplitude model can be used to model binary alloys. In Ref. [119], Cottrell atmospheres, solute segregation to interfaces, and eutectic formation were studied. As well, thin films and their growth have been studied with this model [123]. Refs. [124, 125] have used this method to study surface tension and its anisotropy in pure materials and alloys. Ref. [19] used this model to study premelting, grain boundary energy, and the Asaro-Tiller-Grinfeld instability and demonstrate the effect of making the derivative terms rotationally covariant. Recently, Ref. [13] have expanded the amplitude approach to include multiple crystal structures and demonstrate how to systematically obtain arbitrary order rotationally invariant amplitude formalisms. Still, there is much information left out of the model. As Ref. [19] points out, there are a number of a problems relating to choosing a specific basis, namely that only small angles of misorientation between crystals can be properly represented in this method.

In addition to the above described uses, PFC-type models have been used to study various other systems. Systems with ferromagnetic states can be simulated by adding the approrpriate extra material fields (e.g., magnetization) and the corresponding external fields [126]. As well, the original PFC model has been used to study glasses by Berry et al [127]. The PFC formalism gives better glass properties if slightly modfiied to the vacancy PFC (VPFC) formalism [128], as shown by Refs. [129] and [130]. Finally, it should be mentioned that soft condensed matter systems including colloids and liquid crystals have been studied with PFC-type models (e.g., Ref. [131]), where a PFC-type description even performs better because the approximation of the density distribution

of the micron-scale "atoms" is much better. For a more complete review on the background and applications of the phase field crystal model, the reader is referred to Refs. [132] and [99]. Some of the details of the above-mentioned models are discussed further below.

2.2 PFC Model of a Pure Material

For a pure material, the free energy the system can be written as

$$\Delta F = \Delta F_{id} + \Delta F_{ex} + F_{ext} \tag{2.1}$$

where $\Delta F_{id}$is the ideal free energy due to entropy considerations relative to a reference state, ΔF_{ex} is the free energy due to interactions between particles, and F_{ext} is the change in free energy of the system due to external factors, such as a magnetic field acting on the system (cf. Ref. [133]). Now we write the individual terms of Eq. 2.1 as a functional of density, $\rho(\vec{r})$. For the ideal term free energy of mixing term, we arrive at

$$\Delta F_{id}[\rho] = k_B T \int_V \left[\rho \ln\left(\frac{\rho}{\rho_0}\right) - \delta\rho\right] d\vec{r} \tag{2.2}$$

where k_B is the Boltzman constant, T is the temperature, $\rho \equiv \rho(\vec{r})$, $\delta\rho = \rho - \rho_0$, ρ_0 is the reference density of the system about which the material properties are taken, and V is volume of the d-dimensional system in which the system is [12]. The excess free energy is given by:

$$\begin{aligned}\Delta F_{ex}[\rho] &= \tfrac{1}{2}\int_V \delta\rho\vec{r}\delta\rho'(\vec{r'})\tfrac{\delta^2 F}{\delta\rho\delta\rho'}d\vec{r}d\vec{r'} + \tfrac{1}{3!}\delta\rho'(\vec{r})\delta\rho'(\vec{r'})\delta\rho'(\vec{r''})\tfrac{\delta^3 F}{\delta\rho\delta\rho'}d\vec{r}d\vec{r'}d\vec{r''} + ... \\ &= -\tfrac{k_B T}{2}\int_V \delta\rho\delta\rho' C_2(\vec{r},\vec{r'})d\vec{r}d\vec{r'} - \tfrac{k_B T}{3!}\int_V \delta\rho\delta\rho'\delta\rho'' C_3(\vec{r},\vec{r'},\vec{r''})d\vec{r}d\vec{r'}d\vec{r''} + ...\end{aligned} \tag{2.3}$$

where $C_n(\vec{r}_1, \vec{r}_2, ...\vec{r}_n)$ is the n-point correlation function at the reference density in the reference state of the material [134, 12]. An external free energy contribution can be written as

$$\begin{aligned}F_{ext}[\rho; M, \lambda] &= \int_V M(\vec{r})\tfrac{\delta F}{\delta M}d\vec{r} \\ &= \int_V M(\vec{r})\lambda(\rho)d\vec{r}\end{aligned} \tag{2.4}$$

where M is the field acting on the system and λ is the material property of the field that interacts with the field—i.e., the complementary variable. When combining the above expressions, we get the classical density functional theory (CDFT) expression for the free energy of the system:

$$\begin{aligned}\Delta F[\rho] &= k_B T \int_V \rho \ln\left(\tfrac{\rho}{\rho_0}\right) - \delta\rho d\vec{r} - \tfrac{k_B T}{2}\int_V \delta\rho\delta\rho' C_2(\vec{r},\vec{r'})d\vec{r}d\vec{r'} \\ &\quad - \tfrac{k_B T}{3!}\int_V \delta\rho\delta\rho'\delta\rho'' C_3(\vec{r},\vec{r'},\vec{r''})d\vec{r}d\vec{r'}d\vec{r''} + ... + \int_V M(\vec{r})\tfrac{\delta F}{\delta M}d\vec{r}\end{aligned} \tag{2.5}$$

To derive the expression for the PFC free energy from Eq. 2.5, let $n = (\rho - \rho_0)/\rho_0$, expand the ideal term to 4^{th} order (or higher depending on the goal of the simulation), and truncate the excess term after the second order correlation function, which is taken about a liquid reference point. For simplicity, the free energy is renormalized by dividing out the energy density scale $k_B T\rho_0$. These algebraic manipulations result in:

$$\begin{aligned}F_{PFC} &= \frac{\Delta F[n]}{\rho_0 k_B T} \\ &= \int_V \frac{\Delta B}{2}n^2 - \frac{t}{3}n^3 + \frac{v}{4}n^4 d\vec{r} - \frac{1}{2}\int_V \delta\rho\delta\rho' C_2(\vec{r},\vec{r'})d\vec{r}d\vec{r'} + \int_V M(\vec{r})\frac{\delta F}{\delta M}d\vec{r}\end{aligned} \tag{2.6}$$

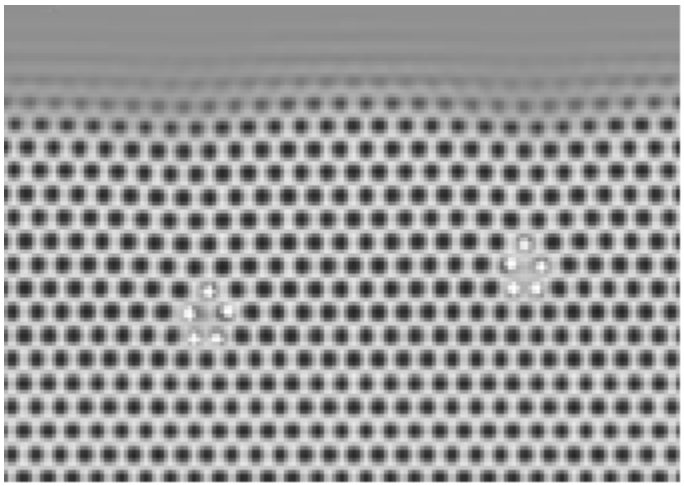

Figure 2.1: An image demonstrating pattern formation in the PFC model. At the top of the image, there is liquid and at the bottom a crystal with defects (dislocations). Adapted from Ref. [1].

where $\Delta B = 1$, $t = 1/2$, $v = 1/3$, though they can be adjusted to fit a particular free energy better ([12]). The main feature determining the kind of PFC model being used is the choice of C_2, which controls the elastic properties of the solid. Usually, $C_2(\vec{r}, \vec{r}') = C_2(|\vec{r} - \vec{r}'|)$; that is, the interaction between atoms only depends on the distance between them. For all of the problems studied in this work, $M(\vec{r}) = 0$.

In the original work [39], the second order correlation function is replaced by a function which matches the height and position of the first peak in Fourier space of the fourier transform of an isotropic correlation function; that is $\hat{C}_2(k) = \hat{C}_{20} + \hat{C}_{22}k^2 + \hat{C}_{24}k^4$. This translates to writing the excess energy term as a power series of gradients in real space:

$$F_{PFC} = \int_V f_{PFC} d\vec{r} \quad = \int_V \tfrac{B_L}{2} n^2 - \tfrac{t}{3} n^3 + \tfrac{v}{4} n^4 + B_X \tfrac{n}{2} (2\nabla^2 + \nabla^4) n d\vec{r} \tag{2.7}$$

where the constants $\hat{C}_{20}$, $\hat{C}_{22}$ $\hat{C}_{24}$ have been chosen so that a single value B_X can be used and $B_L = \Delta B + B_X$. In general, B_X and B_L are the isothermal compressibilities of the solid and liquid respectively [12]. Although the cubic term is dropped in [39] and [1], it is kept because it can be motivated from CDFT. The structures that result from this free energy are shown in Fig. 2.1. It should be noted that this form can be guessed from various pattern formation models such as the the Swift-Hohenberg model [39, 1, 134], which is identical to Eq. 2.7.

2.2.1 Phase Diagram

The phase diagram of the basic model can be approximated by a one-mode expansion of the density. In 2D, for instance, the following form for the density field can be used:

$$n = 2\phi(cos(\vec{q}_1 \cdot \vec{r}) + cos(\vec{q}_2 \cdot \vec{r}) + cos(\vec{q}_3 \cdot \vec{r})) + n_o \tag{2.8}$$

where ϕ is amplitude of the density oscillation, n_o is the average density, and $\vec{q}_i = q(\cos(2\pi/3i)\hat{x} + \sin(2\pi/3i)\hat{y})$ are the wave vectors, which obey $|q_i| = q$ and $\vec{q}_1 + \vec{q}_2 + \vec{q}_3 = 0$. Substituting this

expression into Eq. 2.7, and noting that all non-constant terms average to 0 over the integral, gives:

$$\begin{aligned} f &= \frac{F_{PFC}}{V} = \frac{1}{V}\int_V B_L\left(\frac{n_o^2}{2}+3\phi^2\right) - t\left(\frac{n_o^3}{3}+2n_o\phi^2+6\phi^3\right) \\ &+ v\left(\frac{n_o^4}{4}+9n_o^2\phi^2+12n_o\phi^3+\frac{45}{2}\phi^4\right)+3B_X\phi(-2q^2+q^4)\phi d\vec{r} \\ &= B_L\left(\frac{n_o^2}{2}+3\phi^2\right) - t\left(\frac{n_o^3}{3}+2n_o\phi^2+4\phi^3\right) \\ &+ v\left(\frac{n_o^4}{4}+9n_o^2\phi^2+12n_o\phi^3+\frac{45}{2}\phi^4\right)+3B_X(-2q^2+q^4)\phi^2 \end{aligned} \tag{2.9}$$

The parameters q or ϕ are not conserved when the free energy is minimized, so to find their values, the derivative can be taken and set to 0:

$$\begin{aligned} \frac{\partial f}{\partial q} = 12B_X\phi^2(-q+q^3) = 0 \\ \Rightarrow q = 0, \pm 1 \end{aligned}$$

$q = 0$ corresponds to constant (fluid) phase, while it is a local maximum for a given ϕ, where $q = \pm 1$ are equivalent and correspond to a solid phase. Substituting in $q = 1$ into the free energy and minimizing it with respect to amplitude gives:

$$\begin{aligned} \frac{\partial f}{\partial \phi} = 6B_L\phi - t\left(4n_o\phi+12\phi^2\right)+v\left(18n_o^2\phi+36n_o\phi^2+90\phi^3\right)-6B_X\phi = 0 \\ \Rightarrow \phi = 0, \frac{t-3vn_0 \pm \sqrt{t^2+24tvn_o-36v^2n^2-15v\Delta B}}{15v} \end{aligned} \tag{2.10}$$

For the solid phase, $\phi = \phi_0$ (the non-zero root giving the minimal free energy) and $n_o = n_s$.

For the liquid phase the free energy is trivial, with $\phi = 0$ and $n_o = n_l$, giving the following free energy:

$$f_l = B_L\frac{n_o^2}{2} - t\frac{n_o^3}{3} + v\frac{n_o^4}{4}$$

To find coexistence between the solid and liquid phases, we use the common tangent construction and solve the resulting equations numerically:

$$\begin{aligned} \left(\frac{\partial f}{\partial n_0}\right)_{n_o=n_s,\phi=\phi_0} &= \mu_n(n_s,\phi=\phi_0) \qquad = \left(\tfrac{\partial f}{\partial n_0}\right)_{n_o=n_l,\phi=0} = \mu_n(n_l,\phi=0) \\ f(\phi=0,n_o=n_l)-\mu_n(n_l,\phi=0)n_l &= f(\phi=\phi_0,n_o=n_s)-\mu_n(n_l,\phi=0)n_s \end{aligned} \tag{2.11}$$

There are also other phases present (stripe in any dimension greater than or equal to 1 and BCC in 3D), but because the focus of the thesis is on 2D metallic materials, they are just briefly mentioned in this report. Their phase boundaries are found in a way similar to that used to find the 2D solid-liquid transition. A phase diagram (including the 1-mode analysis shown above) for a 2D material is contained in Fig. 2.2.

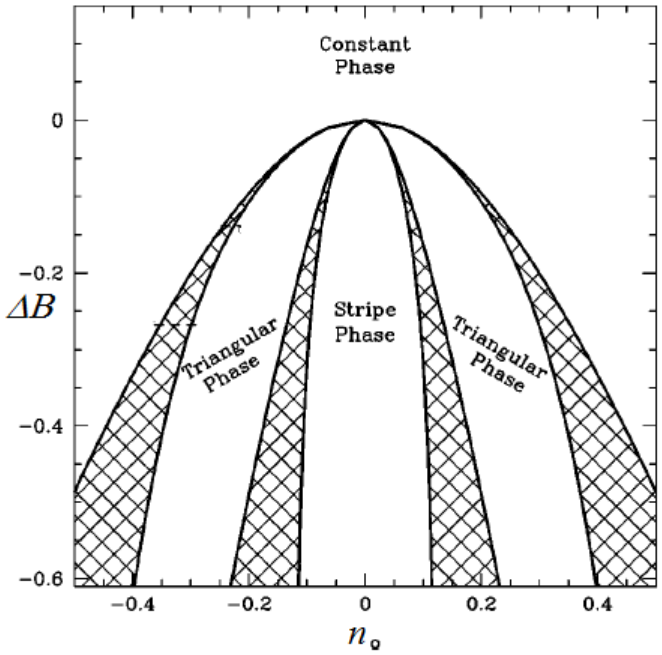

Figure 2.2: 2D PFC pure material phase diagram for $t = 0$, $v = 1$, $B_X = 1$. The hashed regions correspond to coexistence regions. Adapted from Ref. [1].

2.2.2 Dynamics

Typically, dissipative dynamics of conserved fields (model B) are assumed for the evolution of the density field [99]. The dynamics of the model can be written as:

$$\frac{\partial n}{\partial t} = \nabla^2 \left(\frac{\delta F_{PFC}}{\delta n} \right) + \eta = \nabla^2 \left(B_L n - t n^2 + v n^3 + B_X (2\nabla^2 + \nabla^4) n \right) + \eta \tag{2.12}$$

where the functional derivative for a functional depending on n and powers of gradients of it is defined as:

$$\frac{\delta F_{PFC}}{\delta n} = \sum_{i=0}^{\infty} (-1)^i \nabla^i \frac{\partial f_{PFC}}{\partial \nabla^i n} \tag{2.13}$$

f_{PFC} is the local free energy density. η is a noise term representing thermal fluctuations. Its average is 0 and it obeys fluctuation dissipation theorem, such that $< \eta(\vec{r}', t')\eta(\vec{r}', t') >= -2\rho_0 K_B T \nabla^2 \delta(\vec{r} - \vec{r}')\delta(t - t')$ [134]. For most simulations, this term is set equal to 0. These evolution equations accurately capture the behaviour of the evolution of soft condensed matter systems and of other materials where elastic states evolve relatively slowly. To capture rapid elastic relaxation more accurately in metals, the following expression can be used:

$$\frac{\partial^2 n}{\partial t^2} + \beta \frac{\partial n}{\partial t} = \alpha^2 \nabla^2 \left(\frac{\delta F_{PFC}}{\delta n} \right) \tag{2.14}$$

where β and α determine how quickly the elastic waves propagate and dissipate [97, 98], respectively. Normally, this second time derivative term is chosen so that elastic field relax much more quickly, though not necessarily as quickly as phonons would allow, hence the use of the term "quasi-

phonon." The above equations are simplified from CDFT in which:

$$\begin{aligned}\frac{\partial^2\rho}{\partial t^2}+\beta\frac{\partial\rho}{\partial t} &= \alpha^2\nabla\cdot\left(\rho\nabla\frac{\delta F}{\delta\rho}\right)\\ \frac{\partial^2 n}{\partial t^2}+\beta\frac{\partial n}{\partial t} &= \alpha^2\nabla\cdot\left((1+n)\nabla\frac{\delta F_{PFC}}{\delta n}\right)\end{aligned}$$

see [133, 99].

To find equilibrium properties of a system, the density field can be evolved using a fictitious time according to model A dynamics,

$$\frac{\partial n}{\partial t}=-\left(\frac{\delta F_{PFC}}{\delta n}-\mu_{n0}\right) \tag{2.15}$$

where μ_{n0} is a control parameter, the chemical potential of the reservoir with which the system is in contact [38]. In the case that one wants to conserve the average value of n as opposed to evolving the system to a fixed chemical potential [38], the following equation can be used

$$\mu_{n0}=\frac{1}{V}\int_V\frac{\delta F_{PFC}}{\delta n}d\vec{r} \tag{2.16}$$

2.3 PFC Model of a Binary Alloy

The first PFC studies of binary alloys started with considering 2 density fields (one for each species) and an interaction term (e.g., Ref. [39]). Even in Elder et al [12], this was the starting point, from which a free energy functional in terms of a density field and a concentration field is derived:

$$F_{PFC}=\frac{F_1+F_2+F_{12}}{\rho_0 k_B T} \tag{2.17}$$

where

$$F_i=k_BT\int_V\rho_i\ln\left(\frac{\rho_i}{\rho_{i0}}\right)-\delta\rho_i-\frac{1}{2}\int_V\delta\rho_i(\vec{r})\delta\rho_i(\vec{r}')C_{ii}(\vec{r}-\vec{r}')d\vec{r}'d\vec{r} \tag{2.18}$$

and

$$F_{12}=-k_BT\int_V\int_V\int_V\delta\rho_1(\vec{r})\delta\rho_2(\vec{r}')C_{12}(\vec{r}-\vec{r}')d\vec{r}'d\vec{r} \tag{2.19}$$

where $C_{ij}(\vec{r}-\vec{r}')=-\frac{\delta F}{\delta\rho_i\delta\rho_j'}$

To derive a simpler PFC energy, the following substitutions can be made $n=(\rho_1+\rho_2)/\rho_0$, $c=(\rho_1-\rho_2)/\rho_0$, $\rho_0=\rho_{10}+\rho_{20}$ and $C_{ij}=C_0+R^2C_2k^2+R^4C_4k^4$ [135]. Making these substitutions, expanding the logarithms to 4^{th} order, and dropping constant terms (only differences in free energy control the physics) result in the following free energy:

$$F_{PFC}=\int_V\frac{n}{2}(B_L+B_X(2R^2\nabla^2+R^4\nabla^4))n-\frac{t}{3}n^3+\frac{v}{4}n^4+\frac{w}{2}c^2+\frac{u}{4}c^4+\frac{K_c}{2}|\nabla c|^2d\vec{r}$$

where the symbols found in the pure material (B_L, B_X, t, v) have the same meaning in Eq. 2.7 as here and w is related to the energy of mixing of the 2 species, K_c is related to w and the spacing of atoms, and u ensures that the free energy is capped. In Elder et al 2007, B_L is expanded as $B_0^L+B_2^Lc^2$ and the spatial dimensions are rescaled such that $R=1+\alpha c$, which can be expanded to linear order, where α is the Vegard's law parameter [12, 135]: This gives the alloy PFC free energy

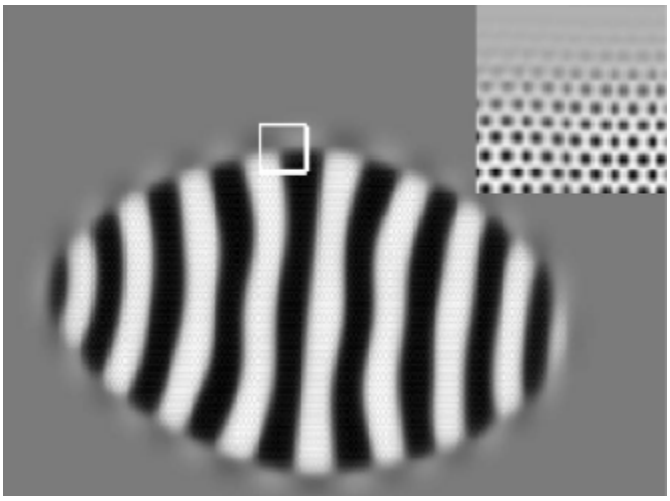

Figure 2.3: Concentration image (dark - $c < 0$, light - $c > 0$) of 2D PFC binary eutectic crystal growth for $B_0^L = 1.0248$, $t = 3/5$, $v = 1$, $B_X = 1$, $B_2^L = -9/5$ $u = 4$, $w = 0.008$, $\alpha = 1/4$, $K_c = 4$, average $c = 0$. Inset shows the density field of a small region. Adapted from [12].

functional of the form

$$\begin{aligned} F_{PFC} &= \int_V \frac{n}{2}(B_0^L + B_2^L c^2 + B_X(2(1+\alpha c)^2\nabla^2 + (1+\alpha c)^4\nabla^4))n - \frac{t}{3}n^3 + \frac{v}{4}n^4 \\ &+ \frac{w}{2}c^2 + \frac{u}{4}c^4 + \frac{K_c}{2}|\nabla c|^2 d\vec{r} \end{aligned} \tag{2.20}$$

2.3.1 Phase Diagram

Neglecting density changes between the solid and liquid, we can approximate the fields as:

$$\begin{aligned} n &= 2\phi(cos(\vec{q}_1 \cdot \vec{r}) + cos(\vec{q}_2 \cdot \vec{r}) + cos(\vec{q}_3 \cdot \vec{r})) \\ c &= c \end{aligned}$$

where $\vec{q}_i = q(cos(2\pi/3i)\hat{x} + sin(2\pi/3i)\hat{y})$ such that $|q_i| = q$ and $\vec{q}_1 + \vec{q}_2 + \vec{q}_3 = 0$, and ϕ is a constant. Substituting this expression into Eq. 2.20, and noting that non-constant terms average to 0 over the integral, gives:

$$\begin{aligned} f &= \frac{F_{PFC}}{V} = 3(B_0^L + B_2^L c^2)\phi^2 \\ &- 4t\phi^3 + \frac{45v}{2}\phi^4 + 3B_X(-2(1+\alpha c)^2 q^2 + (1+\alpha c)^4 q^4)\phi^2 + \frac{w}{2}c^2 + \frac{u}{4}c^4 \end{aligned} \tag{2.21}$$

The parameters q or ϕ are not conserved when the free energy is minimized, so to find the values at equilibrium, the derivative can be taken and set to 0:

$$\begin{aligned} \frac{\partial f}{\partial q} &= 12B_X\phi^2(-q + q^3) = 0 \\ &\Rightarrow q = 0, \pm(1+\alpha c) \end{aligned}$$

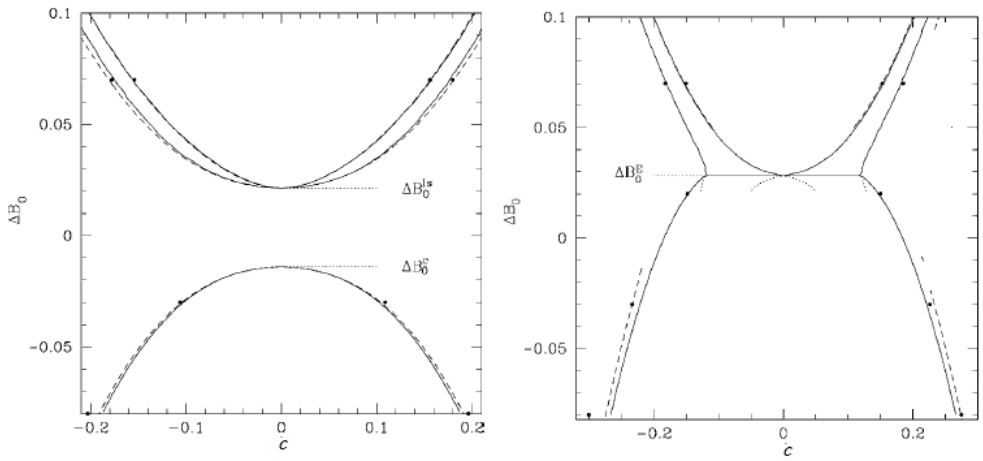

Figure 2.4: 2D PFC binary material phase diagram for $t = 3/5$, $v = 1$, $B_X = 1$, $B_2^L = -9/5$ $u = 4$ and average fields $n = 0$. Spinodal phase diagram on the left ($w = 0.088$) and eutectic on the right ($w = 0.008$). Adapted from [12].

We notice that there is also a possible phase with wave vector $q = 1 + \alpha c$; that is, the spacing of atoms changes with concentration. Let us invoke $\alpha = 0$, resulting in $q = 1$. Substuting in $q = 1$ into the free energy and minimizing it with respect to amplitude gives:

$$\frac{\partial f}{\partial \phi} = 6(B_0^L + B_2^L c^2)\phi - 12t\phi^2 + 90v\phi^4 - 6B_X\phi = 0$$
$$\Rightarrow \phi = 0, \frac{t \pm \sqrt{t^2 - 15v\Delta B}}{15v} \tag{2.22}$$

where $\Delta B = B_0^L - B_X + B_2^L c^2$ For the solid phase, $\phi = \phi_0$ (the non-zero root giving the minimal free energy, which with $t > 0$ is the plus root) and $c = c_s$.

Similiarly, for the liquid phase, $\phi = 0$ and $c = c_l$, giving the following free energy:

$$f_l = w\frac{c_l^2}{2} + u\frac{c_l}{4}$$

To find coexistence between the solid and liquid phases, we use the common tangent construction and solve the resulting equations numerically:

$$\left(\frac{\partial f}{\partial c}\right)_{c=c_s,\phi=\phi_0} = \mu_c(c_s, \phi = \phi_0) = \left(\frac{\partial f}{\partial c}\right)_{c=c_l,\phi=0} = \mu_c(c_l, \phi = 0)$$
$$f(\phi = 0, c = c_l) - mu_c(n_l, \phi = 0)c_l = f(\phi = \phi_0, c = c_s) - mu_c(c_l, \phi = 0)c_s$$

A phase diagram for a spinodal and eutectic material obtained with this model are contained in Fig. 2.4

2.3.2 Dynamics

As with the pure material, diffusive dynamics (model B) is the starting point.

$$\frac{\partial n}{\partial t} = \nabla^2 \left(\frac{\delta F_{PFC}}{\delta n}\right) + \eta_n \tag{2.23}$$

$$\frac{\partial c}{\partial t} = \nabla^2 \left(\frac{\delta F_{PFC}}{\delta c}\right) + \eta_c \tag{2.24}$$

where η_i are noise terms representing thermal fluctuations. Its average is 0 and it obeys fluctuation dissipation theorem where $< \eta_i(\vec{r}', t')\eta_i(\vec{r}', t') > \propto M_i K_B T \nabla^2 \delta(\vec{r} - \vec{r}')\delta(t - t')$. As with the pure material, this term is set to 0 in this thesis. These equations can also be derived from the dynamic density functional theory equations [99] or simply equations for 2 densities (see Ref. [135]). To not only capture elasticity more accurately in metals, but also mass transport in rapid phase transformations, the following equations of motion,

$$\frac{\partial^2 n}{\partial t^2} + \beta_n \frac{\partial n}{\partial t} = \alpha_n^2 \nabla^2 \left(\frac{\delta F_{PFC}}{\delta n}\right)$$

$$\frac{\partial^2 c}{\partial t^2} + \beta_c \frac{\partial c}{\partial t} = \alpha_c^2 \nabla^2 \left(\frac{\delta F_{PFC}}{\delta c}\right)$$

have been shown to filed accurate results in with regards to solute trapping and drag, through the parameters β_i and α_i [116].

To find equilibrium states of a system more quickly, the density and concentrations fields can be evolved with model A:

$$\frac{\partial n}{\partial t} = -\left(\frac{\delta F_{PFC}}{\delta n} - \mu_{n0}\right) \tag{2.25}$$

$$\frac{\partial c}{\partial t} = -\left(\frac{\delta F_{PFC}}{\delta c} - \mu_{c0}\right) \tag{2.26}$$

where μ_{n0} and μ_{c0} are control parameters, the chemical potentials of n and c fields in the reservoir with which the system is in contact, resepctively [16].

2.4 XPFC Model

Because the original PFC model is primarly limited to simulate predominantly 1-mode structures [108], another model needs to be used to easily and quantitatively capture more complex crystal structures. To have greater control of the structures, the XPFC model was developed by Greenwood et al [110, 111]. The free energy in all XPFC models has the form of Eq. 2.1. For a pure material, the form is identical to Eq. 2.6, though the notation for the constants differs somewhat:

$$\begin{aligned} F &= \int_V \left\{ \frac{n^2}{2} - \eta \frac{n^3}{6} + \chi \frac{n^4}{12} \right. \\ &- \left. \frac{n}{2} \int_{V'} (C(|\vec{r} - \vec{r}'|) n(\vec{r}') d\vec{r}') \, d\vec{r} \right\} \end{aligned} \tag{2.27}$$

The parameters η and χ are chosen to fit the ideal free energy [110, 111].

The fourier transform of the correlation function in Eq. 2.27 is given by:

$$\hat{C}(k) = \sum_{i=1}^{N} P_i \exp\left(-D_i \sigma^2 k_i^2\right) \exp\left(-G_i (k - k_i)^2\right)$$

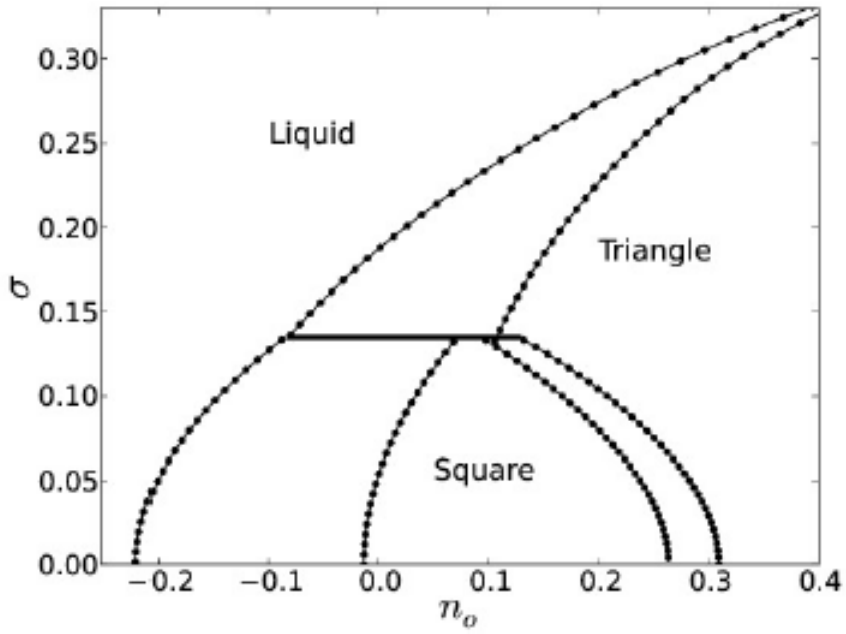

Figure 2.5: 2D XPFC pure material phase diagram with at different average densities and temperatures from [13]. Parameters are $\eta = 1.4$, $\chi = 1$, $k_1 = 2\pi$,$k_2 = 2\pi\sqrt{2}$, $G_1 = G_2 = 1/2$, $D_1 = k_1^2/4$,$D_2 = \sqrt{2}k_2^2/4$

where σ plays the role of a temperature field, D_i and G_i are constants specifying the how the Debye-Waller and elastic constants behave in the system, and N is the number of peaks in the system [110, 111].

Choosing an XPFC model with two peaks, a peritectic (liquid-square-triangle) can be obtained for the material. The phase diagram can be approximated in much the same way as the regular PFC model, except to make the calculations easier, the height of the second mode is often approximated as a fraction of the first mode (roughly half gives decent results in 2D and 3D) [113]. A sample phase diagram for the pure material is contained in Fig. 2.5.

The XPFC model can easily be generalized to multicomponent systems. Defining the normalized density in the same way as in Eq. 2.20 and $c = \rho_2/(\rho_1 + \rho_2)$, a simple functional for a binary alloy is:

$$\begin{aligned} F &= \int_V \left\{ \frac{n^2}{2} - \eta\frac{n^3}{6} + \chi\frac{n^4}{12} \right. \\ &+ \omega(1+n)(c\ln(c/c_0) + (1-c)\ln((1-c)/(1-c_0))) \\ &- \left. \frac{n}{2}\int_{V'} (C_{eff}(\vec{r}-\vec{r}')n(\vec{r}')d\vec{r}') + \alpha\frac{|\nabla c|^2}{2}\, d\vec{r} \right\} \end{aligned} \tag{2.28}$$

where η and χ are, as in the pure material, prefactors to fit the ideal free energy, ω and c_0 determine the strength of the entropy of mixing, and α is a constant related to the two-point correlation function, which is here taken as a constant for the concentration [113]. The effective correlation function is defined as:

$$C_{eff} = g(c)C_{11} + (1-g(c))C_{22},$$

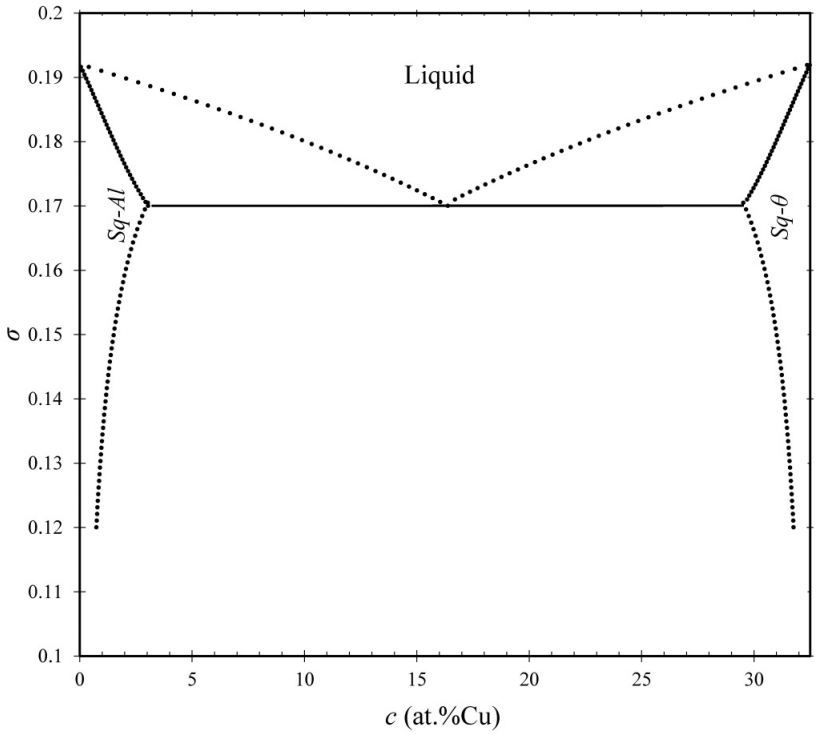

Figure 2.6: 2D XPFC alloy eutectic phase diagram in which both phases have a square crystal structure from [14]. The parameters are $\eta = 1.4$, $\chi = 1$, $k_{1,1} = 2\pi$, $k_{1,2} = \sqrt{2}k_{1,1}$, $k_{2,1} = 81/38\pi$, $k_{1,2} = \sqrt{2}k_{2,1}$, $D_{1,1}k_{1,1}^2 = D_{2,1}k_{2,1}^2 = D_{1,2}k_{1,2}^2 = D_{2,2}k_{2,2}^2 = 400/121$, $G_{1,1} = G_{2,1} = 5/24$, $G_{1,2} = G_{2,2} = 5/48$, $\eta = 1.4$, $\chi = 1$, $\omega = 0.008$, $c_0 = 0.5$, $\lambda = 0$.

$$g(c) \quad = \quad 1 - \lambda c + (3 + \lambda)c^2 + 4$$

where $g(c)$ is a function that interpolates between 0 when $c = 0$ and 1 when $c = 1$ and where λ is the energy of mixing in the solid phases. The fourier transform of these correlation functions is given by:

$$\hat{C}_{xx}(k) = \sum_{i=1}^{N} P_{xx,i} \exp\left(-D_{xx,i}\sigma^2 k_{xx,i}^2\right) \exp\left(-G_{xx,i}(k - k_{xx,i})^2\right)$$

where $P_{xx,i}$, $D_{xx,i}$, and $G_{xx,i}$ retain the same meanings in each pure phase xx as described for an individual peak in the pure material. An example of a binary phase diagram is given in Fig. 2.6. It should be noted that this phase behaviour is accurate in the limiting case of a pure material; that is, the solidus and liquidus lines converge at respective melting points. Also, other kinds of realistic phase diagrams can be made with this model, including ones in which the materials have different crystal structures [113].

Finally, we note that a free energy for a ternary material can be written in much the same way as a binary material, where the normalized density is $n = (\rho_1 + \rho_2 + \rho_3)/\rho_0 = \rho_t/\rho_0 - 1$ and the two concentrations are $c_2 = \rho_2/\rho_t$ and $c_3 = \rho_3/\rho_t$. Noting that $c_1 = 1 - c_2 - c_3$, the free energy is written as follows:

$$F \quad = \quad \int_V \left\{ \frac{n^2}{2} - \eta\frac{n^3}{6} + \chi\frac{n^4}{12} \right.$$

$$
\begin{aligned}
&+ \quad \omega(1+n)\left[\sum_{i=1}^{3} c_i \ln\left(\frac{c_i}{c_{io}}\right)\right] \\
&- \quad \frac{n}{2}\int_{V'}(C_{eff}(\vec{r}-\vec{r}')n(\vec{r}')d\vec{r}') + \sum_{i,j=1}^{3}\frac{\alpha_{ij}}{2}\nabla c_i \cdot \nabla c_j, d\vec{r}\Bigg\}
\end{aligned} \tag{2.29}
$$

where η and χ are defined the same as in Eq. 2.28, ω and c_{i0} determine the strength of the entropy of mixing, and α_{ij} is a constant related to the two-point correlation functions, which are here taken as constants; normally for the off-diagonal concentration gradient prefactors, $\alpha_{i,j} = 0$ [118]. The effective correlation function is interpolated between the different concentrations as:

$$
\begin{aligned}
C_{eff} &= \sum_i g_i(c_1, c_2, c_3) C_{ii}, \\
g_i(c_1, c_2, c_3) &= 1 + \sum_{j\neq i}(-3c_j^2 + 2c_j^3) - 4c_i \Pi_{j\neq i} c_j - \lambda(c_1c_2 + c_2c_3 + c_3c_1)
\end{aligned} \tag{2.30}
$$

where λ is a tunable parameter related to the interactions between atoms.

2.4.1 Dynamics

For XPFC alloy dynamics, once again,the functional derivative of the free energy is taken to determine the chemical potential of each field. For the problems studied, diffusive dynamics is used [118]:

$$
\begin{aligned}
\frac{\partial n}{\partial t} &= \nabla^2\left(\tfrac{\delta F_{PFC}}{\delta n}\right) + \eta_n \\
\frac{\partial c_i}{\partial t} &= M_{ci}\nabla^2\left(\tfrac{\delta F_{PFC}}{\delta c_i}\right) + \eta_{c_i}
\end{aligned} \tag{2.31}
$$

A mobility term is introduced for the concentration field so that it can evolve at a different rate from the density field. The noise term is chosen to have a mean of 0 and to obey flucutation dissipation theorem, that is $< \eta_i(\vec{r}, t)\eta_i(\vec{r}', t') > \propto M_i k_B T \nabla^2 \delta(\vec{r}-\vec{r}')\delta(t-t')$. The concentrations must add up to 1, so typically, one of the concentrations is solved for in terms of the other variables and its evolution equation is neglected. An image of ternary alloy solidification is shown in Fig. 2.7.

2.5 Amplitude model

An amplitude model is a model in which the phase field crystal equations are described in terms of more slowly varying fields. These fields are the average density and concentration(s), and the ampltiudes of the modes describing the crystal structures. It relies on the assumption of the average fields being described varying more slowly than the atomic variation ([122]). There are three main approaches for deriving ampltiude models: the renormalization group approach [120, 121], the multiple scales expansion approach [15, 119, 122], and the volume-averaging coarse-graining approach [124, 125, 13]. The approaches give similar results, though some details may be left out as noted by [15, 19] and because of this, depending on the physics one wants to include in the amplitude model, some approaches better than others.

In this thesis, the volume-averaging approach is used [13]. In this approach, the local free energy density is converted to a free energy density, which varies on longer length scales via a smoothing convolution:

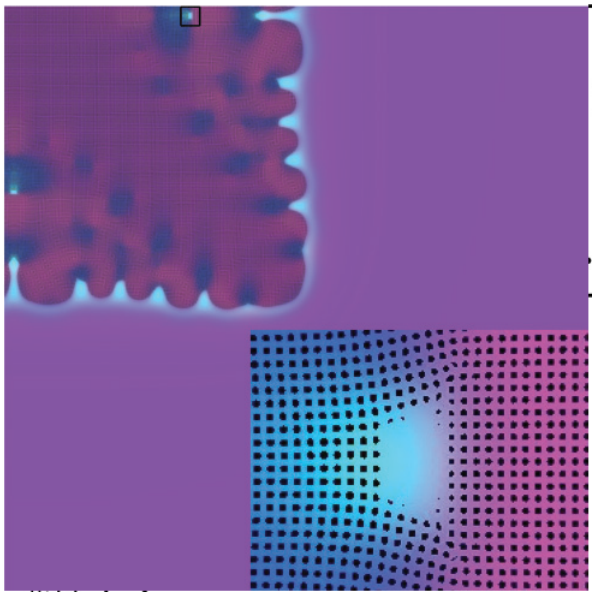

Figure 2.7: 2D ternary XPFC alloy simulation showing ternary alloy solidification. The simulation parameters are $\eta = 1.4$,$\chi = 1$,$\omega = 0.005$, $k_{1,1} = 81/38$, $k_{2,1} = 54/29\pi$,$k_{3,1} = 2\pi$,$k_{i,2} = \sqrt{2}k_{i,1}$ and $c_{io} = 0.3333$ for all i, $\sigma = 0.164$ $c_1 = 0.82$, $c_2 = 0.005$. In the inset, a close-up of a solidifying liquid pool is shown indicating how the density field is deformed due to atomic mismatch. From [13]

$$f(\vec{R}) = \int_V f(\vec{r})\chi(\vec{R} - \vec{r})d\vec{r} \tag{2.32}$$

where $\chi(\vec{R} - \vec{r})$ is weighting function, for which $\int_V \chi(\vec{r})d\vec{r} = 1$. For a convenient calculation, one might choose $\chi = 1/V_{unitcell}$ for all points within a unit cell from the point one is averaging and $\chi = 0$ outside of it, where $V_{unitcell}$ is the volume of the unit cell. Let us assume that the crystal contains a hexagonal symmetry substituting for the density,

$$n = n_o + \sum_{j=1}^{N} A_j \exp(i\vec{k}_j \cdot \vec{r}) + c.c. \tag{2.33}$$

where $N = 3$, the A_j are complex numbers and $c.c.$ denotes the complex conjugate of the terms already written in the expression. Applying Eq. 2.32 to Eq. 2.6 with the substiution of Eq. 2.33. Noting that any term with a factor of the form $\exp(i\vec{k} \cdot r)$ integrates to 0, this substitution gives,

$$\begin{aligned} F_{amp} &= \int_V B_L \left(\frac{n_o^2}{2} + \sum_{j=1}^{N} |A_j|^2 \right) - t \left(\frac{n_o^3}{3} + 4n_o \sum_{j=1}^{N} |A_j|^2 + 2(\prod_j^N A_j + \prod_j^N A_j^*) \right) \\ &+ v \left(\frac{n_o^4}{4} + 3n_o^2 \sum_{j=1}^{N} |A_j|^2 + 6n_o(\prod_j^N A_j + \prod_j^N A_j^*) + \frac{3}{2} \left(2[\sum_{l=1}^{N} |A_l|^2]^2 - |A_j|^4 \right) \right) \\ &+ C(\nabla^2; 0)\frac{n_0^2}{2} + A_j^* \sum_{j=1}^{N} C(\nabla^2 + 2i\vec{k}_j \cdot \nabla); \vec{k}_j) A_j d\vec{r} \end{aligned} \tag{2.34}$$

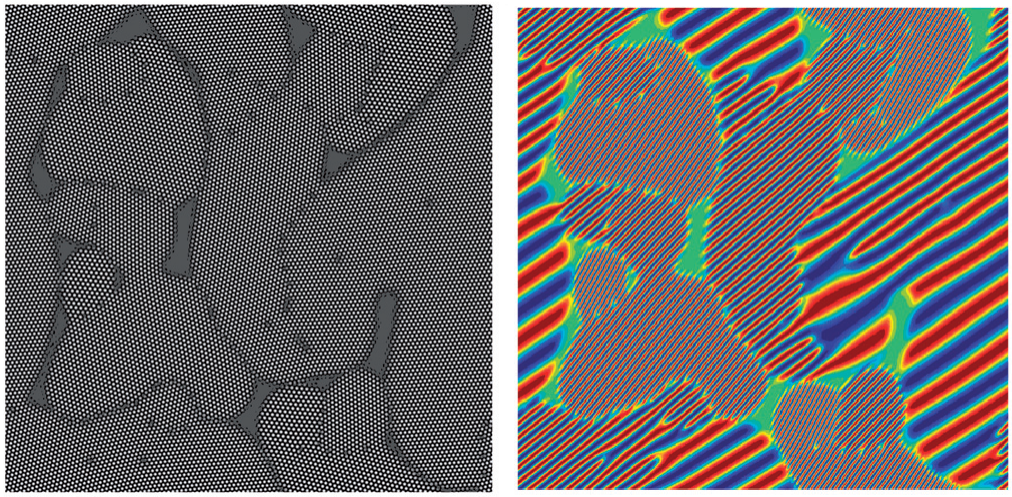

Figure 2.8: Solidification from many nuclei ([15]). Left - density field showing the individual grains, right - plot of real component of amplitude corresponding to $\vec{k}_j = -\sqrt{3/2}\hat{x} - 1/2\hat{y}$ showing how changes in amplitude gives different crystal orientations.

where $*$ denotes complex conjugate and $C(\nabla^2 + 2i\vec{q}\cdot\nabla;\vec{q}) = \sum_{l=0}^{\infty} \frac{(-1)^l}{l!} \frac{\partial \hat{C}(k)}{\partial k^2}|_{\vec{k}=\vec{q}} (\nabla^2 + 2i\vec{q}\cdot\nabla)^l$. The sum in the correlation function terms is that of a long-wave limit correlation function, which is typically a truncation of the gradient series expansion for the full correlation function (cf. Ref. [13]). For different crystal structures, the polynomial terms will be different. However, the terms which result from the coarse-graining of the correlation function terms can always be written in a similar form to that written above.

To obtain evolution equations for the amplified and average density fields, model C dynamics is used,

$$\begin{aligned} \frac{\partial n_o}{\partial t} &= \nabla^2 \left(\frac{\delta F_{amp}}{\delta n_o} \right) \\ \frac{\partial A_j}{\partial t} &= \nabla^2 \left(\frac{\delta F_{amp}}{\delta A_j^*} \right), j = 1..N \end{aligned} \tag{2.35}$$

An image showing how these equations simulate polycrystals is given in Fig. 2.8.

A similar process can be done to get an amplitude model for a binary alloy. Consider the following expansion to describe the density and concentration fields:

$$n = \sum_{j=1}^{N} A_j \exp(i\vec{k}_j \cdot \vec{r}) + c.c. \tag{2.36}$$

$$c = c_o \tag{2.37}$$

Applying the above substitution in Eq. 2.20 and applying Eq. 2.32, results in:

$$F_{amp} = \int_V (B_L - B_X) \sum_{j=1}^{N} |A_j|^2 - 2t(\prod_j^N A_j + \prod_j^N A_j^*) + v\frac{3}{2}\left(2[\sum_{l=1}^{N} |A_l|^2]^2 - |A_j|^4 \right)$$

$$
\begin{aligned}
&+ \quad B_X \sum_{j=1}^{N} A_j^*(-\nabla^2 - 2i\vec{k}_j \cdot \vec{r})^2 A_j \\
&+ \quad \left(B_2^L 2 \sum_{j=1}^{N} |A_j|^2 + w \right) \frac{c_o^2}{2} + u\frac{c_o^4}{4} + K_c \frac{|\nabla c_o|^2}{2} d\vec{r}
\end{aligned} \tag{2.38}
$$

It should be noted that the gradient terms in Eq. 2.38 are directly relatable to the more general expressions in Eq. 2.34. Once again, model C dynamics can be used to simulate the evolution of the fields:

$$
\begin{aligned}
\frac{\partial c_o}{\partial t} &= \nabla^2 \left(\frac{\delta F_{amp}}{\delta c_o} \right) \\
\frac{\partial A_j}{\partial t} &= \nabla^2 \left(\frac{\delta F_{amp}}{\delta A_j^*} \right), j = 1..N
\end{aligned} \tag{2.39}
$$

For an alternate approach, see appendix A.

2.5.1 Derivation of Phase Field Models from Amplitude Models

Phase field models have been successfully employed to a number of phase transition problems (for a review, see Ref. [136]), though they have been developed phenomenologically. Through the PFC ampltiude model, it can be demonstrated that phase field models are derivable from more fundamental theories [119]. To proceed with this derivation, the following form is chosen for the ampltiudes in an amplitude model: $A_j = \phi \exp(i\vec{k}_j \cdot \vec{u})$, where $\vec{u}$ is the displacement field and ϕ is the mangitude of the amplitude ([119]). If this substitution is made into Eq. 2.38, then the following equation results:

$$
\begin{aligned}
f_{PF} &= 3(B_L - B_X)\phi^2 - 4t\phi^3 + 45v\phi^4/2 + 6B^X|\nabla\phi|^2 + \left(6B_2^L\phi^2 + w\right)\frac{c_o^2}{2} + w\frac{c_o^4}{4} \\
&+ \quad K_c\frac{|\nabla c_o|^2}{2} + 3B_X\left(\frac{3}{2}(U_{xx}^2 + U_{yy}^2) + U_{xx}U_{yy} + 2U_{xy}^2\right) \\
&+ \quad 12B_X\alpha c_o\left(-\phi\nabla^2\phi + (U_{xx} + U_{yy})\phi^2\right)
\end{aligned} \tag{2.40}
$$

where the strains are $U_{ij} = \frac{1}{2}\left(\frac{\partial u_i}{\partial x_j} + \frac{\partial u_j}{\partial x_i}\right)$ [119]. Model C can be used for the dynamical equations of the density and concentration fields:

$$
\begin{aligned}
\frac{\partial c_o}{\partial t} &= \nabla^2 \left(\frac{\delta F_{PF}}{\delta c_o} \right) \\
\frac{\partial \phi}{\partial t} &= \nabla^2 \left(\frac{\delta F_{PF}}{\delta \phi} \right)
\end{aligned} \tag{2.41}
$$

To solve for the displacements, mechanical equilibrium is assumed at each time step. This is expressed using Einstein summation notation as:

$$
\frac{\partial \sigma_{ij}}{\partial x} = \frac{\partial}{\partial x}\frac{\delta F}{\delta U_{ij}} = 0 \tag{2.42}
$$

where σ_{ij} are the stress fields [137]. It should be noted that the driving force on ϕ in Eq. 2.41 is different by a factor of 6 on from the average driving force acting on the A_j's in Eq. 2.39.

Chapter 3

Grain Boundary Thermodynamics in Alloys

3.1 Introduction

As indicated in sections 1.2 and 2.1, the PFC formalism is an appropriate way of studying problems relating to grain boundary thermodynamics. There have been a few PFC studies concerned with grain boundary properties in pure materials (e.g., [1], [2], [38], [54], and [53]), and alloys (e.g., [17], [16]). In this part of the thesis, the grain boundary properties of two binary alloy PFC-type models (those of Refs. [12] and [113]) are studied. The results for the grain boundary thermodynamics section of this chapter are contained in Stolle et al [16]. The results of grain boundary pre-melting in alloys are contained in Power et al [138].

3.2 Grain boundary thermodynamics

The first PFC model used in this grain boundary premelting study is the one derived by [12]. It is described in more detail in section 2.3 and will not be repeated here. The equations of motion for the diffusive dynamics of density, n, and concentration, ψ, are given by Eqns. 2.23 and 2.24; note that the notation for the original PFC model in this chapter differs from section 2.3 only in that ψ replaces c. These equations are simulated using the spectral method described in [1] and [38] for both the density and concentration fields. The grid spacing, Δx, was varied according to the solid concentration ψ_s, which does not vary much from the mean simulation concentration, ψ_0, such that there were roughly 8 grid points between atomic planes. The average concentration, ψ_0, was chosen in each simulation to lie between -0.2 and 0.1. Because the simulations were focused on the role of concentration, the initial average density was set to $n_0 = 0$. The temperature, B_0^L, was chosen in each run such that the undercooling was sufficient for the grain boundaries to close completely despite the disjoining pressure. A summary of the the parameters used for the bicrystal simulations is given in Table 3.1.

Each simulation was performed with periodic boundary conditions. A single bi-crystal was set up with roughly 10 grid points between each grain. For the least deep quench at a given, ψ_0, the simulation was cooled to the stated B_0^L. Otherwise, the simulations are first cooled to an intermediate temperature before proceeding with equilibrating the simulation at the final temperature. Each bicrystal is rotated by $\pm\theta$ from the 0° misorientation such that the full misorientation angle is θ. The misorientation angles are chosen such that for small angles, an integer number of dislocations fit excatly into the simulation grid. As can be inferred from there being 2 grain boundaries with periodic boundary conditions, their intial separation is $N_x/2$ grid points in each direction. At

$L_x/2 = 512\Delta x$, this means the interaction of the grain boundaries is negligible except possibly at 1.55°. In Fig. 3.1, examples of the density and concentration fields of low angle and a high angle grain boundaries are shown.

The simulations for each parameter range are run until the system is close to equilbrium. Close enough to equilibrium is determined by the standard deviation of the chemical potential of each field and the ratio of $s_{\mu x}$ to mean chemical potential, $\bar{\mu}_x$, where x is ψ or n. The average microscopic chemical potentials varying by roughly less than 10^{-5} and the ratio of the standard deviation to the mean value is less than 10^{-2} throughout the simulation domain. To meet this criterion, the similuations are run for 100000 timesteps for each set of simulation parameters.

Table 3.1: Table of Variables and Parameters for Grain boundary Thermodynamics PFC Simulations

Parameters	Values
Simulation Dimensions N_x, N_y	1024 (or 2048), 2048 (or 1024)
Equilibriation time N_t	100000
Grid Spacing and time increment Δx, Δt	$\pi/4\sqrt{(1-2\eta\psi_s)/(1-4\eta\psi_s)}$, 1.0
mean concentration ψ_0	-0.15, -0.05, 0, 0.1, and -0.2 (for large angles only)
mean density n_0	0
t, v, B^x	0.6, 1, 1
B_2^L, u, K_c	-1.8, 4, 4
w	0.008 (eutectic), 0.088 (spinodal)
mismatch η	0, 0.05, 0.1
Undercooling $(\Delta B_0^L)_{solidus} - \Delta B_0^L$	$\sim 0.02 - 0.06$
Misorientation angles θ	1.55°, 2.07°, 2.58°, 3.10°, 4.14°, 5.17°,6.20°, 8.23°, 10.3°, 12.5°, 15°, 17.5°, 20°, 22.5°, 25°,27.5°, 30°, 32.5°, 35°, 40°

Calculation of Grain Boundary Energy

The grain boundary energy, γ_{gb}, which is defined as the excess free energy per unit area of an interface as indicated in Eq. 1.7, as in can also be written in 2D as:

$$\begin{aligned} L_y\gamma_{gb} &= L_y w_{gb}\left(f_{gb} - \bar{\mu}_\psi\psi_{gb} - \bar{\mu}_n n_{gb}\right. \\ &- \left.\left(f_s - \bar{\mu}_\psi\psi_s - \bar{\mu}_n n_s\right)\right) \end{aligned} \tag{3.1}$$

where L_y is the length (area) of the grain boundary, w_{gb} is the width of the grain boundary region, f_{gb}, ψ_{gb}, n_{gb} are the free energy density, normalized density difference, and normalized density in a region that contains the grain boundary, and f_s, ψ_s, n_s are the free energy density, normalized density difference, and normalized density of the bulk solid region region. The bulk and excess intensive quantities can be calcluated as follows (with n and f replacing ψ for normalized density and free energy density calculations, respectively):

$$\begin{aligned} \psi_{gb} &= \frac{1}{L_y w_{gb}}\int_0^{L_y}\int_{x_{gb}-w_{gb}/2}^{x_{gb}+w_{gb}/2}\psi dxdy \\ \psi_s &= \frac{0.5L_x\psi_0 - w_{gb}\psi_{gb}}{0.5L_x - w_{gb}} \end{aligned} \tag{3.2}$$

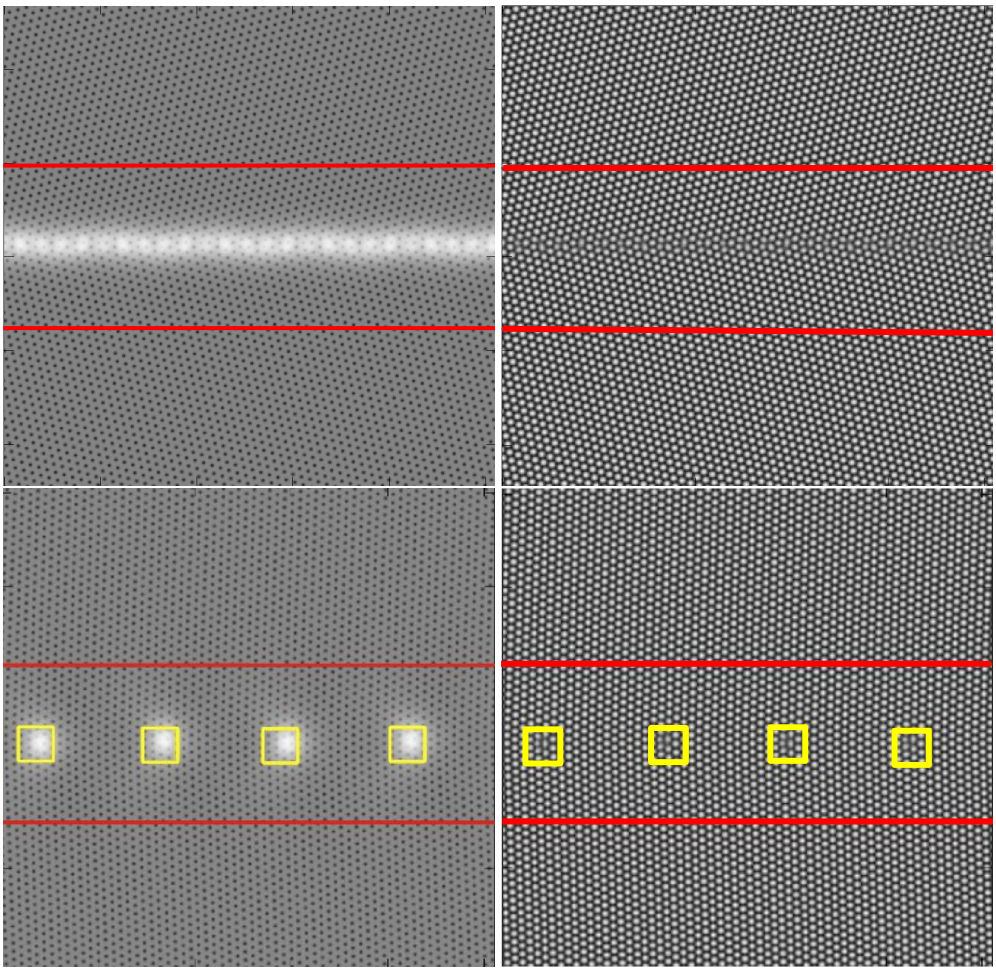

Figure 3.1: Concentration *(left frames)* and density fields *(right frames)* around low angle *(bottom frames)* and high angle *(top frames)* grain boundaries. The area between the two red lines is the grain boundary region, while the rest is bulk solid. The dislocations in the low angle grain boundary are indicated by yellow squares. The x-direction in simulations is the vertical direction in the figures. From [16].

Because ψ_s and n_s are close to the average system values ψ_0 and n_0, respectively, f_s can be written as a Taylor series about n_0 and ψ_0 as was done by [38], which gives

$$\begin{aligned} \gamma_{gb} &= w_{gb}\{f_{gb} - \bar{\mu}_\psi(\psi_{gb} - \psi_0) \\ &- \bar{\mu}_n(n_{gb} - n_0) - f_s(n_0, \psi_0)\} \end{aligned} \tag{3.3}$$

where $f_s(n_0, \psi_0)$ is the free energy density of the solid at a normalized density, n_0, and concentration, ψ_0.

To determine the grain boundary energy, we determine the energy of grain boundary energy region. One method of determining this quantity involves finding the position along the x-axis with the maximum free energy density, x_{gb}. Next, a region centred about x_{gb} of width, w_{gb}, needs to be chosen. For widths $w_{gb} \gtrsim 150\Delta x$, accurate approximations of the excess quantities could be found; for larger values of w_{gb}, calculating the excess quantities results in differences typically less than 1%. To simplify the calculations, $w_{gb} = L_x/2$. This choice was made in [38] and Eq. 3.3 becomes:

$$2\gamma_{gb} = L_x\{f_{gb} - f_s(n_0, \psi_0)\} \tag{3.4}$$

Still, f_s needs to be determined accurately, which [38] notes is rather difficult. One method for determining f_s is by extracting it from a fit using the theoretical low angle Read-Shockley relation, Eq. 1.10:

$$\gamma_{gb} = E_0\theta(A - \ln(\theta))$$

As noted by [1],

$$E_0 = \frac{Y_2 b}{8\pi\alpha} = \frac{B^X \phi^2 b}{\pi\alpha} \tag{3.5}$$

where ϕ is the amplitude of density field in the one mode approximation in the solid phase, Y_2 is the 2D Young's modulus, b is the Burger's vector of the dislocations, and $\alpha = \sqrt{3}/2$ accounts for the triangular geometry of the lattice. Making this substitution and fitting the free energy data up to $10.35°$ gives an estimate of A and f_s.* To verify the accuracy of this method, 2 angles ($4.14°$ and $27.8°$) were chosen to calculate the free energy of the system using the free energy from the fit and by a truncated scaling approach used in [38]. In this "scaling" approach, a linear relation is fit to data relating $1/L_x$ and f, where the slope $2\gamma_{gb}$ and the $1/L_x$-axis intercept is f_s. From Eq. 3.4, it is clear that the free energy density of the system is inversely proportional to the length of the system perpendicular to the grain boundary with the constant of proportionality being the grain boundary energy. A comparison of the results are shown below in Table 3.2.

Table 3.2: Comparing γ_{gb} calculation with "scaling" and low-angle fit methods)

θ	ψ_0	B_0^L	Low angle fit ω_s	Scaling ω_s	Low Angle Fit 2 γ_{gb}	Scaling 2 γ_{gb}
27.8	-0.15	1.035	0.0010421	0.0010420	0.0130	0.0130
27.8	-0.15	1.015	0.0005222	0.0005219	∼0.20	0.02055
27.8	-0.15	0.995	-0.0001354	-0.0001358	∼0.270	0.2717
27.8	0	1.002	-0.0002849	-0.0002849	∼0.0121	0.01207
27.8	0	0.962	-0.013299	-0.013302	∼0.26	0.02610
27.8	-0.05	1.006	-0.0001354	-0.0001796	∼0.0116	0.01161
4.14	-0.15	1.015	0.0005222	0.0005222	0.009501	0.009453

Figure 3.2 illustrates how well the low angle data fits to the theoretical Read Shockley relation, where $A = 1 + \ln(b/r_0)$ and $r_0 \approx 4.4$. All of the curves were scaled by a horizontal stretch factor

*Quantities determined with this method will be referred to as "low angle fit" quantities. To determine ω_s, $\omega_s = f_s - \mu_\psi\psi_s - \mu_n n_s$. N.b., the E_0 used in for the low angle fit, which is defined by Eq. 3.5, will be referred to as E_0^{low}

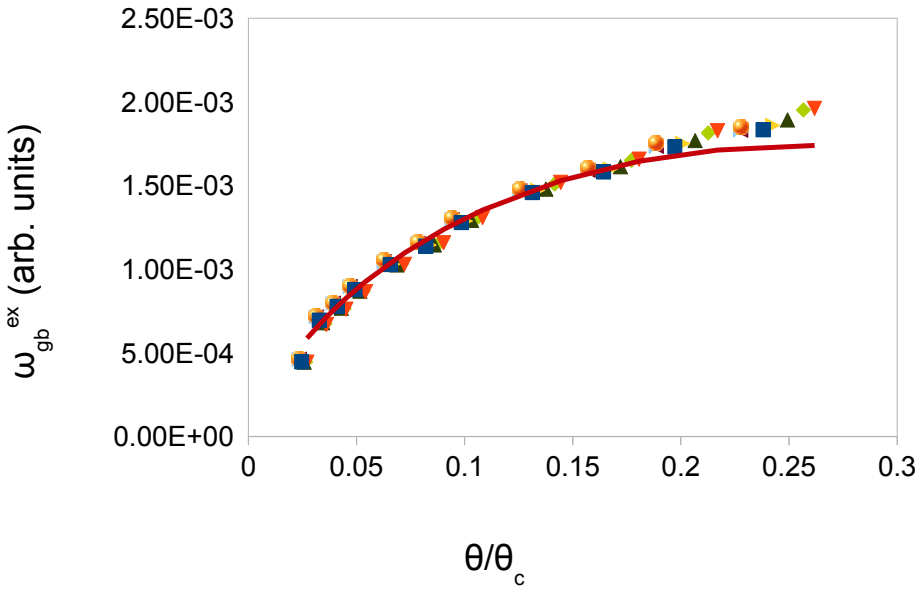

Figure 3.2: Alloy PFC model scaled grain boundary energy plot. The normalized grain boundary energy, $\omega_{gb} = \gamma_{gb}\Delta x\theta_c/(w_{gb}\phi^2)$, is plotted against the normalized bicrystal crystal misorientation, θ/θ_c, for different concentrations and temperatures for low angles, where $\theta_c = r_0\exp(0.5)/a$ is a horizontal stretch factor. For the reference curve, $\theta_c = 1$ and θ is given in radians. Read-Shockley reference curve (solid); $\psi_0 = 0$, $B_0^L = 1.002$ (squares); $\psi_0 = 0$, $B_0^L = 0.962$ (inverted triangle); $\psi_0 = -0.05$, $B_0^L = 0.996$ (right triangle); $\psi_0 = -0.05$, $B_0^L = 1.006$ (circle); $\psi_0 = 0.1$, $B_0^L = 1.015$ (left triangle); $\psi_0 = 0.1$, $B_0^L = 0.995$ (star); $\psi_0 = -0.15$, $B_0^L = 1.035$ (bow tie); $\psi_0 = -0.15$, $B_0^L = 1.015$ (triangle); $\psi_0 = -0.15$, $B_0^L = 0.005$ (diamond). From [16].

$\theta_c = r_0\exp(0.5)/a$ and normalized by their respective theoretical low angle E_0, E_0^{low}; that is in the Fig. 3.2, the normalized system free energy density plotted is defined as:

$$\omega_{normalized} = \frac{\omega}{E_0^{low}L_x}$$

The core energies for different average concentrations and undercoolings are shown in Fig. 3.3. The core radiii are roughly constant, though possibly decreasing with undercooling, $(\Delta B_0^L)_{solidus} - \Delta B_0^L$, which is constistent with the trend found in [38].

A number of other analyses were done using the full range of angles. Using the f_s determined above, the grain boundary energy data in Fig. 3.4 can be scaled (up to $40°$) onto one Read-Shockley curve ($A = 0.362$ and $E_0 = 1$). In particular, a vertical scaling factor $E' = E_0^m(B_0^L = 1.002, \psi_0 = 0)(\Delta x)/E_0^m(B_0^L, \psi_0)/w_{gb}$ is applied to the data, where the E_0^m values are determined by fitting the data to Eq. 1.10. The value E_0^m depends linearly on the theoretical value of E_0 for the spinodal ($w = 0.088$) data. This fact will be used to derive an expression for the segregation behaviour in the PFC model in section 3.2. Also, the core energy contribution was relatively insensitive to temperature for the spinodal phase diagram data, for which $A = 0.362$. It varies a lot for the eutectic ($w = 0.008$) materials. For example, for $\psi_0 = -0.2$, $A = 0.0.719, 0.467, 0.411$ for $B_0^L = 1.065, 1.045, 1.025$, respectively. While in the spinodal material grain boundary energy is

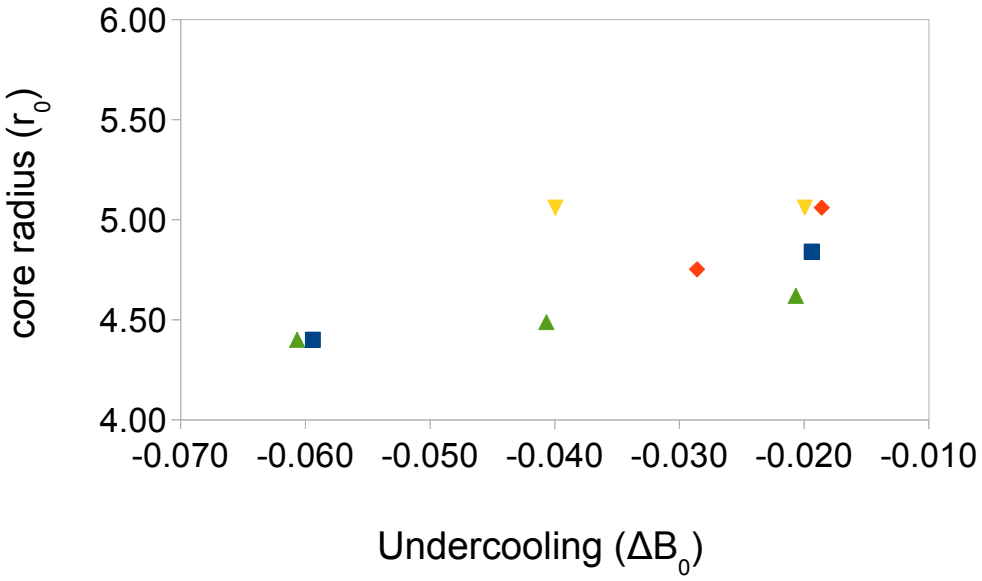

Figure 3.3: Core radius versus undercooling for different concentrations determined from low angle fit data of Fig. 3.2. Square (blue) - $\psi_0 = 0$; Diamond (red) - $\psi_0 = -0.05$; Upside down triangle (yellow) - $\psi_0 = 0.1$; Triangle (green) - $\psi_0 = -0.15$. From [16].

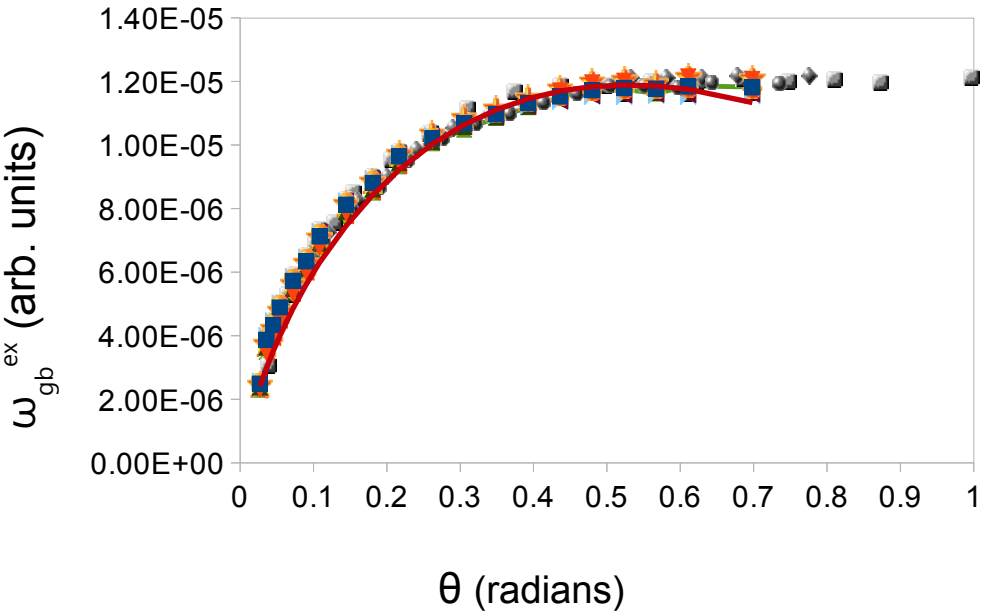

Figure 3.4: Scaled grain boundary energy for the PFC model. Scaled grain boundary energy, $\omega_{gb} = \gamma_{gb}E_0^m(B_0^L = 1.002, \psi_0 = 0)/(w_{gb}\Delta x E_0^m(B_0^L, \psi_0))$, vs. bicrystal crystal misorientation, θ/θ_c for different concentrations and temperatures. Empirical reference Read-Shockley curve (solid), θ/θ_c is in radians. Data for $w = 0.088$: $\psi_0 = 0$, $B_0^L = 1.002$ (squares); $\psi_0 = 0$, $B_0^L = 0.962$ (inverted triangle); $\psi_0 = -0.05$, $B_0^L = 0.996$ (right triangle); $\psi_0 = -0.05$, $B_0^L = 1.006$ (circle); $\psi_0 = 0.1$, $B_0^L = 1.015$ (left triangle); $\psi_0 = 0.1$, $B_0^L = 0.995$ (star); $\psi_0 = -0.15$, $B_0^L = 1.035$ (bow tie); $\psi_0 = -0.15$, $B_0^L = 1.015$ (triangle); $\psi_0 = -0.15$, $B_0^L = 0.995$ (diamond),$\psi_0 = -0.2$, $B_0^L = 1.045$ (graduated-shading circles). Data for $w = 0.008$: $\psi_0 = -0.2$, $B_0^L = 1.065$ (graduated-shading boxes), $\psi_0 = -0.2$, $B_0^L = 1.045$ (graduated-shading diamonds),$\psi_0 = -0.2$, $B_0^L = 1.025$ (line with ties). From [16].

mostly controlled by structural effects as indicated by the universality of the grain boundary energy curves with constant A, in the eutectic material, where solutal effects are stronger, solute segregation to the grain boundary has a noticeable effect on grain boundary thermodynamics. For all of these runs, there is no mismatch between the atomic species; i.e., $\eta = 0$.

It should also be noted that although grain boundary energy does not change much between an alloy and a pure material with the same elastic and structural properties, large changes in grain boundary energy can still be seen with undercooling. The effect of undercooling on grain boundary energy is shown in Fig. 3.5 for $w = 0.088$. To look at this effect, two concentrations, ψ_0, at the same B_0^L are compared; in this model, increasing $|\psi_0|$ means increasing undercooling at the same temperature (see section 2.3 for specific phase diagrams).

The effect of mismatch is studied for $B_0^L = 1.015$ and $w = 0.088$. As expected by the formula for the elastic moduli, grain boundary energy did not change much due to mismatch. Namely, the E_0 is related to ϕ, which does not change much with η—the grain boundary energy does not change much as is shown in Fig. 3.6. As well, the amount of solute segregation to the grain boundary does not change much either. There are some exceptions. For $4.14° - 8.28°$ at $\eta = 0.05$, the grain

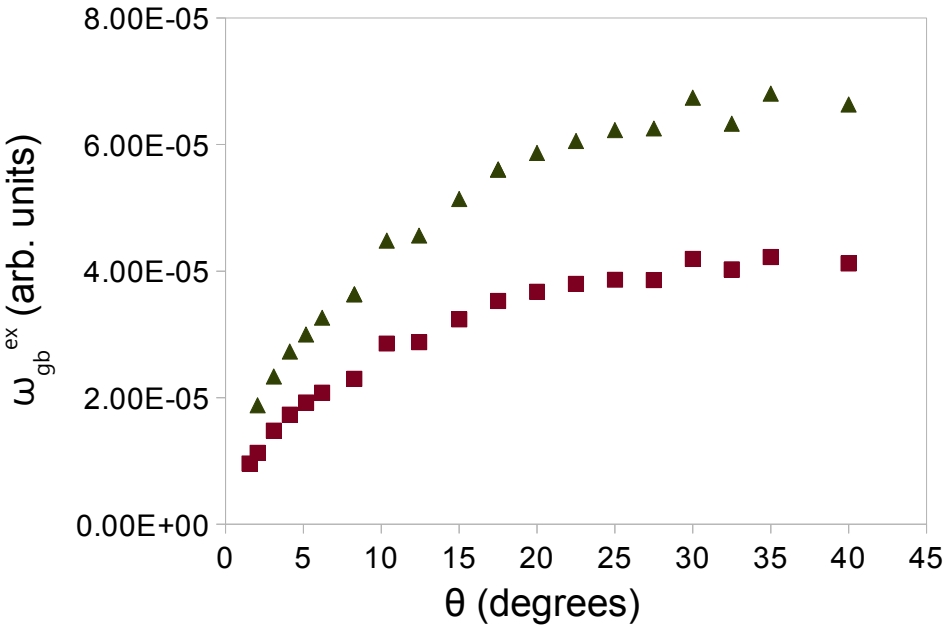

Figure 3.5: PFC model grain boundary energy at different undercoolings. Plotted are $\omega_{gb} = \gamma_{gb}\Delta x/w_{gb}$ vs. misorientation at $B_0^L = 1.015$ for $\psi_0 = 0.1$ (squares) and $\psi_0 = -0.15$ (triangles). From [16].

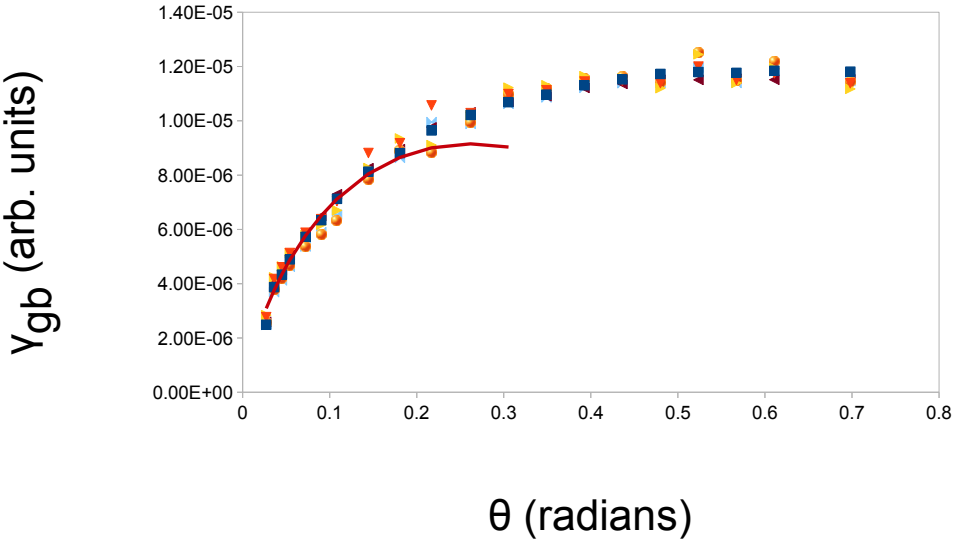

Figure 3.6: Grain boundary energy normalized by the system elastic constants for different degrees of mismatch in the PFC model. Blue squares, maroon triangles - $\eta = 0$; cyan ties, red triangles - $\eta = 0.05$, yellow triangles, orange shaded balls - $\eta = 0.1$. We include a fit to the low angle Read Shockley for comparison. All systems are at the same average alloy concentration. From [16].

boundary energy is a little higher because the grain boundary structure is strained. At larger η, these strains can cause the grain boundary to buckle at some higher angles and at $8.28°$. In fact, going to higher mismatch, the interface is very likely to buckle as shown in Fig. 3.7.

Calculation of Segregation Behaviour

In order to characterize the thermodynamics of solute segregation in grain boundaries, Eqs. 2.25 and 2.26 were simulated. For studying segregation behaviour, a smaller grain boundary length was used ($L_y = 1024\Delta x$). The results of simulations using $L_y = 1024\Delta x$ and $L_y = 2048\Delta x$ were essentially indistinguishable. In these simulations $w = 0.088$, $\eta = 0$, and $B_0^L = 1.002$, $\mu_n = -0.2$ (that is, $n_0 \neq 0$), and misorientation angle $\theta = 40°$. The constant parameters were chosen were those listed in Table 3.1. μ_ψ was the only parameter that was varied.

Both grain boundary energy and excess solute were determined by applying Eq.3.4 as was done by [38], except that only 2 system widths ($N_x = 1024, 2048$) were used as opposed to 5 in [38]. To determine Γ_ψ, the same method was used by referring to Equation. μ_ψ was changed from -0.018 to 0.005 in increments of 0.005. Eq. 1.9, where $y = n$ and $z = \psi$, was computed as follows:

$$\frac{\gamma_{gb}^{i+1} - \gamma_{gb}^{i-1}}{\tilde{\mu}_\psi^{i+1} - \tilde{\mu}_\psi^{i-1}} = -\Gamma_\psi^{ex,i} \tag{3.6}$$

where the index, i, indicates which chemical potential increments are used. Figure 3.8 contains a plot in which $\partial\gamma_{gb}/\partial\bar{\mu_\psi}$ red is determined with Eq. 3.6. In the next section, an analytic form for the total solute segregation in this model is given.

A more conventional way to show the data as was done in [21] is shown in Fig. 3.9, in which solute segregation vs. chemical potential and grain boundary energy vs. chemical potential are

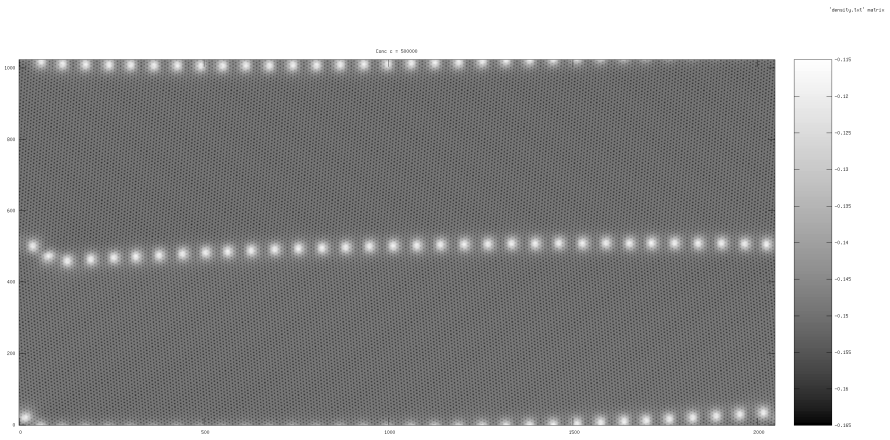

Figure 3.7: Example of concentration field of buckled grain boundary for $\theta = 8.28°$, $\eta = 0.1$, and $B_0^L = 1.015$.

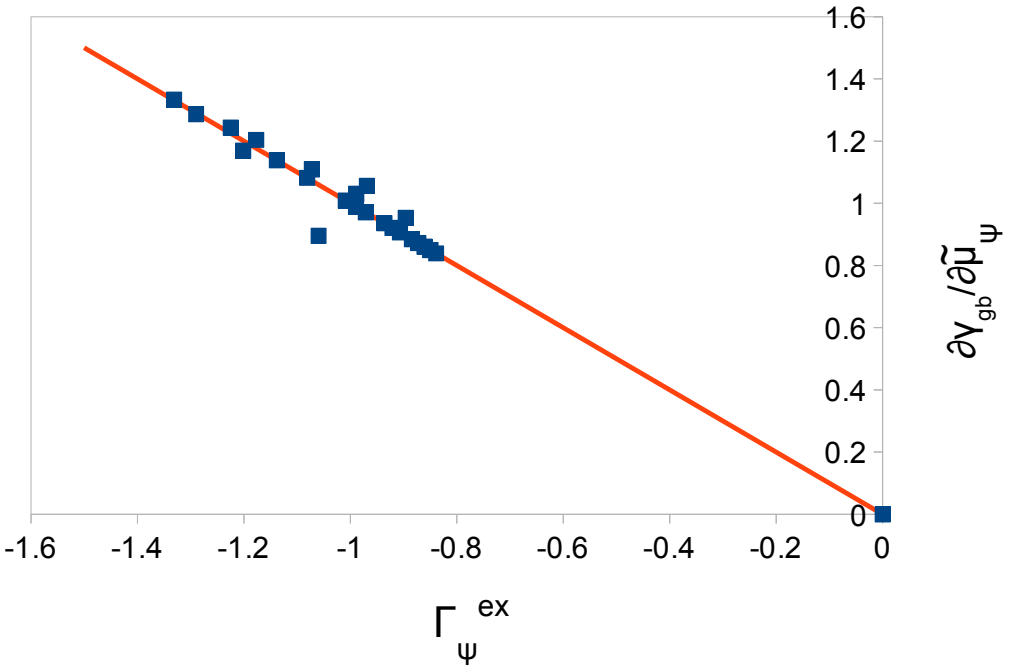

Figure 3.8: $(\partial\gamma_{gb}/\partial\tilde{\mu}_\psi)_{B_0^L,\tilde{\mu}_n}$ vs. negative of grain boundary excess concentration, $-\Gamma_\psi^{ex}$. A reference line with a slope of -1 is included. From [16]

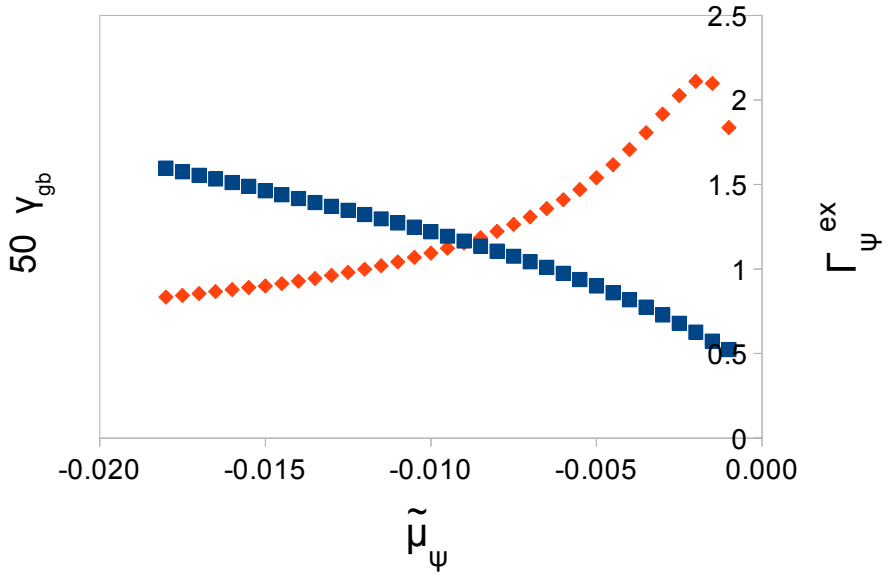

Figure 3.9: PFC model computations of grain boundary energy, γ_{gb}, (blue, squares) and excess grain boundary concentration, Γ^{ex}_{ψ}, (red diamonds) vs chemical potential $\tilde{\mu}_{\psi}$. From [16]

plotted together. Where the change in grain boundary energy is steepest, the amount of excess solute is largest. Nonetheless the large decrease in grain boundary energy is mostly related to the elastic constants in the system changing and not due to the solute segregation, which will be further discussed later in this chapter. The plots indicate that the data is thermodynamically consistent; however, Fig. 3.9 is very different from typical plots of this form for dilute allows, as can be found in [21].

Analytic Derivation of Segregation Behaviour in the PFC Model

An analytic expression for solute segregation to a grain boundary is derived in this section for the PFC model. Using the Gibbs' Adsorption Theorem, Eq. 1.6 and the semi-analytical characterization for γ_{gb} from the previous section allows the derivation of Γ^{ex}_{ψ}. Using the typical variables notations of the PFC alloy model (the reader is referred to sections 2.3 and 3.2), the expression for excess solute in Eq. 1.6 can be rewritten as:

$$\begin{aligned}\left(\frac{\partial \gamma_{gb}}{\partial \mu_{\psi}}\right)_{T,p} &= \left(\frac{\partial \gamma_{gb}}{\partial \mu_{\psi}}\right)_{T,V} - V_{ex}\left(\frac{\partial p}{\partial \mu_{\psi}}\right)_{T,V} \\ &= \left(\frac{\partial \gamma_{gb}}{\partial \psi}\frac{\partial \psi}{\partial \mu_{\psi}}\right)_{T,V} - w_{gb}\frac{n_s - n_{gb}}{1+n_s}\psi \\ &= -\Gamma^{ex}_{\psi} \end{aligned} \tag{3.7}$$

where the thermodynamic temperature variable T is replaced by the reduced temperature variable B^L_0 (B^X is constant) of the PFC model, μ_{ψ} is assumed to be equal to the system average, $\bar{\mu}_{\psi}$, and w_{gb} is the width of grain boundary region. In Eq. 3.7, both derivatives can be written as analytic

expressions with Eqs. 1.10, 2.22, and 3.5, and making use of $\mu_\psi = \partial f/\partial\psi$, where $f(\psi, \phi(\psi), B_0^L)$ is the free energy density derived from the PFC model from the single mode approximation of the density n, Eq. 2.40. Differentiating Eq. 2.40 with respect to ψ results in $\mu_\psi = (w + 6B_2^L\phi^2 - 24\eta B_0^X\phi^2)\psi + u\psi^3$. However, it should be noted that the theoretical quantity $\bar{\mu}_\psi$ differs from the simulated $\bar{\mu}_\psi$, which also implies that there is an uncertainty on any calculated quantities which use this value. Proceding with this definition of μ_ψ,

$$\frac{\partial\psi}{\partial\mu_\psi} = \frac{1}{(w + (6B_2^L\phi - 24\eta B_0^X\phi)(\phi + 2\psi)) + 3u\psi^2 + \partial\phi/\partial\psi} \tag{3.8}$$

and

$$\begin{aligned}\frac{\partial\gamma_{gb}}{\partial\psi} &= \frac{\partial E_0^m}{\partial\phi}\frac{\partial\phi}{\partial\psi}\,\theta\,(A - \ln(\theta)) \\ &= 2\phi\frac{-0.80(B_2^L - 4\eta^2)\psi\theta(A - \ln(\theta))}{\sqrt{t^2 - 15v(B_0^L - B^X + (B_2^L - 4\eta^2)\psi^2)}}\end{aligned} \tag{3.9}$$

Eqs. 3.8 and 3.9 can then be substituted into Eq. 3.7, which gives the expression

$$\begin{aligned}\Gamma_\psi^{ex} &= -w_{gb}\frac{n_s - n_{gb}}{1 + n_s}\psi \\ &- \frac{1.60\,\phi}{(w + 6(B_2^L - 4\eta B_0^X)\phi(\phi + 2\psi\partial\phi/\partial\psi)) + 3u\psi^2} \\ &\times \frac{((B_2^L - 4\eta^2)\psi)\theta(A - \ln(\theta))}{\sqrt{t^2 - 15v(B_0^L - B^X + (B_2^L - 4\eta^2)\psi^2)}}\end{aligned} \tag{3.10}$$

If considering the ensemble in which p is held constant, Cahn's method [22] for determining excess solute is the easiest method for determining the right hand side of Eq. 3.7. Using the PFC variables n and ψ, the application of Cahn's method results an expression for the excess grain boundary concentration:

$$\Gamma_\psi^{ex} = w_{gb}\left(\psi_{gb} - \frac{(1+n)_{gb}}{(1+n)_s}\psi_s\right) \tag{3.11}$$

The expression in Eq. 3.10 can be compared directly with numerical simulations (Eq. 3.11) of grain boundary segregation to verify its validity, which was done in Fig. 3.10. The main discrepancies occur because the theoretical and simulated μ_ψ are not the same; this is partially accounted for by using error bars whose magnitude are determined by the relative difference of the theoretical and simulated μ_ψ. Alternatively, it is easier to consider Γ_ψ^{ex} when $\bar{\mu}_n$ is constant. This results in Eqs. 3.2 and 1.9. However, when studying in the one mode approximation in which n is constant throughout the system, if the temperature is held constant, then the pressure must change, meaning Eqs. 3.10 and 3.11 are equivalent to Eqs. 1.9 and 3.2.

3.2.1 XPFC model

The XPFC model used in this part of the thesis is that formulated in [113]. For studying how grain boundary energy varies with misorientation, Eqs. 2.31 are simulated using the following numerical method because of difficulties reaching equilibrium according to the criteria used ($s_{\mu n} \sim O(10^{-4})$) when using the conventional simulation methods of [113]:

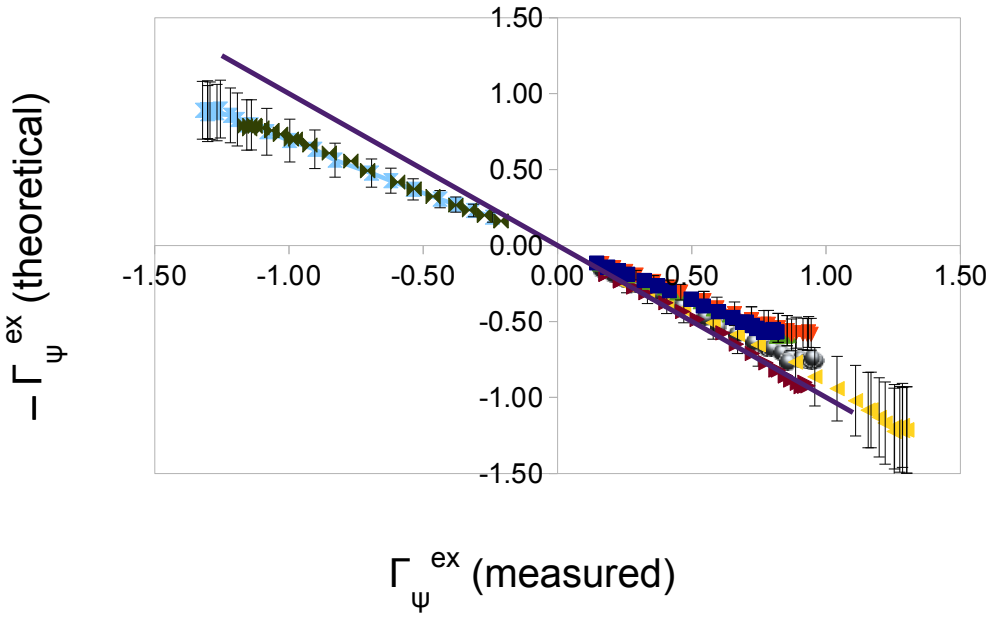

Figure 3.10: Comparing Eq. 3.10 vs. measured Γ_{ψ}^{ex}. Uses empirically determined Read-Shockley parameters. Blue - $B_0^L = 1.015$, $\psi_0 = -0.15$; red - $B_0^L = 1.035$, $\psi_0 = -0.15$; green - $B_0^L = 0.995$, $\psi_0 = -0.15$; maroon - $B_0^L = 1.006$, $\psi_0 = -0.05$; yellow - $B_0^L = 0.996$, $\psi_0 = -0.05$; cyan - $B_0^L = 0.995$, $\psi_0 = 0.1$; dark green - $B_0^L = 1.015$, $\psi_0 = 0.1$; shaded square - $B_0^L = 1.045$, $\psi = -0.2$; shaded diamond - $B_0^L = 1.015$, $\psi = -0.15$,$\eta = 0.05$; shaded ball - $B_0^L = 1.015$, $\psi = -0.15$,$\eta = 0.1$. All data points have $w = 0.088$. Included reference line has a slope of -1. From [5].

$$\hat{n}_k^{t+1} = \frac{1}{1+pk^2\Delta t}(\hat{n}_k^t - \Delta t k^2(\hat{\mu_n}_k^t - p\hat{n}_k^t))$$
$$\hat{c}_k^{t+1} = \frac{1}{1+\alpha k^4\Delta t}(\hat{n}_k^t - \Delta t k^2(\hat{\mu_c}_k^t - k^2\alpha\hat{c}_k^t))$$

where $p = 2$. With this model, simply a 1024x1024 grid is used because the results do not noticeably vary if the either dimension is changed to 2048 grid points. The grid spacing is chosen to be $\Delta x = 0.125$ because this allows for 8 grid points between atomic planes because the interplanar distance does not vary much from that of the pure material, in which the wave number of the solvent phase is $k_1 = 2\pi$. All of the relevant parameters are given in Table 3.3. When performing these simulations a similar criterion to that used for the PFC model. If $s_{\mu n} \approx 10^{-6}$ then the system was considered to be in equilibrium because the concentration field reaches equilibrium much more quickly than the density field.

Table 3.3: Table of Variables and Parameters for XPFC Grain boundary Simulations

Parameters	Values
Simulation Dimensions N_x, N_y	1024 (or 2048), 1024
Equilibriation time N_t	100000 (misorientation runs), 20000 (μ_c change)
Grid Spacing and time increment Δx, Δt	0.125, 1.0 (misorientation), 0.25 or 0.5 (segregation)
mean concentration c_0	0.015 (misorientation runs)
mean density n_0	0 (misorientation runs)
η, χ	1.4, 1
c_0, ω, α, M_c	0.5, 0.02, 1,1
λ	0 or 0.2
k_1, k_2	2π, $9\pi/5$
temperature σ	0, 0.025, 0.05, 0.075, 0.1, 0.125
G_0, D_0, P_0, G_1, D_1, P_1	2/9, 1, -2, 25/32, 1/12, 1
Misorientation angles, θ	$1.55°$, $2.07°$, $2.58°$, $3.10°$, $4.14°$, $5.17°$,$6.20°$, $8.23°$, $10.3°$, $12.5°$, $15°$, $17.5°$, $20°$, $22.5°$, $25°$,$27.5°$, $30°$, $32.5°$, $35°$, $40°$

Calculation of Grain Boundary Energy

The simulations for studying the changing of grain boundary energy with misorientation were done at an average concenration $c = 0.015$ and average density $n = 0$. Unlike the PFC model, the XPFC always has misfit because of how the properties of both phases are interpolated with concentration. $k_2 = 9\pi/5$ was chosen so that the atoms in the solute phase were roughly 10% bigger in linear dimension than the atoms in the solvent phase. The misorientation angles were the same as those used in Section 3.2. The temperature of the system was quenched at $\sigma = 0$ and then the temperature was raised and equilibriated at $\sigma = 0.025, 0.05, 0.075, 0.1, 0.125$. Only results from $\sigma = 0, 0.05, 0.1$ were considered and the grain boundary was always solid at these temperatures.

Eq. 3.4 was used to determine grain boundary energy. Unlike with the PFC model, strain effects were often large and cause deivations. Therefore, the fitting method could not be used. Instead the bulk free energy for a single high energy run ($22.5°$) was determined by using the scaling method of [38], though with 4 data points as opposed to 5, and subtracted off the rest of the runs. Fig. 3.11 shows how grain boundary energy varies with misorientation in the XPFC model at different temperatures. Both high and low angle fits to the $\sigma = 0, 0.1$ data are shown. For the low angle fits,

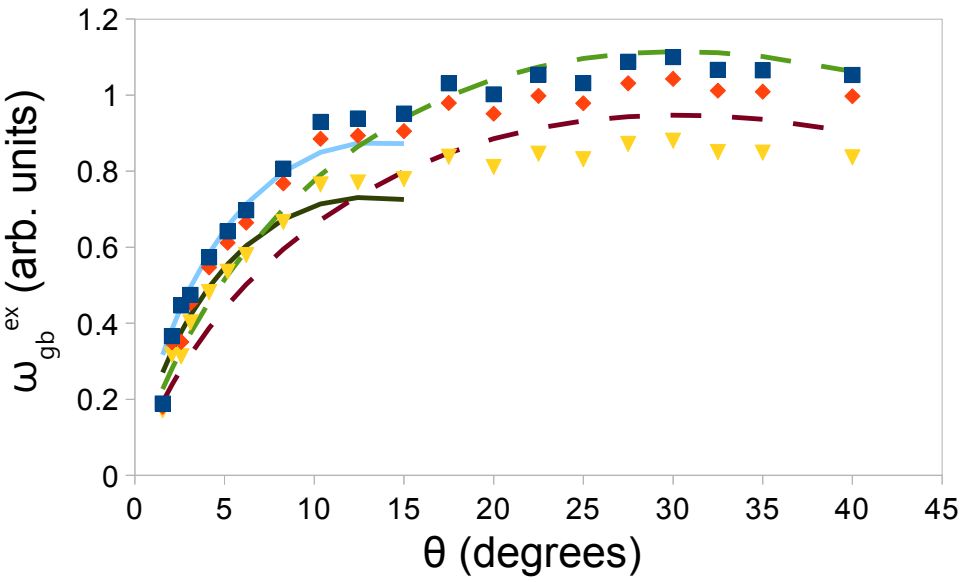

Figure 3.11: Grain boundary energy vs. misorientation in the XPFC model at average system concentration $c = 0.015$ for the parameters in Table 3.3. The datapoints correspond to data taken at temperatures $\sigma = 0.0$ (blue squares), $\sigma = 0.05$ (red diamonds) and $\sigma = 0.1$ (yellow triangles). Low-angle Read-Shockley fit to the $\sigma = 0$ and $\sigma = 0.1$ data are given by the two solid curves. High-angle Read-Shockley fits to the $\sigma = 0$ and $\sigma = 0.1$ data are given by the dashed curves. From [16].

the prefactor E_0/w_{gb} is much smaller than the expected value of $Y_2 b/8\pi\phi^2 w_{gb}$. This observation suggests that solute segregation in the XPFC model decreases grain boundary energy very strongly.

Quantifying Segregation Behaviour

The segregation behaviour of the XPFC model is characterized with the same methods as were used for the PFC model in section 3.2. It should be noted that all equations are the same except that ψ is interchanged with c. Non-conserved dynamics with Eqs. 2.31 are used to find the equilibrium state. Three types of runs were done. For the first two, $\lambda = 0$, $\sigma = 0$, $\tilde{\mu}_n = -0.2$, $M_c = 1.0$ with the chemical potential ranging from $\tilde{\mu}_c = -0.024$ to 0.051. The chemical potential is initially set to $\tilde{\mu}_c = 0$ at which it is equilibriated for 200000 timesteps. Then it is incremented in steps of ± 0.01 and equilibriated for 20000 timesteps at each $\tilde{\mu}_c$. The only difference between the first two types runs is that one is for a low angle grain boundary, $\theta = 4.14°$, and the other is a high angle grain boundary, $\theta = 27.8°$. The third type of run is single run at 27.8° for which $\lambda = 0.2$. Besides the parameters which are the same for all three runs, which are listed in Table 3.3, the others parameters which differ from the first two runs are: $\Delta t = 0.25$, $\tilde{\mu}_n = -0.2$, and $\tilde{\mu}_c$ ranging from -0.0225 to 0.050 in increments of ± 0.0025. The system was initially equillibriated at $\tilde{\mu}_c = 0$ for 400000 timesteps and then held at each subsequent $\tilde{\mu}_c$ for 40000 timesteps.

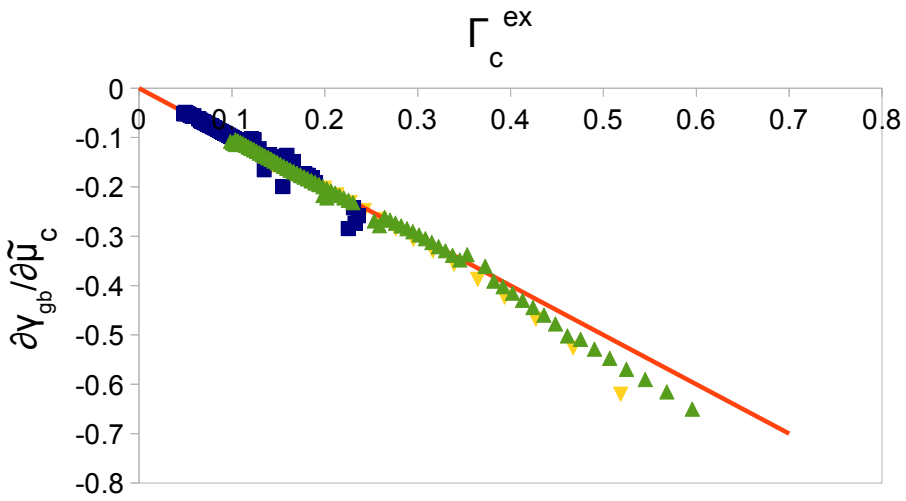

Figure 3.12: XPFC model prediction of Γ_c^{ex} via Eq. 3.12 vs. the same quantity obtained by direct numerical simulation of Γ_c^{ex} (Eq. 3.6 with c replacing ψ) . Green triangles - $\lambda = 0$, misorientation angle $27.8°$, Yellow triangles - $\lambda = 0.2$, misorientation angle $27.8°$, Blue squares - $\lambda = 0$, misorientation angle $4.14°$. The reference line has a slope of -1. From [16].

In the XPFC model, Gibbs adsorption theorem can be written as:

$$\left(\frac{\partial \gamma_{gb}}{\partial \tilde{\mu}_c}\right)_{\sigma,\tilde{\mu}_n} = -\Gamma_c^{ex} \tag{3.12}$$

The data sets obey Eq. 3.12 fairly well as shown in Fig. 3.12. There are some deviations from a slope of -1, which are decreased if a higher order derivative scheme (like a 5 point stencil) is used or by equilibriating longer. Some data was omitted because very large strains, which developed in the system, caused large chemical potential gradients and grain boundary rearrangement, which did not always equilibriate within the alotted time.

As with the PFC model, the change of grain boundary energy and excess concentration with μ_c were shown in Fig. 3.13. There is less segregation when the misorientation is lower, which is explained by there being less imperfect (amorphous/disordered) material in a low angle grain boundary, to which the solute can segregate; that is, there are only dislocation cores (toward which most of the solute is segregating) as opposed to the entire grain boundary being disordered material. Enthalpy of mixing also strongly affects the degree of segregation. Although for both $\lambda = 0$ and $\lambda = 0.2$ data at $27.8°$ the amount of solute segregation is similar, the segregation per amount of solute is much stronger for the $\lambda = 0.2$ data because there is much less solute in the $\lambda = 0.2$ runs than in the $\lambda = 0$ runs for a given $\tilde{\mu}_c$ (the difference is roughly a factor of 3). As expected by how the segregation varies in the system, the grain obundary energy varies similarly between both systems.

The XPFC model was chosen because of its ability to model realistic phase diagrams of metals, including the low concentrations limits. Fig. 3.13 resembles the same plot for P segregation in Fe in [21], which was a study of segregation behaviour at low concentration. Unlike the data in [21],

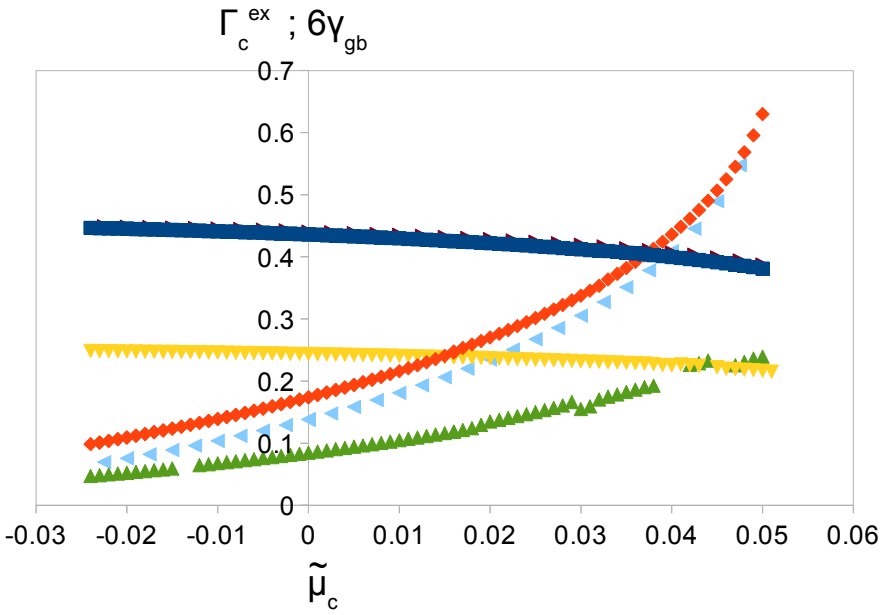

Figure 3.13: XPFC simulation results of Γ_{ψ}^{ex} and γ_{gb} vs. $\tilde{\mu}_c$. γ_{gb}: $\lambda = 0$, misorientation angle $27.8°$ (blue squares); $\lambda = 0$, misorientation angle $4.14°$ (yellow upside-down triangles); $\lambda = 0.2$, misorientation angle $27.8°$ (maroon right-pointing triangles). Γ_{ψ}^{ex}: $\lambda = 0$, misorientation angle $27.8°$ (red diamonds); $\lambda = 0$, misorientation angle $4.14°$ (green upward pointing triangles); $\lambda = 0.2$, misorientation angle $27.8°$ (cyan left-pointing triangles). From [16].

data was obtained in the XPFC model when the material crossed the solvus line and the solid phase became metastable. In this regime, the amount of excess solute does not saturate as suggested by [21], but rather continues to increase. Any discontinuities in the $4.14°$ curve in Fig. 3.13 correspond to instances in which the system had not quite equilibriated and these points were omitted from Fig. 3.12.

3.3 Discussion of Solutal Effects of Grain boundaries

3.3.1 Relation of Grain Boundary Segregation to Physical Properties

By considering the analytical expressions derived in Eq. 3.10, the degree of solute segregation in the system can be related to the physical properties of the system, including temperature (undercooling), chemical potential (concentration), mismatch, and energy of mixing. Plots of Eq. 3.10 for various simulation parameters are contained in Fig. 3.14. The analytic curves for $w = 0.088$ are very similar to the plot in Fig. 3.8.

(Normalized) temperature (ΔB_0) strongly affects the degree of segregation, which is illustrated by the change observed between the red and green curves. ΔB_0 has a noticeable impact on the density amplitude, ϕ, and $\partial\mu_\psi/\partial\psi$ which causes this large change in segregation. We note that this strong dependence of solute segregation on temperature is also expected for the XPFC model because of the large change in γ_{gb} observed in Fig. 3.11. Far away from a phase boundary in both the PFC eutectic and XPFC models, the degree of segregation is small. Near the phase boundary, however, the degree of undercooling has a strong effect, as is shown in Figs. 3.13 and 3.14.

In Figure 3.14, the effect of mismatch is small, if the mismatch between the solute and solvent

species ($|\eta|$) is small; the blue ($\eta = 0.1$) and red ($\eta = 0$) curves, which are at the same temperature, do not differ much. But if the mismatch becomes larger, as in the case of the purple ($\eta = 0.2$), then there is a significantly larger degree of segregation for the range of μ_ψ around the peaks of the curve. This change can be expected on physical grounds because strains in the system due to local lattice mismatch can be significantly reduced if a lot of solute moves to the grain boundary, where the atoms of a different size can be accomodated more easily due to the disordered structure. The small effect at low $|\eta|$ occurs because ϕ^2 and $\partial\mu_\psi/\partial\psi$ are not changed by a significant amount (these quantities depend on η^2). In the XPFC model, on the other hand, the misfit is responsible for showing the usual segregation behaviour. At no lattice mismatch in the XPFC model, the segregation behaviour has the opposite sign; that is, solute moves away from the grain boundary, which is rare, but still seen in some materials [22].

In the PFC model, eutectic systems ($w = 0.008$) displayed stronger segregation than those with a double lens-shaped ($w = 0.088$) phase diagram at the same concentration, ψ_s. This is related to the energy of mixing between the two species (A and B), ϵ_{AB}, relative to the the self bond energies $\epsilon_{AA}, \epsilon_{BB}$, which is realted to the parameter $w \sim (2\epsilon_{AB} - \epsilon_{AA} - \epsilon_{BB})$. As w decreases, both species exhibit larger self-attraction, meaning that a larger degree of segregation is thermodynamically more favourable in the eutectic material than in the double lens phase diagram material. In fact, this trend is observed when comparing a number of materials according to solute enrichment factor and solute solubility, which is roughly related to $2\epsilon_{AB} - \epsilon_{AA} - \epsilon_{BB}$ [21, 22]. The XPFC model also exhibits this behaviour, which can be seen by comparing the $\lambda = 0$ and $\lambda = 0.2$ datasets at misorientation $\theta = 27.8°$. For the $\lambda = 0.2$, the solute solibility is lower and the solute enrichment factor is higher than in the $\lambda = 0$ case because the degree of solute segregation is the same despite the much lower concentration in the $\lambda = 0.2$ case.

Several of the curves in Fig. 3.14 have 2 extrema (a maximum and minimum) in grain boundary excess concentration. One extremum is expected if there is a non-zero excess in a pure material if the solid solubility is continuous, unlike in eutectics, or other materials with a solubility gap, in which there need not be an extremum. In fact, for a material in which both species are completely soluble in each other, there should be 2 extrema, if solute favours occupying the grain boundary as opposed to the matrix. In the PFC model with the double lens-shaped phase diagram, this is the case; the material is A-rich for $\psi < 0$ and B-rich for $\psi > 0$ and a quasi-pure material at $\psi = 0$. In more complex materials, if the free energy functional is known, then Eq. 1.9 can be used to predict the behaviour of the segregation curves and where peaks of segregation behaviour occur. Also, the segregation peaks in Fig. 3.14 shift with temperature. The segregation peaks shift towards $\psi_0 = 0$ at lower temperatures because the grain boundary can be considered as consisting of amorphous regions, whose metastability increases with decreasing temperature.

On the other hand, materials with a solubility gap can have discontinuities in the Γ^{ex}_ψ vs. μ_ψ (or equivalently ψ) relation. This is clearly seen in the eutectic material in the PFC model, in which this relation is monotonic, except for the discontinuity. Equivalently, in the work of [21], only a montonic change in the degree of solute segregation of P in Fe-P is observed with change in chemical potential; chemical potential is found using Henry's Law from the concentration. The binary XPFC model also shows the trend of Γ^{ex}_c monotonically changing with c and it approximately obeys Henry's Law.

3.3.2 Impact of Physical Properties of Material on Grain boundary Energy

When considering the effect of solute segregation on grain boundary energy, there are two main factors to consider: the difference between the grain boundary energy of an alloy and a pure material with equivalent properties and the change in grain boundary energy with a change in thermodynamic control parameters (e.g., temperature, chemical potential, pressure). In the PFC model with $w = 0.088$, an alloy and pure material with equal elastic moduli do not have substantially different grain boundary energy. At low angles, this phenomenon might be related to Turnbull's estimation of an interface energy between two systems of low lattice mismatch; that is, a heterointerface containing a

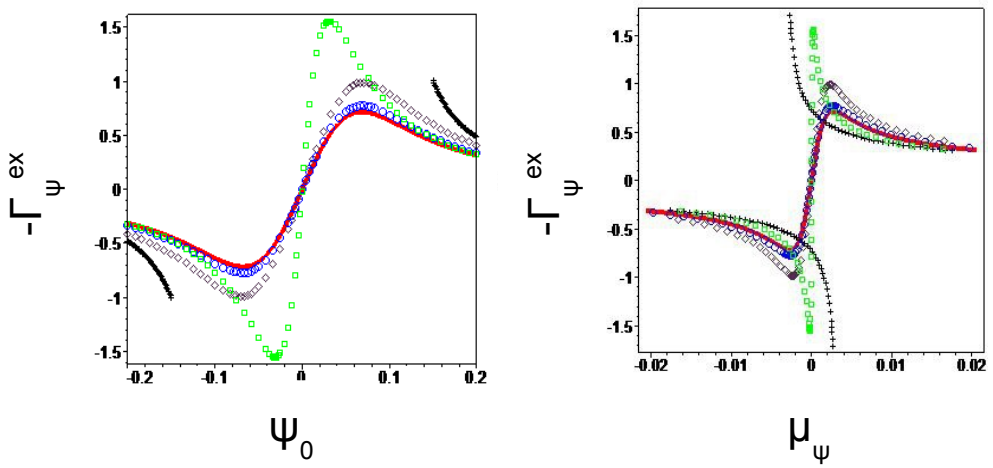

Figure 3.14: Solute segregation at misorientation of 22.5° at different ψ_0 *(left)* and μ_ψ *(right)* using Eq. 3.10. Red line- $B_0^L = 0.01$; Blue circle- $\eta = 0.1$, $B_0^L = 0.01$; Purple diamonds- $\eta = 0.2$, $B_0^L = 0.01$; Green square- $B_0^L = -0.01$; Black crosses- $B_0^L = 0.01$. $w = 0.088$ for all plots except the black crosses, which have $w = 0.008$. Adapted from [16] and [16].

number of dislocations [139]. The energy in such a system is considered to be dominated by elastic, but not chemical effects. Even with possibly changing core size, as indicated in Fig. 3.3, the grain boundary energy is very close to that of a pure material (to which $\psi_0 = 0$ is equivalent) because the cores only account for a small portion of the free energy.

As mentioned, high angle grain boundaries in the PFC model with $w = 0.088$ also show little change in grain boundary energy between an alloy and a pure material. For a given material, the decrease in γ_{gb} in a given grain boundary should be proportional to the amount of solute, which segregated to the grain boundary. Based on Eq. 3.10, the decrease should be proportional γ_{gb} for a given material, so the observation of a negligible relative decrease in grain boundary energy should be unsurprising, despite the fact that the grain boundary energy is no longer dominated by elastic effects as at low angles, but rather by the presence of an undercooled (disordered) metastable phase [140]. Nonetheless, it should be remarked that although the grain boundary energy does not differ significantly from that of a pure material with equal elastic properties, the grain boundary energy can change substantially with a change in thermodynamic control parameters.

The eutectic PFC model, on the other hand, exhibits some difference in grain boundary energy from an elastically-equivalent pure material. The increase in energy of mixing in solute segregation means that the increased amount of solute in the grain boundary also has a larger effect on γ_{gb}, causing it to decrease more. The XPFC model studied is also that of a eutectic material, in which the atoms are even less soluble in each other—which suggests a greater energy of mixing. In fact, the grain boundary energy decrease is so large in the XPFC model that the Read Shockley coefficents are noticeably smaller than the theoretical values ($\sim 80\%$ of the theoretical E_0). However, the grain boundary energy does not change much as μ_c changes at constant σ. This trend suggests that any decrease in γ_{gb} is dominated by the degree of solute segregation.

In fact, despite any solutal effects on the grain boundary energy, γ_{gb} should maintain its Read-Shockley form. The amount of solute segregation, Γ_z^{ex}, has a Read-Shockley form according to Eq. 1.9. The free energy decrease is proportional to Γ_z^{ex}, meaning that any contributions to the free energy also have a Read-Shockley form. Because of these considerations, even in the eutectic PFC model or the XPFC model, where solutal effects noticeably change the free energy, the

Read-Shockley form should be a good form to study grain boundary energy because it has been demonstrated to be useful in many other studies of pure materials.

The PFC formalism results can be compared with experiments and molecular dynamics stuides. These also demonstrate that solute segregation can have a large effect on grain boundary energy when the species are immiscible (e.g., [22, 24]) and small when they are miscible (e.g., Cu-Au in [21]). Though significant effects can be seen when the composition changes drastically in miscible systems as shown in [25]. However, such studies are not necessarily able to probe the mechanism responsible for the decrease in grain boundary energy. Modelling, in particular PFC modeling, on the other hand, can be used to isolate what particular physical mechanism is responsible for a decrease in grain boundary energy by calculating the individual properties, such as elastic constants. One particular instance of isolating the mechanism for grain boundary energy decrease is in studying the PFC model with $w = 0.088$, in which it can be determined that the changing elastic constants is related to the dominant effect for the changing grain boundary energy because the grain boundary energy does not differ in systems with different amounts of solute, but the same elastic constants. This effect is particularly strong, as shown in Fig. 3.9, but it is not directly related to solute segregation as the previous consideration shows.

It should be noted that there are some differences when comparing 2D grain boundary energy studies against 3D grain boundary energy studies. For some of the tilt axes in 3D, the grain boundary versus misorientation data has deep cusps in the relation [22, 25, 141], while for 2D studies, the grain boundary energy is relatively smooth with at most shallow cusps [1, 38, 16] . However, as shown in [141], not all of the tilt axes have deep troughs, so qualitatively the picture given by the grain boundary relation for misorientation looks pretty much the same. It may be possible to simulate special high angle boundaries with low energy by changing the initial conditions or by using different crystal symmetries in 2D, thereby allowing some 2D simulations to capture particular features of 3D simulations. It should also be noted that even when the physics between 2D and 3D is qualitatively the same, the quantitative results are nonetheless different as many of the thermodynamic quantities and their relative ratios shift between 2D and 3D [134]. Changes in grain boundary segregation behaviour are to be expected as well because the segregation behaviour is tied to the grain boundary energetics.

3.3.3 Miscellaneous considerations

With demonstrating that PFC-type alloy models can capture the fundamental physics of alloy grain boundary behaviour, it remains to develop more quantitative models of this process. There are a number of new improvements in PFC models. One of the most important is by tuning the correlation function properly (e.g., [112, 108, 109, 40, 118]) and with this improvement, segregation preoprties should be simulated more accurately. In fact, Berry et al [112] demonstrate how certain defect properties can be tuned, thus resulting in more realistic simulations of these defect properties.

Nonetheless, advances can still be made by considering generic properties of materials with non-tuned models. The considerations about grain boundary energy and solute segregation in alloys are important for studying the problem of premelting; the energetics are clearly important as noted by by [29], [38], and [46] and consideration of solutal effects is noted by [3]. Not only can solutal effects alter the effects seen in a pure material, but they might also cause entirely new phenomena to emerge. Gibbs adsorption theorem could provide a useful tool for studying these effects in even premelted interfaces [22]. Some preliminary work on this topic is shown in the next section.

3.4 Grain boundary premelting

As noted in section 1.2.2, an important consideration in studying grain boundary premelting behaviour is the determination of the disjoining potential for a given grain boundary. This section

shows new results on the disjoining potential for the PFC model.

To estimate the disjoining potential, Eqs. 1.11 and 1.12 were used. The solid system properties were estimated from the scaling method of [38], except with only $L_x = 1024\Delta x$ and $2048\Delta x$. The liquid properties are determined in a separate simulation. The constant simulation parameters used are listed in Table 3.4. The reader is referred to Section 1.2.2 for the details of the disjoining potential theory examined in this section via PFC simulations.

Table 3.4: Table of Variables and Parameters for Grain Boundary Premelting PFC Simulation

Parameters	Values
Simulation Dimensions N_x, N_y	1024 or 2048, 1024 (solid) or 64, 64 (liquid)
Grid Spacing and time increment Δx, Δt	$\pi/4$, 1.0
t, v, B^x	0.6, 1, 1
B_2^L, u, K_c	-1.8, 4, 4
w	0.088 (spinodal)
mismatch η	0
B_0^L	1.05
μ_n	-0.025
Misorientation angle θ	40°

Disjoining potential was determined using a modification of the method of [38] used. As noted, in [38], the derivative of the disjoining potential is the disjoining pressure, which is equal to the difference in grand potential of liquid and solid states:

$$\frac{dV(h)}{dh} = \omega_s - \omega_l \tag{3.13}$$

As mentioned in section 1.2.2, there are many definitions for width of the grain boundary. In this section, two definitions are used— the definition in Eq. 1.14 and the analogue for ψ, which is:

$$h_\psi = L_x \frac{\Gamma_\psi^{ex}/L_y}{\psi_l - \psi_s} \tag{3.14}$$

Figure 3.15 contains a plot showing how width varies against temperature for both defintiions. Although the estimation of width is quite different between the two methods, they are both monotonic with chemical potential, meaning that the preference of one over the other is somewhat arbitrary in that both are equally good thermodynamic variables, though one might make calculations easier. They are more similar closer to the melting point, which would be expected because there would be a larger region which is more similar to the liquid.

Figure 3.16 contains a plot for disjoining pressure vs. width for both methods of calculating width. Using either definition of width, the disjoining pressure curves can be well-fit by exponential functions, as expected for 40° misorientation, a large angle grain boundary. These fits can then be used to determine the disjoining potential by integrating the pressures with respect to width, as illustrated in Fig. 3.17.

This preliminary set of runs was further refined by [17] in which the grain boundary premelting behaviour was characterized. The parameters for the simulations are given in [17]. One important consideration neglected in this section of the thesis, which was accounted for in [17], was that of elastic effects, which slightly increase the energy of the solid phase, and thus slightly alters the melting point of the material. This problem was avoided by choosing angles in [38], in which the crystal fits well in the $y-$direction (whose length is a mulitple of 256π). Figure 3.18 shows the width versus chemical potential for 5 different angles, each representing a different kind of grain boundary (5° and 13.2° are low angle grain boundaries, while 17.8°, 21.8°, and 27.8° are high angle grain bound-

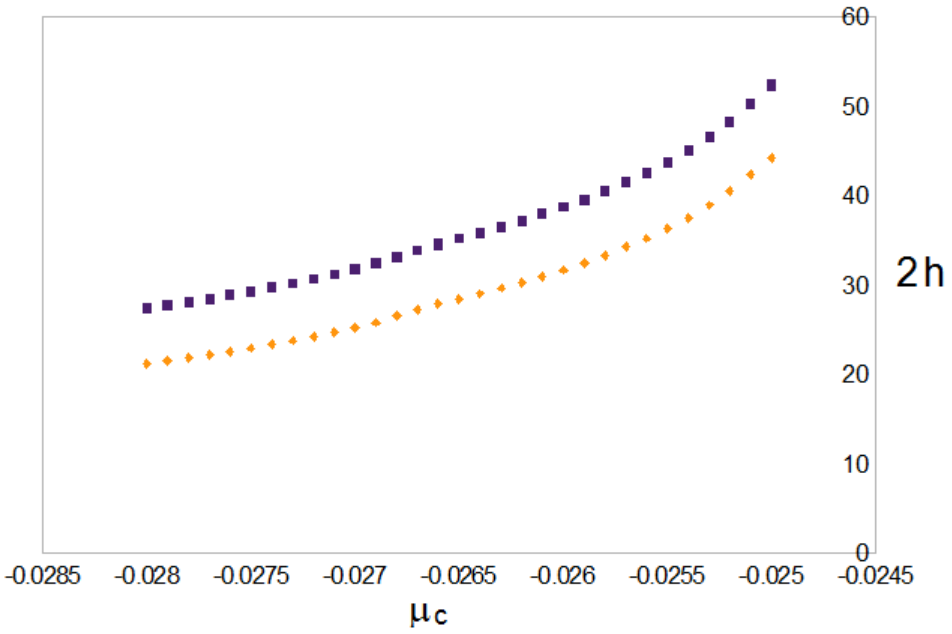

Figure 3.15: Grain boundary width, h, as determined by excess concentration (purple squares) and by excess density (yellow diamonds) vs. chemical potential, μ_c.

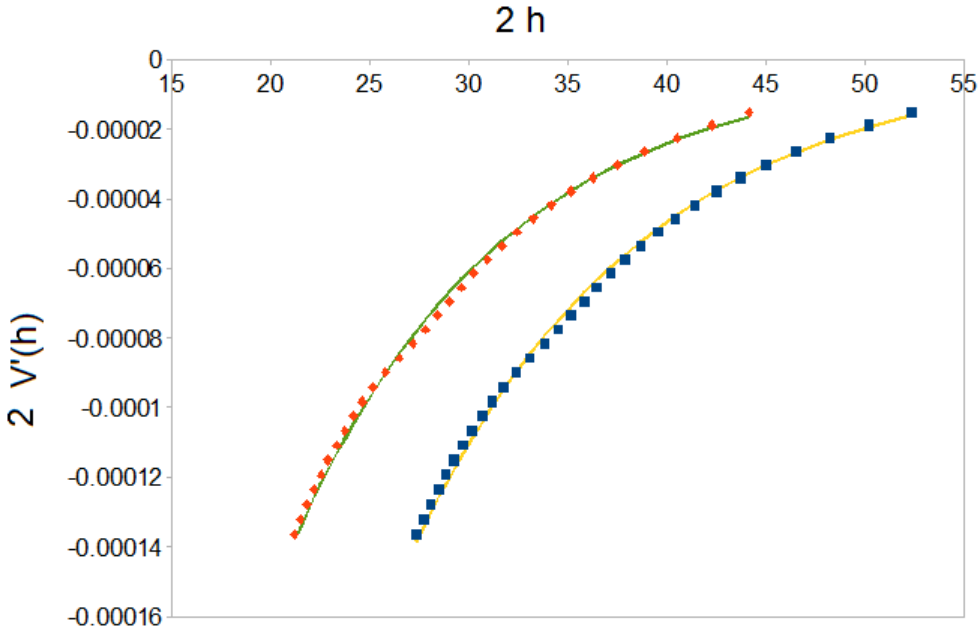

Figure 3.16: Disjoining pressure vs. width as determined by excess concentration (blue squares) or excess density (red diamonds). Included are exponential fits of the form $C_1 \exp(\lambda_1 h)$: yellow curve, $\lambda = -0.08575$, $C_1 = -0.001446$; green curve, $\lambda = -0.09270$, $C_1 = -0.0009844$

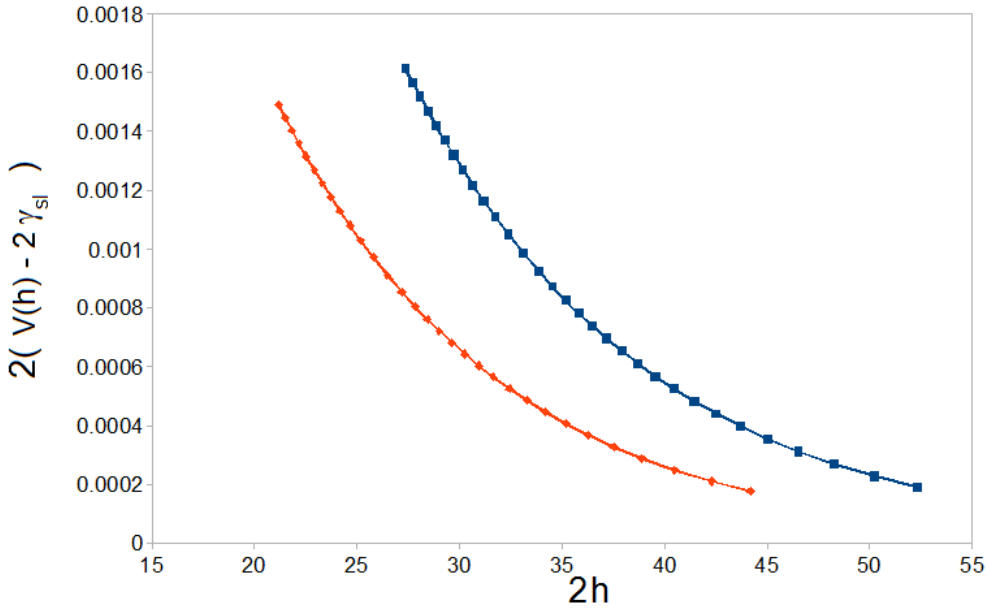

Figure 3.17: Disjoining potential vs. width as determined by excess concentration (blue squares) or excess density (red diamonds).

aries). As expected from the changing grain boundary energies, different premelting behaviours were obtained; the small angle, low energy grain boundaries could be overheated because the attractive grain boundary keeps the grain boundary from opening and acting as a site of nucleation for a liquid to form, while the large angle, high energy grain boundaries had a logarithmic divergence at the melting point. 17.8° was an intermediate energy grain boundary, which could not be overheated, yet its width did not diverge at the melting point. As seen in Fig. 3.19. In [17], larger widths were obtained than in the results of Fig. 3.15. The definition of width that was chosen was Eq. 1.14.

In Figure 3.20, the disjoining pressure versus width curves are shown for each grain boundary. To capture the attractive behaviour, the double exponential fit of [48] was used [17] . These curves can then be integrated analytically to give the disjoining pressure, as shown in Fig. 3.21. As expected, the angles with repulsive disjoining potential curves correspond to those that could not be overheated in Fig. 3.18, while those with finite width at the melting point have a long range attractive disjoining potential. The short range disjoining potential is repulsive for all of the angles studied in [17].

3.4.1 Miscellaneous Considerations

An analytic model of premelting was by considering by using Eq. 2.40 and by substituting an average strain field, $< \epsilon^2 >$, corresponding to the effect of the grain boundary. Although it would be more accurate to change the strain with temperature, insights into the effects of solute on premelting behaviour can be obtained simply by analyzing a form with a constant strain field. An effective phase field free energy, derived from a PFC model [119], which includes solute, order parameter and mean field strain effects can be directly written down as follows:

$$F = \int d\vec{r} \left(3\Delta B_0 \phi^2 + 3B_2^L c^2 \phi^2 + 4t\phi^3 + \frac{45v}{2}\phi^4 + 6B_0^X (\nabla\phi)^2 \right)$$

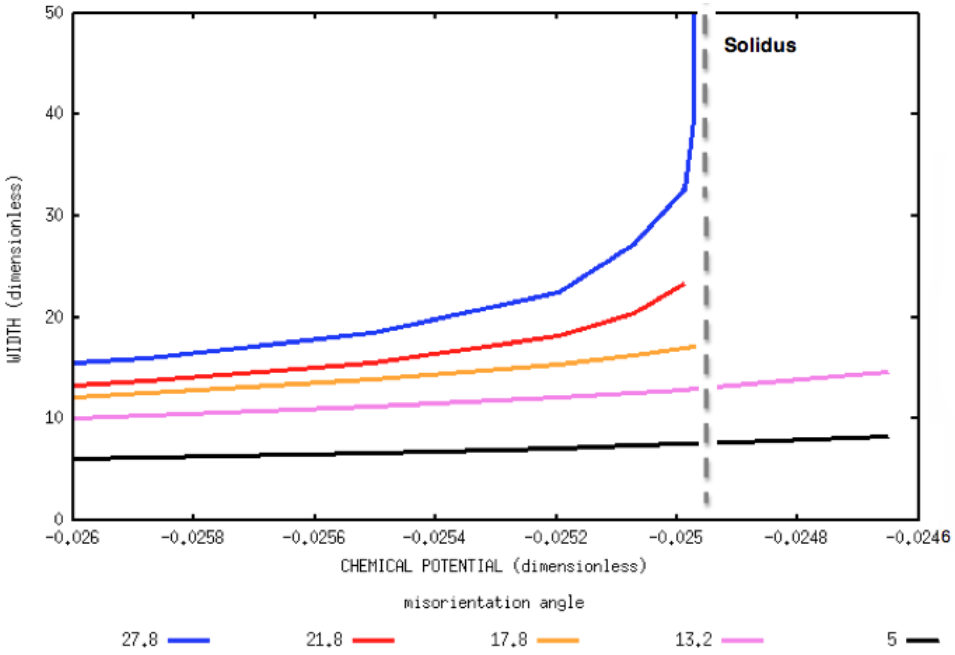

Figure 3.18: Disjoining potential vs. width as determined by excess density for angles 5° (black), 13.2° (magenta), 17.8° (yellow), 21.8° (red), and 27.8° (blue). The dashed grey line is the melting point. From [17].

$$+\left(\frac{wc^2}{2}+\frac{uc^4}{4}+\frac{K(\nabla c)^2}{2}+18B_0^X<\epsilon^2>\phi^2\right) \tag{3.15}$$

This model can be used to study two problems: the asymptotic behaviour of grain boundary premelting and hysteresis of grain boundary widths.

Asymptotic Behaviour of Disjoining Potentials

One problem that can be approached analytically is what kind of disjoining potentials Eq. 3.15 describes and to what extent concentration affects the disjoining potential. To start this study, the approach of [3] is used. Also, to simplify the algebra, in a liquid layer of width, W, the grain boundary is considered infinitely sharp; that is, $<\epsilon^2>=\epsilon\delta(x)$. For the system in equilibrium, the grand potential, $\omega = f - \mu c$, must be conserved everywhere, where $\mu = \partial f/\partial c$ for a constant phase (like liquid or solid). In analogy with Hamiltonian mechanics, the Hamiltonian is defined as:

$$H = K|\nabla c|^2 + B_0^X|\nabla\phi|^2 - \omega \tag{3.16}$$

If there is solid present in the material, then the Hamiltonian is everywhere equal to:

$$H = -\omega_s = \mu_s c_s - f_s \tag{3.17}$$

Near the centre of the liquid layer for a premelted grain boundary, the variables deviate slighlty from the liquid values ($c = c_l + \delta\psi$ and $\phi = \delta\phi$). If there is a very large liquid layer, then to 3^{rd} order the perturbed Hamiltonian becomes

$$H \quad = \quad -\omega_s = -\omega = -\omega_l + K|\nabla\delta c|^2 + 6B_0^X|\nabla\delta\phi|^2 + \mu_l(c_l+\delta\psi) \tag{3.18}$$

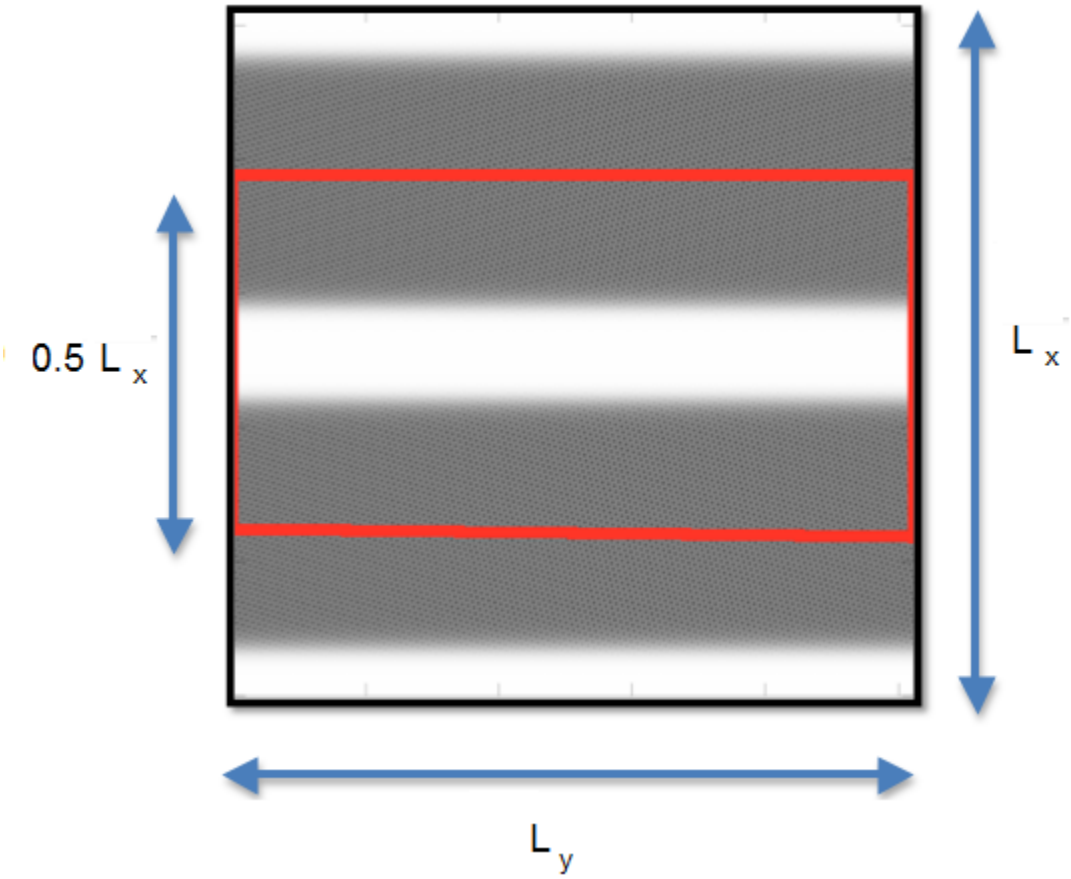

Figure 3.19: Image of a premelted grain boundary. Because there are two boundaries, it is similar to studying 2 bicrystal systems with regions of width $L_x/2$. From [17].

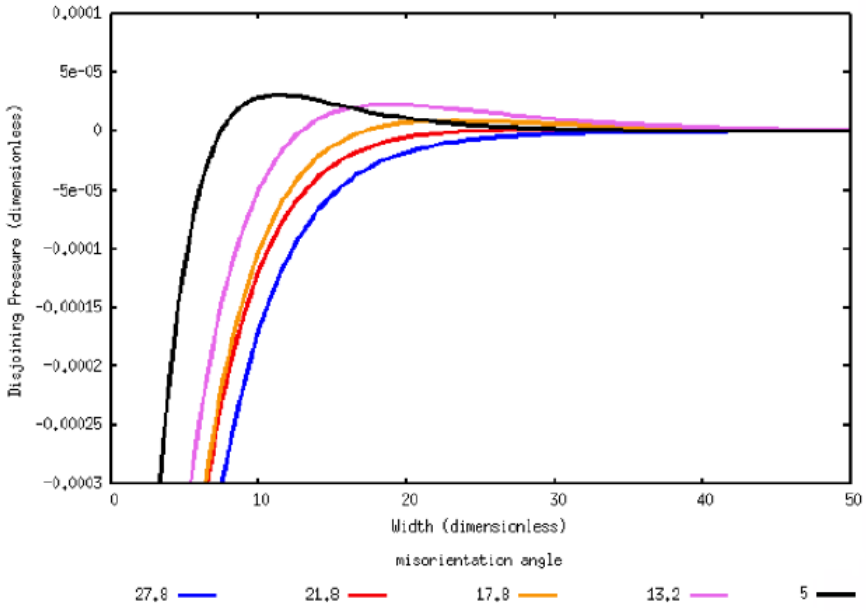

Figure 3.20: Disjoining pressure vs. width for 5° (black), 13.2° (magenta), 17.8° (yellow), 21.8° (red), and 27.8° (blue). From [17].

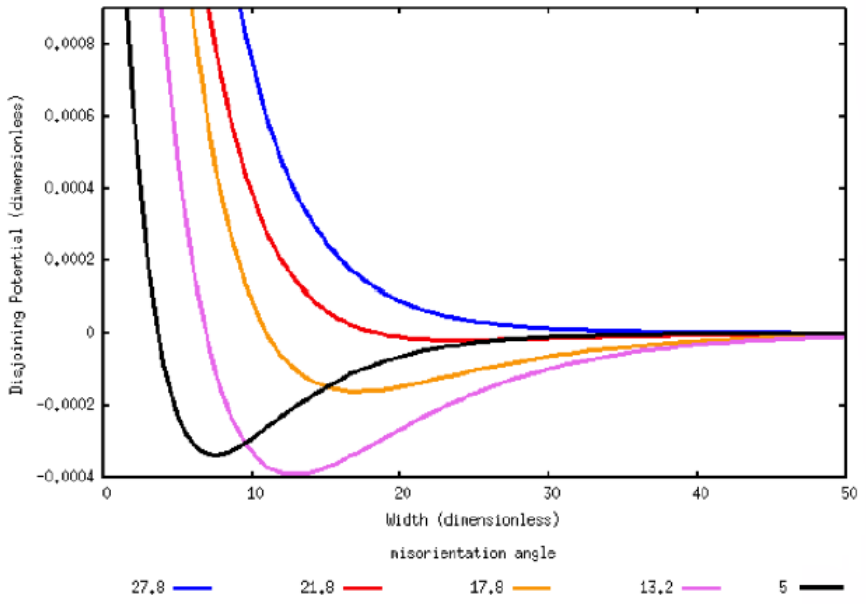

Figure 3.21: Disjoining potential vs. width for 5° (black), 13.2° (magenta), 17.8° (yellow), 21.8° (red), and 27.8° (blue). From [17].

$$- \quad \left(3\Delta B_0 \delta\phi^2 - 4t\delta\phi^3 + 3B^L c_l^2 \delta\phi^2\right) - \left(6B^L c_l \delta c \delta\phi^2 + \frac{w}{2}\delta c^2 + \frac{3}{2}uc_l^2\delta c^2 + uc_l\delta c^3\right)$$

where, according to [3], the effective action, S, can be written for an alloy as

$$S = \int_{-\infty}^{\infty} \omega - \omega_s dx$$

Normally, the third order terms can be neglected because they are much smaller than the second order terms, so the initial analysis can be performing with the 2nd order terms only. Taking the functional derivatives of 3.19, dropping the 3rd order terms, setting the result to zero, and rearranging the equation results in two uncoupled differential equations:

$$\begin{aligned} K\frac{d^2\delta c}{dx^2} &= (w + 3uc_l^2)\delta c \\ 12B_0^X \frac{d^2\delta\phi}{dx^2} &= 6(\Delta B_0 + B_2^L c_l^2)\delta\phi \end{aligned} \tag{3.19}$$

with the following boundary conditions:

$$\begin{aligned} \delta c(W) &= \delta c(-W) = C \\ \delta\phi(W) &= \delta\phi(-W) = \Phi \\ \frac{d\delta\phi}{dx}_{0+} - \frac{d\delta\phi}{dx}_{0-} &= 18B_0^X\epsilon \end{aligned} \tag{3.20}$$

where Φ and C are constants.

Because both the fluctuation in amplitude and concentration fields are decoupled in the liquid, this means that they both have the form $C_{1i}\exp(\lambda_{1i}x) + C_{2i}\exp(\lambda_{2i}x)$, where i is ϕ or c and $\lambda_{1i} = -\lambda_{2i}$. Substituting this form in Eq. 3.19 with the third order terms dropped results in:

$$-(\omega_s - \omega_l) = -(w + 3uc_l^2)C_{1c}C_{2c} - 6(\Delta B_0 + B_2^L c_l^2)C_{1\phi}C_{2\phi} \tag{3.21}$$

Making use of Eqs. 3.20 results in:

$$\begin{aligned} -(\omega_s - \omega_l) &= -(w + 3uc_l^2)C_{1c}^2 - 6(\Delta B_0 + B_2^L c_l^2)C_{1\phi}(C_{1\phi} - 18B_0^X/|\lambda_{1\phi}|\epsilon) \\ -(\omega_s - \omega_l) &\approx -(w + 3uc_l^2)C_{1c}^2 + \frac{108(\Delta B_0 + B_2^L c_l^2)B_0^X\epsilon}{|\lambda_{1\phi}|}C_{1\phi} \\ -(\omega_s - \omega_l) &\approx -(w + 3uc_l^2)C^2\exp(-2|\lambda_{1c}|W) \\ &+ \frac{108(\Delta B_0 + B_2^L c_l^2)B_0^X\epsilon}{|\lambda_{1\phi}|}\Phi\exp(-|\lambda_{1\phi}|W) \end{aligned} \tag{3.22}$$

From Eq. 3.22, it can be deduced that the asymptotic disjoining potential is determined by either the c terms or the ϕ term. In the case that the ϕ term survives $|\lambda_{1\phi}| < 2|\lambda_{1c}|$:

$$W \sim \ln\left(\frac{-(\omega_s - \omega_l)}{D_1}\right) \tag{3.23}$$

where $D_1 = 108\Phi(\Delta B_0 + B_2^L c_l^2)B_0^X\epsilon)/|\lambda_{1\phi}| > 0$, which means that solutions only exist when $-(\omega_s - \omega_l) > 0$ or when the system premelts. The grain boundary is therefore asymptotically repulsive.

Conversely, when the c term survives, $|\lambda_{1\phi}| > 2|\lambda_{1c}|$, and

$$W \sim \ln\left(\frac{-(\omega_s - \omega_l)}{D_2}\right) \tag{3.24}$$

where $D_2 = -C^2(w + 3uc_l^2) < 0$, which means that solutions only exist when $-(\omega_s - \omega_l) < 0$ or when the system is overheated. The disjoining potential is therefore asymptotically attractive. Depending on the parameters that are chosen, an attractive or repulsive grain boundary can be made with this model. This means that materials with a eutectic phase diagram (lower w) are more likely to have attractive grain boundaries than those with a spinodal phase diagram (higher w). Because $(\Delta B_0 + B_2^L c_l^2) B_0^X \epsilon)$ is nearly constant, while D_2 changes strongly with c, attractive grain boundaries would be expected for c

In the rare case that $C_{2\phi} = 0$, but $3|\lambda_\phi| < 2|\lambda_c|$, the analysis of [3] would need to be extended, as was done in [54] by considering higher order terms because the second order terms cancel. The third order terms are however still slaved to the results of the second order terms, meaning that $-(\omega_s - \omega_l)$ needs to be compared with $4t\delta\phi^3$. In fact, this term has the opposite sign of $4t\delta\phi^3$. The above consideration is not a concern for the δc field because it is a $\cosh$ function due to Eqs 3.19 and 3.20. Although this analysis can be used to determine more complicated long range disjoining potentials depending on how terms of all orders interact, possibly allowing some insight into a hysteresis mechanism, hysteresis will be approached with a more brute force method in the next section.

Hysteresis

In the above mentioned studies, no hysteresis behaviour was observed, although such a mechanism was observed in the pure model study of [38]. This should also be observable in the PFC binary alloy model, the presence of a second atomic species could open up other possibilities for a hysteresis. One way that this can happen can be understood by considering how different phases can be in equilibrium with each other; in particular, one might look for dual width hysteresis in premelting in material with multiple stable liquid states [142].

From [3], it should be noted that dual width behaviour is seen over of the widest range of conditions if partitioning is strong. To achieve strong partitioning with Eq 3.15, the following parameters are used $t = 0.6$, $v = 1$, $w = 0.008$, $B_2^L = -2.97$, $B_0^X = 1$, and $u = 4$, which results in Fig. 3.22.

To demonstrate this dual width effect, Eqs 2.41 are simulated. In the simulations, $\Delta B_0 = 0.2$, $< \epsilon^2 >= 0.001$ in a region of width $60\Delta x$, $\Delta x = 1$, and $\Delta t = 0.01$. Startring an open or closed grain boundary, from the simulation is held at $\psi_s = -0.91$. This results in either an open or a closed boundary, as shown in Fig. 3.23. The hysteresis occurs because there are two liquid states (with different concentrations), which can coexist with the solid. This demonstrates that in addition to structural effects allowing for a hysteresis in grain boundary properties, materials with exotic phase diagrams can also exhibit a hysteresis behaviour due to various phase- and metastable phase-coexistence.

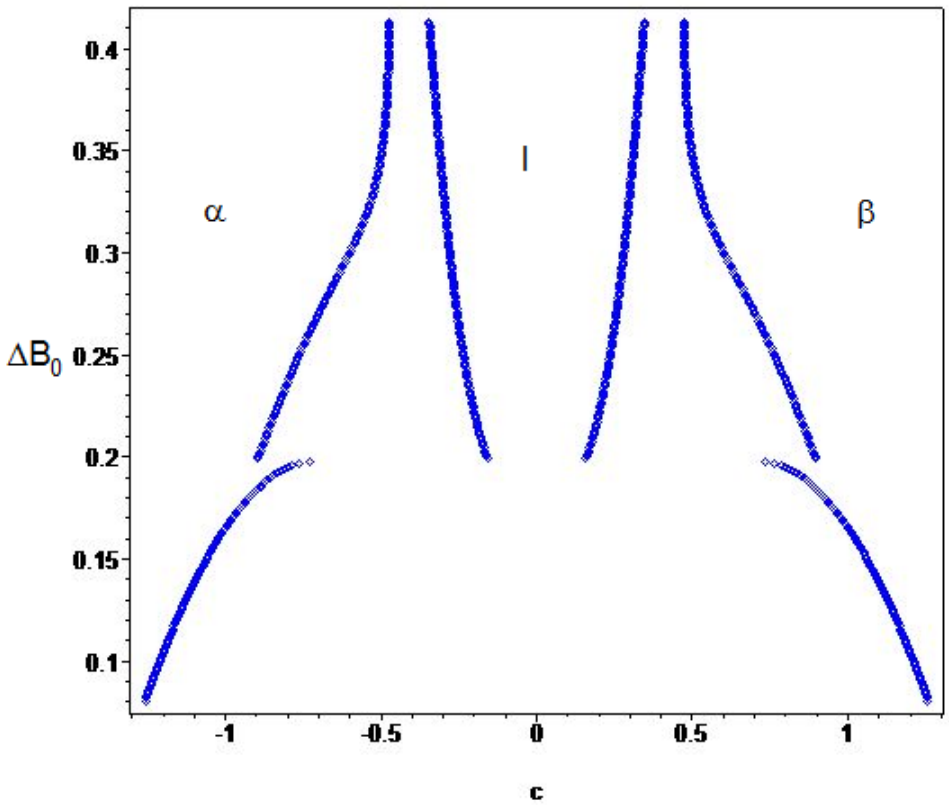

Figure 3.22: ΔB_0 v.s c phase diagram of model being used for hysteresis. There are two solid phases α, β and a liquid phase, l

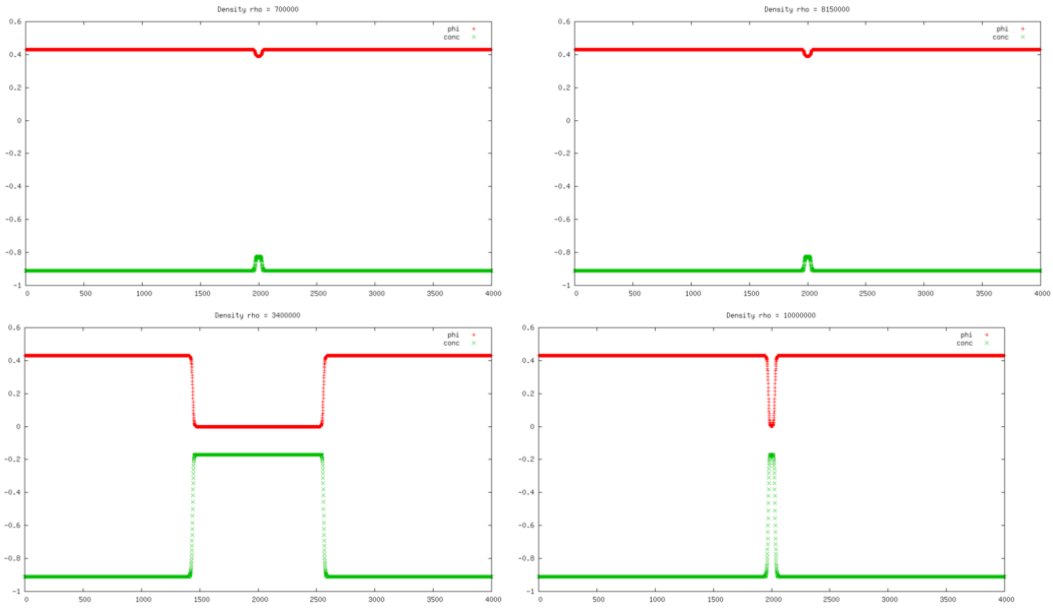

Figure 3.23: Illustration of hysteresis in ϕ (red curves) and c (green curves) using the material with phase diagram in Fig. 3.22 at $\Delta B_0 = 0.2$ and $c_l = --0.91$. Initial condition *(left frames)* and equilibriated state *(right frames)* for small (closed) grain boundary *(top frames)* and large (open) grain boundary *(bottom frames)*.

Chapter 4

Clustering in Alloys

4.1 Introduction

As indicated in section 1.3, the PFC formalsim is an appropriate formalism for studying the formation and behaviour of clusters in alloys because of the time and length scales involves. Because of larger flexibility in defining crystal structures, the XPFC formalism (section 2.4) of [113] (Eq. 2.28) and [118] (Eq. 2.29) was used. Although PFC models are believed to only capture vacancies in a mean-field way—that is, their behaviour is averaged out in the time scales at which the PFC method operates; see Ref. [1]—, they capture the physics of dislocations very well, so this problem is studied in the presence of dislocations and dislocation loops [112]. The results in this section can be found in Refs. [14] and [18].

4.2 Theoretical model for clustering

Because of the transport of different atomic species, the relevant thermodynamic potential is the grand potential, Ω, (usually referred to as G in the work of [14] and [18]) . There are various contributions to the grand potential of a cluster. The simulations are done in 2D and it will be assumed that the cluster shape is a circle of radius R. The most obvious contribution is the grand potential density difference from the cluster to the matrix, $\Delta\omega = \omega_2 - \omega_1$, where ω_2 is the grand potential density of the cluster phase, while ω_1 is the grand potential density of the matrix phase (also referred to as parent or intial phase). Assuming that cluster formation is like a nucleation process, there is a surface energy between the cluster and the matrix, γ. There are also elastic contributions, which are divided into 2 parts; one part is that for coherent nucleation of two crystalline phases with mismatched lattice constant described in section 1.3.2, of which the free energy density is $\Delta\omega_e$, and the other part is the decrease of the elastic energy of the dislocations due to the growth of the cluster, $\Delta\Omega_d$. Also, there is the dislocation core energy, $\Delta\Omega_c$. Summing these terms together gives:

$$W = \pi R^2 \Delta(\omega + \omega_e) + 2\pi R\gamma + \Delta\Omega_d + \Delta\Omega_c \tag{4.1}$$

To determine γ, only the concentration gradient is considered. This means that the dislocations in the interface are ignored, which is a good approximation because they make up only a small portion of the semi-coherent interface and their contribution to the energetics of the problem is considered in Ω_d and Ω_c. As well, the concentration in the cluster at small sizes cannot be considered uniform [69], so simply integrating the concentration from the matrix concentration, c_m to the cluster concentration, c_{cl}, as done in [143] is wrong. Instead, this is approximated by a correction factor of $C_{corr} = 1.3(c_{cl} - c_m)/(c_f - c_m)$, where c_f is the maximum concentration of the cluster and c_{cl}

changes as the cluster grows in size. As as result, the surface tension is approximated as:

$$\gamma = C_{corr} \int_{-\infty}^{\infty} \frac{\alpha}{2} |\nabla c|^2 du = C_{corr} \int_{cb}^{cel} \sqrt{\alpha (f - f_b)} dc \tag{4.2}$$

where u is the a length variable normalized by the interface thickness and α is described in Eq. 2.28. For the ternary model, the only difference is that two fields varying simultaneously which was covered in [143] and is given by the following equation:

$$\gamma = C_{corr} \int_{cb2}^{cel2} \sqrt{\alpha (f - f^b)} \sqrt{1 + \frac{\alpha_3}{\alpha_2} \left(\frac{dc_3}{dc_2} \right)^2} dc_2 \tag{4.3}$$

where the concentration in C_{corr} refers to the concentration of the dominant alloying element.

The elastic energy contribution to grand potential due to coherent growth of the new phase is given by Eq. 1.28. The lattice constants are defined in section 4.2.1, while $\delta = (a_2 - a_1)(c_2 - c_2^b)$ for a binary system, where a_i is the elastic constant of the pure material of the i^{th} component, while ^{b} refers to a bulk phase. In a ternary system, $\delta = (a_2 - a_1)(c_2 - c_2^b) + (a_3 - a_1)(c_3 - c_3^b)$.

The growth of the cluster decreases the strain field the strain field around the dislocations facilitating cluster formation. It is assumed that the precipitate acts like an extended Cottrell atmosphere around the dislocations of the semi-coherent cluster. The magnitude of the elastic energy decrease is assumed to be that expected from the elimination of a dislocation with a Cottrell atmosphere (cf. Eq. 1.16):

$$-\eta_m^2 \chi E A \ln(R) \tag{4.4}$$

where $\chi = (\frac{\partial^2 f}{\partial c^2})^{-1}$ (from Eq. 1.18), $\eta_m = \frac{1}{a} \frac{\partial a}{\partial c}$ is the linear expansion coefficient with respect to concentration (a is the lattice constant), E is the Young's modulus, and

$$A = \frac{G_A \Sigma b_i^2}{4\pi(1 - \nu)} \times \frac{C_{corr}}{1.3} \tag{4.5}$$

It should be noted that the various dislocations contributing to the strain field have been subsumed into one effective strain field, Σb_i^2. Because an equation of the form of Eq. 4.4 has a logarithmic dependence, it is only important at small R because the other terms have R and R^2 dependences. For a ternary alloy, the only change to Eq. 4.4 is that Eq. 1.23 is used; that is

$$\eta_m^2 \chi = \frac{\eta_2 \eta_2 \frac{\partial^2 f}{\partial c_1^2} + \eta_1 \eta_1 \frac{\partial^2 f}{\partial c_2^2} + 2\eta_1 \eta_2 \frac{\partial^2 f}{\partial c_1 \partial c_2}}{\frac{\partial^2 f}{\partial c_1^2} \frac{\partial^2 f}{\partial c_2^2} - \left(\frac{\partial^2 f}{\partial c_1 \partial c_2} \right)^2} \tag{4.6}$$

Finally, the contribution of the core energy to the free energy is

$$\zeta A \tag{4.7}$$

where A is defined by 4.5 and $\zeta \approx 10$ is a prefactor [14, 18], which can be estimated from the average spacing between dislocations (approximately R) and core size, r_0, via Eq. 1.16 (see [66], which gives a smaller estimate for ζ).

4.2.1 Approximation of Elastic Coefficients

Unlike a triangular lattice, the elastic constants in a square lattice are anisotropic. However, given that the model is being used to only approximate the mechanism of cluster formation that occurs,

an isotropic approximation to the elastic constants will be used. Therefore the elastic constants are averaged over all rotations of the system to give effective isotropic elastic constants. Similar to deriving Eq. 2.40 from Eq. 2.38, in one particular basis, the free energy contribution due to the gradient terms is:

$$f_{grad} \approx -\frac{1}{4}\sum_{i,j}\left[A^{\dagger}_{i,j}\left(\frac{\partial^2\hat{C}(k)}{\partial(k^2)^2}\right)_{k=k_{i,j}}(-4\vec{k}_{i,j}\cdot\nabla)A_{i,j}\right] \tag{4.8}$$

where $A_{i,j} = \phi\exp(I\vec{k}_{i,j}\cdot\vec{u})$

After expanding as in section 2.5 and averaging the resulting elastic constants over all angles gives the following expression:

$$\begin{aligned} f_{elast} &\approx \left[\phi^2_{1,0}\left(k^2\frac{\partial^2\hat{C}(k)}{\partial(k^2)^2}\right)_{k=k_{1,0}} + \phi^2_{1,1}\left(k^2\frac{\partial^2\hat{C}(k)}{\partial(k^2)^2}\right)_{k=k_{1,1}}\right] \\ &\times \quad (-3(\epsilon^2_{xx}+\epsilon^2_{yy}) - 2(\epsilon_{xx}\epsilon_{yy}) - 4(\epsilon^2_{xy}))/2 \\ &= \quad C_{11}(\epsilon^2_{xx}+\epsilon^2_{yy})/2 + C_{12}(\epsilon_{xx}\epsilon_{yy}) + 2C_{44}(\epsilon^2_{xy}) \end{aligned} \tag{4.9}$$

From Eq. 4.9, C_{11}, C_{22}, C_{12}, and C_{44} can be used to define the other elastic constants. In 2D, $C_{11} = 8/9E$, $G = C_{44}$, $\nu = 1 - 2G/E = 1/3$. From this it can be deduced that the 2D bulk modulus is

$$K = \frac{E}{2(1-\nu)} \tag{4.10}$$

4.3 Comparison of Theory with Simulations

In this section, the model of a proposed mechanism in section 4.2 is compared to simulations done in [14] and [18]. First, the basic physical mechanisms are illustrated by analysing the binary model, then comparisons with a ternary material are done to elucidate the effect of an additional alloying species. The simulations in [14] and [18] were done with the parameters in the Table 4.1, with the binary material having the phase diagram in Fig. 2.4. The amount of third element alloying is small in the ternary simulations; the equilibrium phases expected change little [18]. It should be noted that the model only simulates the pure Al phase to the precipitate phases, which are considered the other pure material.

4.3.1 Binary alloy simulations

In Fig. 4.1 a)-c), formation of a cluster from a random distribution of dislocations with dislocation density of 1 dislocation per 100 atoms on a 2048x2048 grid is shown. The clusters start around dislocations as Cottrell atmospheres, as suggested by the local minimum in Eq. 1.29 (see [6]). As the dislocations move, they carry solute with them. When multiple dislocations assemble in a stable configuration near each other, the region with enriched solute becomes larger and the average solute density of that region is larger. If the dislocations around the cluster annhilate with other dislocations, then the solute field disperses, eliminating the cluster. This is as would be expected from sub-critical nucleus, which is only stabilized by the presence of a defect. Eventually, if enough defects gather together without annhiliating each other, the amount of solute and area of excess solute increases, leaving a relatively large cluster as seen in [14].

The energetics of the Fig. 4.1 e), the grand potential of a box in a which a cluster grows is shown against the size of the cluster. From the perspective of energetics, the process looks very much like

Table 4.1: Table of Variables and Parameters for Clustering XPFC Simulations

Parameters	Binary XPFC in [14]	Binary XPFC in [18]	Ternary XPFC in [18]
Simulation Dimensions $N_x \times N_y$	$2048x2048$	$4096x4096$	$4096x4096$
Grid Spacing and time increment Δx, Δt	0.125, 1.0	0.125, 10	0.125, 10
mean concentrations c_i, $i = 2, 3$	0.2 , N/A	0.2 , N/A	0.2 , 0.025
mean density n_0	0	0	0
final tempature σ	0.04	0.04	0.04
η, χ	1.3, 1	1.3, 1	1.3, 1
λ	0.035	0.035	0.035
ω, c_{0i}	0.005, 0.5	0.005, 0.5	0.005, 0.3333
$G_{10,i}$, $i = 1, 2, 3$	$0.5/0.8^2$, $0.5/0.8^2$, N/A	$0.5/0.8^2$, $0.5/0.8^2$, N/A	$0.5/0.8^2$, $0.5/0.8^2$, $0.5/0.8^2$
$G_{11,i}$, $i = 1, 2, 3$	$.5/2.4^2/\sqrt{2}$, $.5/2.4^2/\sqrt{2}$, N/A	$0.5/0.8^2/\sqrt{2}$, $0.5/0.8^2/\sqrt{2}$, N/A	$0.5/0.8^2/\sqrt{2}$, $0.5/0.8^2/\sqrt{2}$, $0.5/0.8^2/\sqrt{2}$
$D_{10,i}$, $i = 1, 2, 3$	$1/0.55^2/k_{10,i}^2$	$1/0.55^2/k_{10,i}^2$	$1/0.55^2/k_{10,i}^2$
$D_{11,i}$, $i = 1, 2, 3$	$1/0.55^2/k_{11,i}^2$	$1/0.55^2/k_{11,i}^2$	$1/0.55^2/k_{11,i}^2$
$k_{10,i}$, $i = 1, 2, 3$	2π, $81/38\pi$, N/A	2π, 2.0832π, N/A	2π, 2.0832π, 1.8988π
$k_{11,i}$, $i = 1, 2, 3$	$\sqrt{2}k_{10,i}$	$\sqrt{2}k_{10,i}$	$\sqrt{2}k_{10,i}$
α_{ii}, $i = 2, 3$	1, N/A	1, N/A	$1, 1$
$M_{c,i}$, $i = 2, 3$	1, N/A	1, N/A	$1, 1$

nucleation, despite the lack of thermal noise in the simulations. Fig. 4.1 e) only considers a local grand potential increase in a volume containing the final cluster[14]; as is consistent of dissipative dynamics without noise, the total system grand potential is in fact always decreasing. The local increase is mostly related to the dislocation cores having a very high energy and this is only locally decreased once a large enough cluster forms.

Qualitatively, Fig.4.1 e) corresponds well to Fig. 4.1 d), which is an illustration of how the model captures the energetics of clustering. The local minima for each line in Fig. 4.1 d) correspond to the effective Cottrell atmosphere of a set of clusters with effective square Burgers vector $\sum b_i^2$. As in [6], once the strength of the logarithmic term becomes large enough, there is no barrier to the formation of the precipitate. The grand potential decrease stops in the simulation systems because of the finite size of the system; the system has reached a metastable equilibrium between the cluster and the matrix (see section 4.4).

4.3.2 Effects in Ternary alloys

In [18], differences in cluster formation relating to material composition are elucidated. In Fig. 4.7, the differences in the physical features of the clusters formed between a binary Al-1.1at%Cu alloy and a 3-component Al-1.1at%Cu-0.2at%Mg alloy are very apparent. With the presence of the ternary alloying element, Mg, more and finer clusters form in a comparable simulation than in the binary case. The size and frequency of clusters is given in the histogram in Fig. 4.7.

Some light is shed on these differences by comparing with Eq. 4.2. In Fig. 4.4, the thermo-

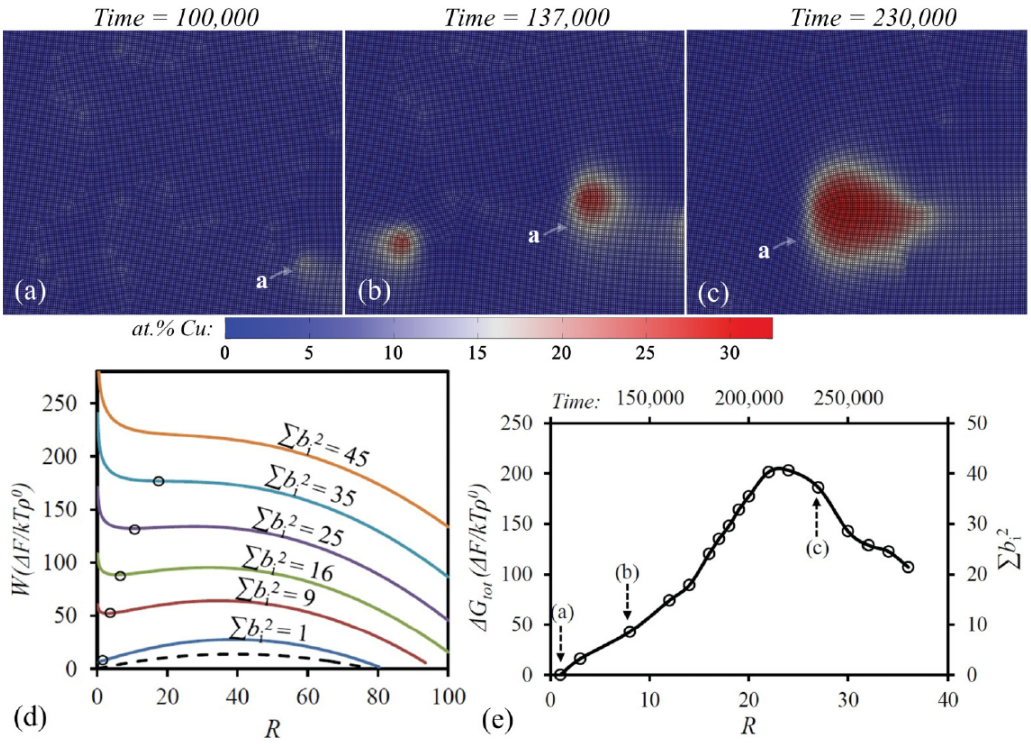

Figure 4.1: Snapshots of cluster formation for a binary Al-1.1Cu alloy *(top frames)*. The bottom frames include the local free energy density of the cluster as given by the theoretical model with $\lambda = 0$ *(left, d)* and simulations *(right, e)*. In the simulations c_{cl} changes from 0.65 to 0.8 and c_{mat} from 0.2 to 0.176, From [14]

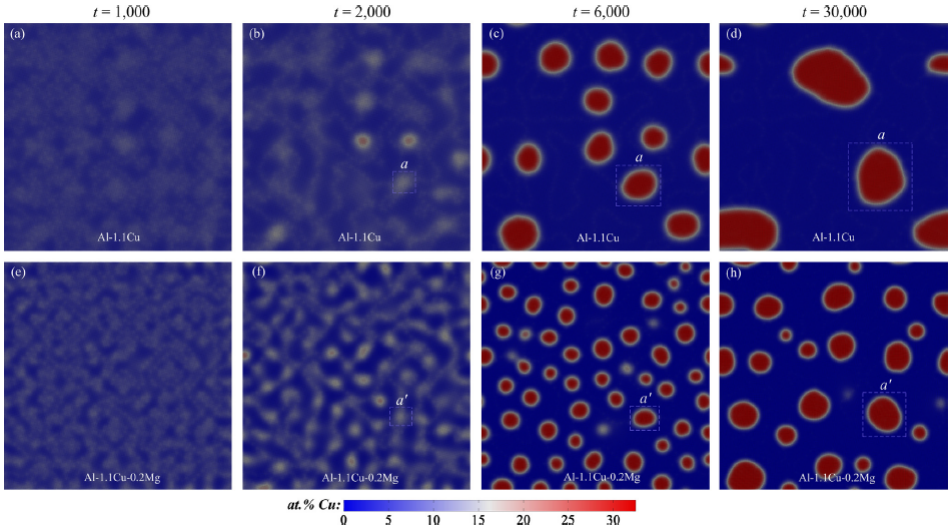

Figure 4.2: Snapshots of cluster formation for a binary Al-1.1Cu alloy *(top frames)*, Al-1.1Cu-0.2Mg alloy) *(bottom frames)* over time. In the left most frames, are the initial states of the system. In the right most frame are essentially the final states of the (finite size) system. The clusters are fewer but larger the binary material than in the ternary alloy. From [18]

dynamics of cluster formation is illustrated. In the left most image Fig. 4.4 a), no dislocations are assumed to be present. The nucleation barrier is very large. Without noise, a new phase will not form and even with noise, it might take a long time, though less so for the ternary alloy with the smaller nucleation barrier and critical radius. In Fig. 4.4 b), the effect of dislocations is included and 2 things can be observed: the nucleation barrier is lower with dislocations than without (though this does not correspond to the true height of the barrier as shown in Fig. 4.1, but it is a good approximation) and the barrier for the ternary is lower than the binary. Finally, the simulations show that the clusters in the ternary simulations have a much lower peak grand potential density in a finite-sized region around the cluster, which suggests that they should form more readily as is observed.

4.4 Discussion

This problem of cluster formation and the final state of the clusters can be seen from an alternate point of view, namely that of phase coexistence. As noted earlier and deduceable from the stress fields in Eq. 1.20, there is a strain field around a dislocation, which attracts solute particles. As observed, many dislocations may be attracted by the solute and orient themselves to increase the amount of solute, thereby increasing the strain of the solute enriched region relative to the matrix lattice constant. To demonstrate how this might give rise to coexistence of a metastable species under strain with the unstrained matrix, an amplitude expansion of the free energy Eq. 2.22, noting the changes implied by Eq. 4.8, was studied in [14]. The average strain field relative to that of the matrix from the simulations for various points in time around a growing cluster was computed. Substituting $U_{xx} = U_{yy} = \epsilon$ into Eq. 2.22 gives the free energy curves shown in Fig. 4.5. At low average ϵ, a common tangent between a phase with slightly higher concentration than the matrix can be drawn; this corresponds to the early stage clusters. However, at larger ϵ, Fig. 4.5 shows that a common tangent with the matrix phase can only be drawn with a phase with much larger concentration. This corresponds to the larger clusters, which can eventually grown into precipitates.

Similiarly, the Cottrell atmospheres in ternary alloys can also be considered phases in coexis-

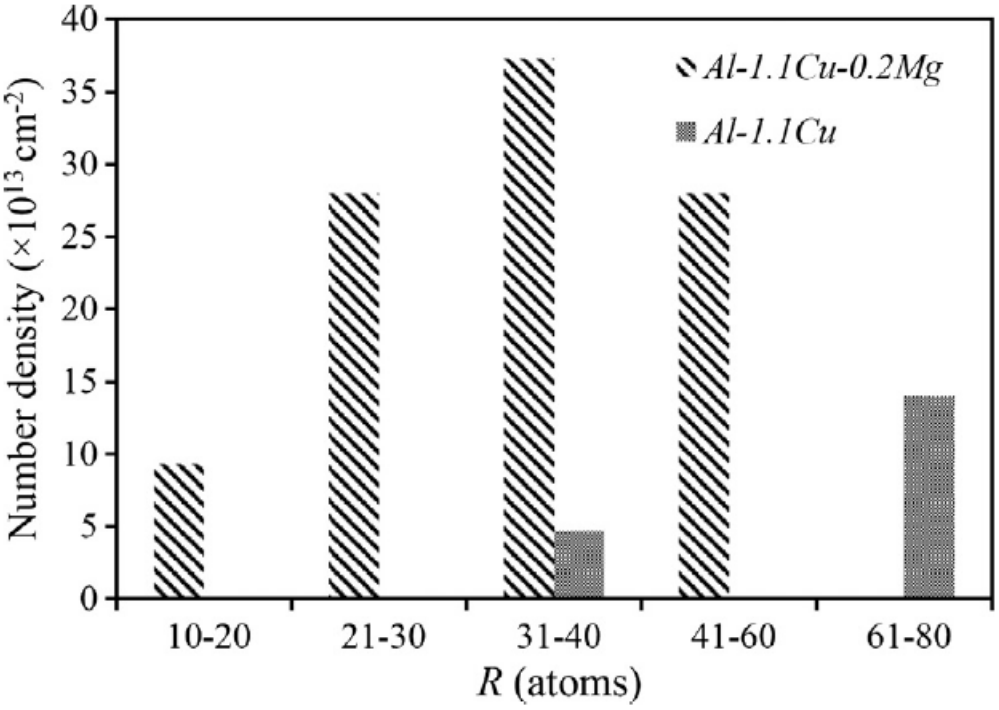

Figure 4.3: Histogram of Number of clusters of a particular size for 4096x4096 simulations of Al-1.1Cu and Al-1.1Cu-0.2Mg. From [18].

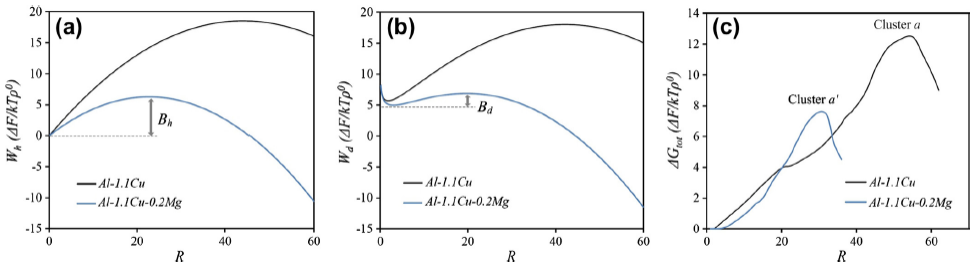

Figure 4.4: Energetics of cluster formation in ternary alloys. Eq. 4.2 with $\Omega_d = \Omega_c = 0$ and $\lambda = 0.02$ *(left frame)*. Eq. 4.2 with $\lambda = 0.02$ *(centre frame)*. Work of formation in region around cluster in simuation *(right frame)*. Black curves are of Al-1.1Cu, while blue curves are of Al-1.1Cu-0.2Mg. From [18].

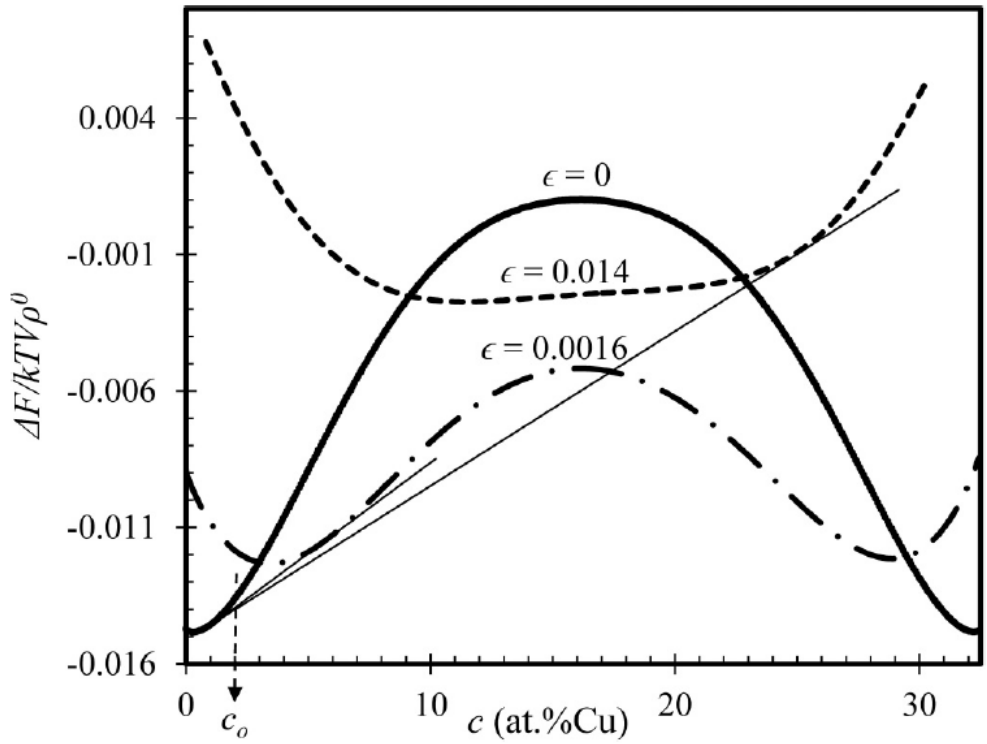

Figure 4.5: Free energy versus concentration when the average strain of the system changes. Common tangent constructions between the unstrained phase $\epsilon = 0$ and slightly strained $\epsilon = 0.0016$ and very strained phases $\epsilon = 0.014$. Note that $\lambda = 0$ for all curves. From [14].

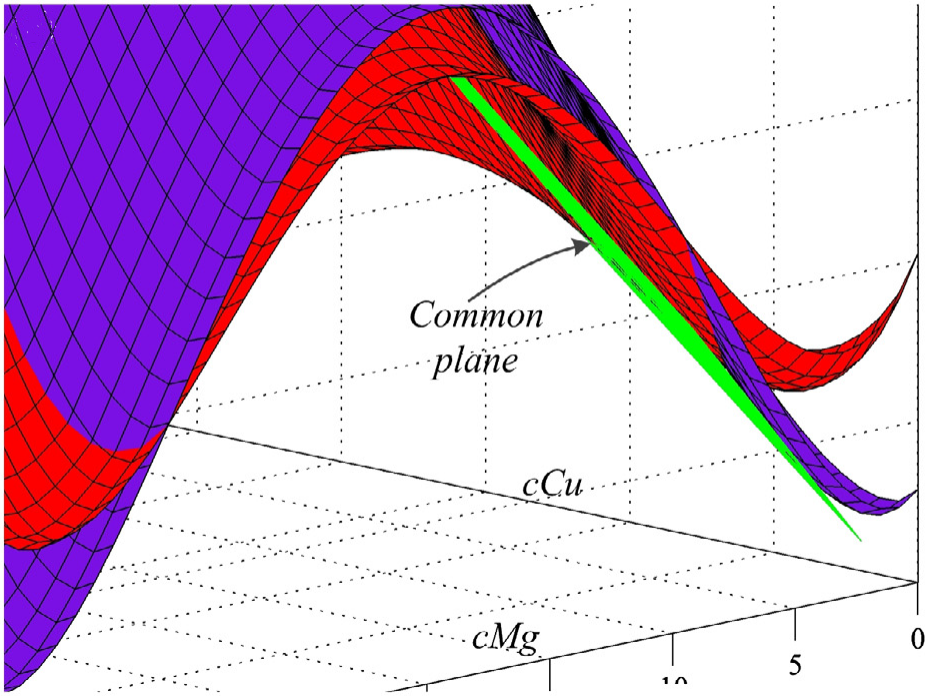

Figure 4.6: Free energy of unstrained *(blue surface)* and slightly strained *(red surface)* versus composition, c_{Mg} and c_{Cu}. A green common plane is drain between the phases indicating the composition of the strained (part of the Cottrell atmosphere) and unstrained (matrix) phases. Parameters are the same as in simulations except $\lambda = 0.02$. Adapted from [18].

tence with the matrix phase in a ternary alloy. Fig. 4.6 show the common plane construction between the free energy of the matrix phase and strained phase.

An effect on cluster composition related to stress is also observed in ternary alloys, which is shown in Fig. 4.7. Unlike in binary alloys, the stress field does not need be as large to allow the precipitate to form because the presence of Mg changes the sign of the lattice constant in the opposite direction of Cu. This makes the precipitate have a closer lattice constant to that matrix phase, so that stress inhibits the formation of the cluster less. Once the cluster grows large enough, the Mg is expelled from the Cu-rich phase because its lattice constant is very different from that of the Cu-rich phase.

Although all of these effects were studied in 2D, they can be expected to be qualitatively correct in 3D. This work was continued in [64], in which a more direct comparison between simulations and experiments for a binary alloy could be made. The model and experiments show many of the same features, such as the presence of dislocations around the clusters to help stabilize them and similar concentration profiles between the matrix and clusters, which are also present in 2D. The biggest difference observed between the 2D and 3D simulations was the anistropic growth of clusters along the close-packed planes in 3D, which is also seen in TEM analysis of the samples.

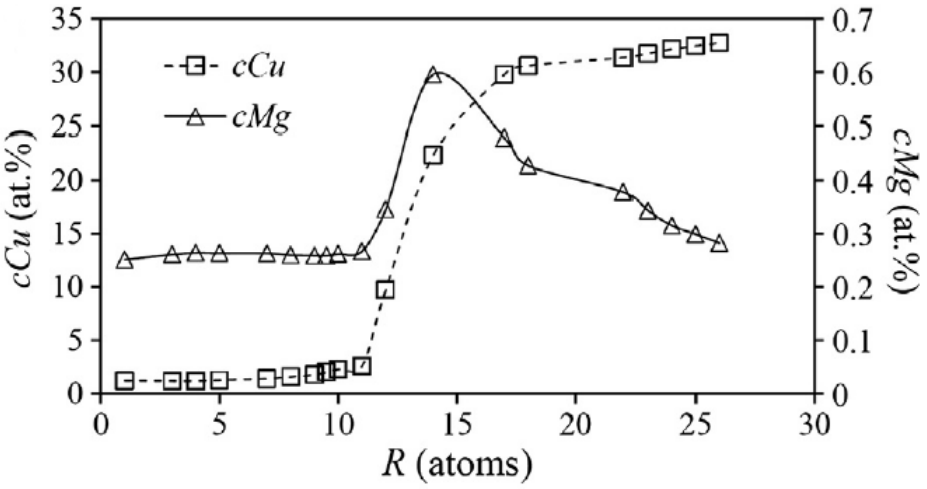

Figure 4.7: Average Concentration of Cu and Mg in cluster as cluster radius, R, changes. Adapted from [18].

Chapter 5

Explosive Crystallization

5.1 Introduction

Past work, such as the one on Ref. [11], showed that reaction-diffusion-type approaches are useful to understand the origin of undulations found in explosive crystallization. These approaches however, oversimplify the fundamentals of the reaction kinetics, ignore interface effects and have no connections to the local crystalline ordering and elasto-plastic effects. The connection of PFC models to more fundamental theories was noted in section 2.5, which implies that the PFC model has parameters which can in principle be directly linked to atomistic properties. However, the PFC model can also be used to generate coarse-grained theories from which emerge phase field models and, ultimately, reaction diffusion models. As such, an appropriate PFC model can be considered a generator of various phenomenologies on multiple scales, carrying into each scale the salient features of interfaces, grain boundaries and elasticity, features traditionally put (or parameterized) in "by hand" into phenomenological models on higher scales. In this chapter, the PFC formalism is used to derive phase field model of explosive crystallization that naturally contains the effects of elasticity and solute diffusion.

5.2 PFC-based model of Explosive Crystallization and Physical Setup

A typical solidification phase transition is taken as the starting point to considering explosive crystallization; that is, the model distinguishes between a stable (solid) state and a metastable (disordered) state. For this purpose, the PFC free energy similar to that found in section 2.3 is sufficient. In this approach, it is assumed that there is a sufficiently large liquid layer between the crystalline and amorphous states and that the liquid state properties do not differ substantially from those of the amorphous material. In this sense, the results of this chapter are directly applicable to the study of explosive liquid phase crystallization (ELPC).

Free energy density

The PFC free energy is adapted in two ways to study the problem of explosive crystallization: the coefficients of the density dependent terms are chosen such that the coarse-grained free energy wells of the phases mimic a typical 4^{th}-order PF free energy and the concentration dependent terms of Eq. 2.20 are changed such that the model is appropriate for studying a dilute binary alloy, examples of which can be found in Refs. [19, 3]. It should be noted that bulk free energy density depends on the resultant crystal structures, which depend on the dimension of the system; the coefficients are

chosen such that the energetics of the transition between the 2D hexagonal state and the uniform liquid state correspond to the energetics of a typical 2-state PF free energy. These considerations result in the following free energy density for the transforming system,

$$f = \frac{B^L}{2}n^2 - \frac{t}{3}n^3 + \frac{v}{4}n^4 + \frac{B^X}{2}n(2(1+2\eta c)\nabla^2 + (1+4\eta c)\nabla^4)n + \frac{RT}{v_M}(c\ln c - c) + \frac{K_c}{2}|\nabla c|^2 \quad (5.1)$$

where the parameters of the original PFC model are here re-defined as,

$$\begin{aligned} B^L &= (h + 3\Delta\epsilon c + 3L(T-T_M)/T_M)\phi_0^2/3 + B^X \\ t &= (h + \Delta\epsilon c + L(T-T_M)/T_M)\phi_0/2 \\ v &= 2h/45 \\ B^X &= K\phi_0^2/12 \end{aligned} \quad (5.2)$$

where η is the size mismatch between the two atomic species, K_c is the gradient squared coefficient of the concentration term, and ϕ_0 is the equilibrium amplitude of the oscillation in the solid phase, which is exactly the value of the amplitude realized when $\eta = 0$. From the phase field model of Ref. [3], T_M is the melting point of the pure material, T is the temperature field in the material, L is latent heat of fusion in the pure material, $\Delta\epsilon$ is the energy change with concentration between solid and liquid, h is the nucleation barrier, R/v_M is the gas constant divided by the molar volume of the material, and K is the coefficient of the ϕ- gradient squared term.

By comparing Eq. 5.1 to Eq. 2.20 and recalling that Eq. 2.40 was derived from Eq. 2.20, one arrives at an amplitude free energy under conditions described in this section,

$$\begin{aligned} f &= 3B^L\phi^2 - 4t\phi^3 + 45vn^4/2 + 6B^X|\nabla\phi|^2 + \frac{RT}{v_M}(c\ln c - c) \\ &+ 3B^X\left(\frac{3}{2}(U_{xx}^2 + U_{yy}^2) + U_{xx}U_{yy} + 2U_{xy}^2\right) \\ &+ 12B^X\eta c\left(-\phi\nabla^2\phi + (U_{xx}+U_{yy})\phi^2\right) \end{aligned} \quad (5.3)$$

where U_{ij} are the various strain components. The ampltiude field, ϕ, can be replaced by the normalized amplitude field, $A = \phi/\phi_0$. A phase diagram for this free energy when $\eta = 0$ is given in Fig. 5.1. Although Eq. 5.3 is appropriate for studying the liquid to hexagonal phase transition in 2D, analogous changes to the PFC free energy can also be done to capture a transistion between a uniform liquid state and the 3D BCC crystal structure. It is also noteworthy that these changes to the original model of Ref. 2.20 gives rise to a much more realistic equilibrium phase digram of a binary alloy.

Dynamics

Driving forces for the dynamics of the A and c fields are determined by using functional derivatives of the free energy in Eq. 5.3, as was done in section 2.5. The dynanics of A and c fields follow non-conserved and conserved fields, respectively:

$$\begin{aligned} \frac{\partial A}{\partial t} &= -M_1(T)\tfrac{\delta F_{PF}}{\delta A} \\ \frac{\partial c}{\partial t} &= \nabla\left[M_c(T,\phi)c\cdot\nabla\left(\tfrac{\delta F_{PF}}{\delta c}\right)\right] \end{aligned} \quad (5.4)$$

where F_{PF} is Eq.5.3 integrated over the system volume, $M_1(T)$ is the mobility of the phase field and $M_c(T,\phi)c = \hat{M}_c(T,\phi) = M_{c0}(1-\tanh(\xi\phi))$ is the mobility of the concentration field, where ξ and M_{c0} are parameters to fit the mobility through the interface. Analogously to Provatas et al.

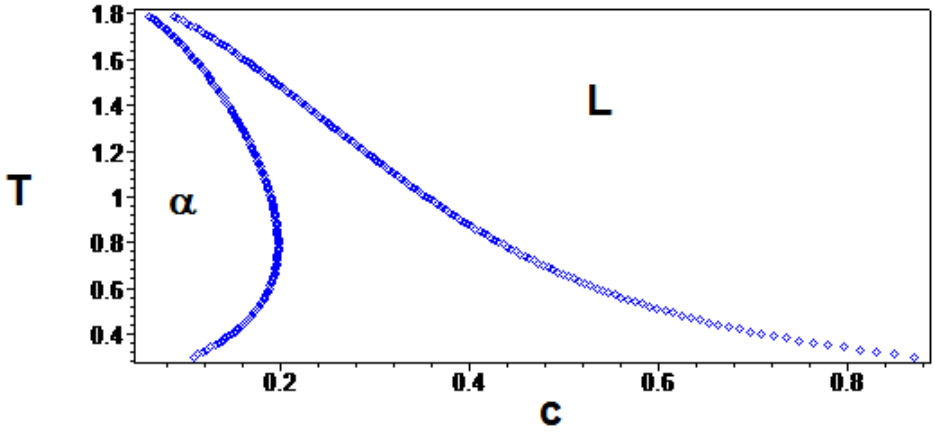

Figure 5.1: Phase diagram for Eq. 5.3 with $T_M = 1.8$, $\phi_0 = 1/20$, $\eta = 0$, $K = 2000$, $R/v = 1/25$, $\Delta\epsilon = 10$, $h = 10$, $L = 3$, where α is the solid phase and L is the liquid phase.

[11], the temperature field follows

$$\frac{\partial T}{\partial t} = M_T \frac{\partial^2 T}{\partial x^2} - \Gamma(T - T_0) + q\frac{\partial A}{\partial t} \tag{5.5}$$

where T_0 is the substrate temperature, on which rests the thin amorphous film undergoing explosive crystallization. The parameter M_T is the thermal diffusion coefficient. As with Eq. 1.31, the first term relates to heat diffusion, the second heat losses through the substrate by Newton's law of cooling, likely through conduction (diffusion) though other means are possible, and the third the latent heat generated via phase transformation. It should be noted that this expression neglects the energy of mixing; heat released within a phase due to composition is assumed to be much smaller than the latent heat. Although the change in latent heat due to concentration changes, can be significant, in this phenomenon, concentration does not change much, and as such latent heat can be rescaled to its value for the initial concentration.

Finally, to relax the strain fields, the boundary conditions need to be considered appropriately. In the model used, this is a 2D problem, though it should be noted that even in 3D the elasticity problem can be considered as a 2D problem; the z-direction is eliminated from consideration because the plane stress approximation is valid due to the film being much thinner in the z direction ($\sim< O(\mu m)$) than in the y and x directions ($\sim O(mm)$) [7, 70]. Also note, that this being a one dimensional problem, none of the fields being considered have a y-dependence. To derive a relation which is consistent in the y-direction, the thin film is assumed to be held in place by insulating walls whose positions do not change much with temperature. Therefore $U_{yy} = 0$ and if $\sigma_{yy} = 0$, then $U_{yy} = \frac{\partial v}{\partial y} \Rightarrow v(x, y)$, meaning that $U_{xy}(x, y)$ or $U_{xx}(x, y)$, where the y-dependence is incompatible with our rest of the equations. Also, the stress, σ_{xx}, is taken to be far from the reactng system. Therefore, the force balance in Eq. 2.42 is written as:

$$\begin{aligned}
\frac{\partial}{\partial x}\sigma_{xx} + \frac{\partial}{\partial y}\sigma_{xy} &= 0 \\
\frac{\partial}{\partial x}\left(9B^X\phi^2 U_{xx} + 2B^X\phi^2 U_{yy} + 3B^X\phi^2 c^2\right) + \frac{\partial}{\partial y}\left(12B^X\phi^2 U_{xy}\right) &= 0 \\
\frac{\partial}{\partial x}\left(6B^X\phi^2 U_{xx} + 12B^X\phi^2 c^2\right) &= 0
\end{aligned} \tag{5.6}$$

and

$$\begin{aligned} \frac{\partial}{\partial y}\sigma_{yy} + \frac{\partial}{\partial x}\sigma_{yx} &= 0 \\ \frac{\partial}{\partial y}\left(9B^X phi^2 U_{yy} + 3B^X phi^2 U_{xx} + 12B^X phi^2 c^2\right) + \frac{\partial}{\partial x}\left(12B^X phi^2 U_{xy}\right) &= 0 \\ \frac{\partial}{\partial x}\left(12B^X phi^2 U_{xy}\right) &= 0 \end{aligned}$$

In the second equation, the shear strain is 0, so a simple identity relation is obeyed.

5.2.1 Thermodynamic consistency

For the case that $\eta = 0$, Eq. 5.3 is known to be thermodynamically consistent and this form is commonly used in phase field-type models because of this (cf., Refs. [19, 3]). This can easily be checked by applying the following relation to Eq. 5.3:

$$E = F + TS = F + T\left(\frac{\partial F}{\partial T}\right)_{V,N} \tag{5.7}$$

where E is the energy of the system, F is the Helmholtz free energy of the system, T is the temperature, and S is the entropy of the system, which gives $E_L - E_\alpha = LV_{tot}$ for a pure material and $E_L - E_\alpha = (L + \Delta\epsilon c_s)V_{tot}$ for an alloy, where c_s is the solid concentration and V_{tot} is the volume of the system. Therefore q should vary as the system concentration changes, though as noted above, change in energy due to mixing in the liquid are ignored. Assuming no change in heat capacity of the material, assuming $A \approx 1$, and approximating the change in atomic spacing via the η-dependent terms, the following expression for q in obtained,

$$q = q(c_s = 0)\frac{L - \Delta\epsilon c_s + K\eta^2 c_s^2}{L} \tag{5.8}$$

where the $q(c = 0)$ is the normalized latent heat of the pure material. The assumption that $A = 1$ gives a good estimate for the latent heat in the case of complete trapping because the change in Eq. 5.8, $\delta q/q(c = 0)$, for $A = 1 + \delta A$ is small, i.e.,

$$\frac{\delta q}{q(c_s = 0)} \approx \frac{2K\eta^2 c_s^2 \delta A}{L} \tag{5.9}$$

As a conservative estimate, $\delta A \sim 0.05$, $\eta \sim 0.2$, $c_s \sim 0.1$ is considered. If $L = 3$, this change is about 2% in the total latent heat released. In fact, in the simulations done, this change was much smaller and so this effect can be ignored.

5.3 Sharp Interface Limit of Diffuse Interface

As shown in Ref. [11], a chemical reaction-diffusion model of explosive crystallization can be linked to a sharp interface model of the process. This section demonstrated the inherent properties of our new phase field model by deriving its lowest order sharp interface limit using a projection operator approach [144]. The problem is considered in 1D, where x is the coordinate perpendicular to the interface. First, Eqs. 5.4 and 5.5 are translated to a co-moving frame of reference, where $x = 0$ corresponds to $A = 1/2$ (though a convenient Gibbs interface can be used as in Ref. [144]) and V corresponds to the velocity of the interface. Converting the coordinates from the laboratory frame

to the comoving frame the time derivatives from the lab frame map to:

$$\frac{\partial}{\partial t} \rightarrow \frac{\partial}{\partial t} - V\frac{\partial}{\partial x} \tag{5.10}$$

By applying Eq. 5.10 to the equations of motion, they become:

$$\begin{aligned}
\frac{\partial A}{\partial t} - V\frac{\partial A}{\partial x} &= -M_1(T)\frac{\partial f_b}{\partial A} + M_1(T)K\frac{\partial^2 A}{\partial x^2} \\
\frac{\partial c}{\partial t} - V\frac{\partial c}{\partial x} &= \frac{\partial}{\partial x}\left(M_c(T,A)c\frac{\partial \mu}{\partial x}\right) \\
\frac{\partial T}{\partial t} - V\frac{\partial T}{\partial x} &= k\frac{\partial^2 T}{\partial x^2} - \Gamma(T-T_0) + q\frac{\partial A}{\partial t} - Vq\frac{\partial A}{\partial x}
\end{aligned} \tag{5.11}$$

where $\mu = \frac{\delta F_{PF}}{\delta c}$. It should be noted that Eq. 5.6 stays the same because it contains no time dependence.

5.3.1 Flux Boundary Conditions for Concentration in Sharp Interface Limit

The concentration equation in Eq. 5.11 is integrated from $x = -W/2$ to $W/2$. Considering only the steady state, in a comoving frame, $\frac{\partial}{\partial t} = 0$, the concentration equation becomes,

$$\begin{aligned}
\int_{-W/2}^{W/2} \frac{\partial c}{\partial t} - V\frac{\partial c}{\partial x}dx &= \int_{-W/2}^{W/2} \frac{\partial}{\partial x}\left(M_c(T,A)c\frac{\partial \mu}{\partial x}\right)dx \\
(0 - Vc)_{-W/2}^{W/2} &= \left(\left(M_c(T,A)c\frac{\partial \mu}{\partial x}\right)\right)_{-W/2}^{W/2} \\
-V(c(W/2) - c(-W/2)) &= \left(M_c(T,A)c\frac{\partial \mu}{\partial x}\right)_{W/2} - \left(M_c(T,A)c\frac{\partial \mu}{\partial x}\right)_{-W/2}
\end{aligned} \tag{5.12}$$

Taking the limit as W goes to 0, gives the boundary condition for the concentration field at the transition between solid and liquid phases:

$$-V(c(0+) - c(0-)) = \left(M_c(T,A)c\frac{\partial \mu}{\partial x}\right)_{0+} - \left(M_c(T,A)c\frac{\partial \mu}{\partial x}\right)_{0-} \tag{5.13}$$

5.3.2 Flux Boundary Conditions for Temperature in Sharp Interface Limit

The temperature field is manipulated similarly to the concentration field, however, it should be noted that the temperature field is continuous across the interface. This gives,

$$\begin{aligned}
\int_{-W/2}^{W/2} \frac{\partial T}{\partial t} - V\frac{\partial T}{\partial x}dx &= \int_{-W/2}^{W/2} M_T\frac{\partial^2 T}{\partial x^2} - \Gamma(T-T_0) + q\frac{\partial A}{\partial t} - Vq\frac{\partial A}{\partial x}dx \\
(0 - VT)_{-W/2}^{W/2} &= \left(M_T\left(\frac{\partial T}{\partial x}\right) - \Gamma(T-T_0) - VqA\right)_{-W/2}^{W/2} \\
0 &= M_T\left(\frac{\partial T}{\partial x}\right)_{W/2} - M_T\left(\frac{\partial T}{\partial x}\right)_{-W/2} - (VqA)_{W/2} + (VqA)_{-W/2}
\end{aligned} \tag{5.14}$$

Taking the limit as W goes to 0 and noting that in the sharp interface limit $\frac{\partial A}{\partial x} = -\delta(x)$ *, gives the boundary condition for the concentration field at the transition between solid and liquid phases:

$$0 = M_T \left(\frac{\partial T}{\partial x}\right)_{W/2} - M_T \left(\frac{\partial T}{\partial x}\right)_{-W/2} + Vq \tag{5.15}$$

5.3.3 Relating Phase Field to Interface Temperature in the Sharp Interface Limit

The last step is to relate V to the temperature at the interface. Considering the steady state, the amplitude (phase field) equation is multiplied by $\frac{\partial A}{\partial x}$ and then integrated from $\pm\infty$. the integral is broken up into 3 different domains:

$$\begin{aligned}
\int_{-\infty}^{\infty} \frac{\partial A}{\partial t}\frac{\partial A}{\partial x} - V\left(\frac{\partial A}{\partial x}\right)^2 dx &= \int_{-\infty}^{\infty} -M_1(T)\frac{\partial f_b}{\partial A}\frac{\partial A}{\partial x} + M_1(T)K\frac{\partial^2 A}{\partial x^2}\frac{\partial A}{\partial x}dx \\
\int_{-\infty}^{\infty} -V\left(\frac{\partial A}{\partial x}\right)^2 dx &= \int_{-\infty}^{\infty} -M_1(T)\frac{\partial f_b}{\partial A}\frac{\partial A}{\partial x} + M_1(T)K\frac{1}{2}\frac{\partial}{\partial x}\left(\frac{\partial A}{\partial x}\right)^2 dx \\
V \times C &= \int_{pW/2}^{\infty} -M_1(T)\frac{\partial f_b}{\partial \phi}\frac{\partial \phi}{\partial x} + M_1(T)K_1\frac{1}{2}\frac{\partial}{\partial x}\left(\frac{\partial \phi}{\partial x}\right)^2 dx \\
&\quad + \int_{-pW/2}^{pW/2} -M_1(T)\frac{\partial f_b}{\partial \phi}\frac{\partial \phi}{\partial x} + M_1(T)K_1\frac{1}{2}\frac{\partial}{\partial x}\left(\frac{\partial \phi}{\partial x}\right)^2 dx \\
&\quad + \int_{-\infty}^{-pW/2} -M_1(T)\frac{\partial f_b}{\partial \phi}\frac{\partial \phi}{\partial x} + M_1(T)K_1\frac{1}{2}\frac{\partial}{\partial x}\left(\frac{\partial \phi}{\partial x}\right)^2 dx
\end{aligned} \tag{5.16}$$

where $C = \int \left(\frac{\partial A}{\partial x}\right)^2 dx$. Normally, the phase field equation cannot be easily manipulated with the projection method because f_b is a function of c, A, T, and U_{ij}. It should be noted that the temperature can be relatively constant in the interface because temperature diffusion is very fast; that is, in limits where the interface is small compared to the capillary length, $M(T) \approx M(T_b)$, where T_b is the interface temperature, for $-pW < x < pW$, where p is a large number so that the entire interface is at approximately constant temperature. As well, nearly complete solute trapping of c is observed for very fast moving interfaces [116], so in this limit, c can be approximated as relatively constant. If c is constant, so are the U_{ij}. These approximations allow one to write the terms $\int_{pW/2}^{\infty} g(A, \partial_x A, \partial_x^2 A)dx = 0$ and $\int_{-\infty}^{pW/2} g(A, \partial_x A, \partial_x^2 A)dx = 0$, where g is any well-behaved function. Therefore, Eq. 5.16 can be simplified to,

$$\begin{aligned}
-V \times C &= \int_{-pW/2}^{pW/2} \left(-M_1(T_b)\frac{\partial f_b}{\partial A}\frac{\partial A}{\partial x} + M_1(T_b)K_1\frac{1}{2}\frac{\partial}{\partial x}\left(\frac{\partial A}{\partial x}\right)^2\right) dx \\
V \times C &= M_1(T_b)\int_{-pW/2}^{pW/2} \left(\frac{\partial f_b}{\partial x} - K_1\frac{1}{2}\frac{\partial}{\partial x}\left(\frac{\partial A}{\partial x}\right)^2\right) dx \\
V \times C &= M_1(T_b)\left(f - \frac{\partial A}{\partial x}\right)_{-pW/2}^{pW/2} \\
V &= \frac{M_1(T_b)}{C}\left(f_l - f_s\right)
\end{aligned} \tag{5.17}$$

*This tacitly assumes that the order parameter is well approximated by particular class of functions, analogous to, say, $A \sim \tanh(x/W)$. This is nearly always a valid approximation for fourth order Ginzburg-Landau type functionals.

In the case that concentration varies, a Gibbs surface could be picked so that the contributions of the excess chemical potential, μ, and excess concentration c, on one side of the interface (approximately) cancel out the other (cf. Ref. [144]), changing $f_l - f_s$ in Eq. 5.17 to $\omega_l - \omega_s$, where $\omega = f - \mu c$. Also, in some situations, if the peak in the mobility function is sharp enough, Laplace's method may be used to evaluate Eq. 5.16 when T varies [145].

Despite the approximations made to derive Eqs. (5.13,5.15,5.17), this procedure makes manifest the inherent connection between this PFC model and the original sharp interface model of [10]. However, since all the parameters on the left hand side of Eq. 5.2 are relatable to the two-point correlation function of a liquid or amorphous phase, these parameters can in principle now be made directly quantitative with some minor effort. Finally, note that the factor $f_l - f_s$ appearing in Eq. 5.17 is a fundamental generalization of the double Arrhenius form in the phenomenological expression in square brackets in Eq. 1.30, used in previous studies assumed from stochastic growth by attachment of atoms to an interface by overcoming an energy barrier (e.g., solid phase epitaxy of Si in [77]).

5.3.4 Application to Vegard's Law in PFC Amplitude equations

With the starting point of Eq. 5.17, the effect of mismatch on the stability of an explosively crystallizing front can be worked out. From Eq. 5.3, f_s and f_l can be determined. To determine the effect of η on C, it should be noted that $C \sim \frac{1}{W_0}$ [146], where W_0^2 is the gradient prefactor of the phase field equation. From Eq.5.3, the following approximation for W_0^2 can be used:

$$\frac{C}{C(\eta = 0)} \approx \frac{1}{1 + 2\eta c} \tag{5.18}$$

The ratio, $V/V(\eta = 0)$ is considered by using Eq. 5.17, Eq. 5.18, Eq. 5.3, and an Arrhenius dependence for M_1. These expressions will be used below to track the relative stability of the steady state solutions at a given temperature using the stability quantities, α and β defined in Eqs. 1.37 and 1.38. Specifically, a numerical analysis will reveal that the solutions with mismatch are less stable (larger α not compensated enough by a larger β) at a given substrate temperature T_0.

5.4 Simulations

Simulations of Eqs. 5.4 and 5.5 are done in 1D, and can thus be solved efficiently enough with simple Euler time-stepping. Odd spatial derivaties are done with simple forward differencing, while even ones are done with a second order central difference scheme. For determining $\frac{\partial \phi}{\partial t}$, a simple backward-difference scheme is used. Because the strain fields equilibriate quickly compared with the motion of the other fields, only one iteration of a Gauss-Seidel algorithm was used per timestep for Eq. 5.6. The main simulations involved following the solid-liquid reaction front started from a solid seed in large 1D systems for a wide variety of substrate temperatures. The parameters used in all simulation are given in Table 5.1, unless otherwise stated. A snapshot showing all 4 fields for one time step of a simulation for both $\eta = 0$ and $\eta = 0.1$ is shown in Fig. 5.2.

For a few oscillatory runs ($T_0 = 0.31575, 0.316, 0.317$), the maximum temperature field with time and concentration field in space are shown. Figs. 5.3-5.5 only displays results from simulations with $\eta = 0$ since the oscillations in concentration are small on the scale of the graph. Although the oscillations in concentration are small in absolute terms, they are still of on the order that is very important for altering electrical or optical properties of a semiconductor films.

As the substrate temperature T_o changes, the extrema of the peak temperatures realized in the simulations undergo a bifurcations sequence. This was shown by Ref. [11] to map onto the Feigenbaum sequence produced by nonlinear mappings with a quadratic maximum. The PFC-derived formalism we introduce in this work allows one to capture, for the first time, the change in bifurcations arising from elastic mismatch. This is demonstrated in the bifurcation diagram shown in

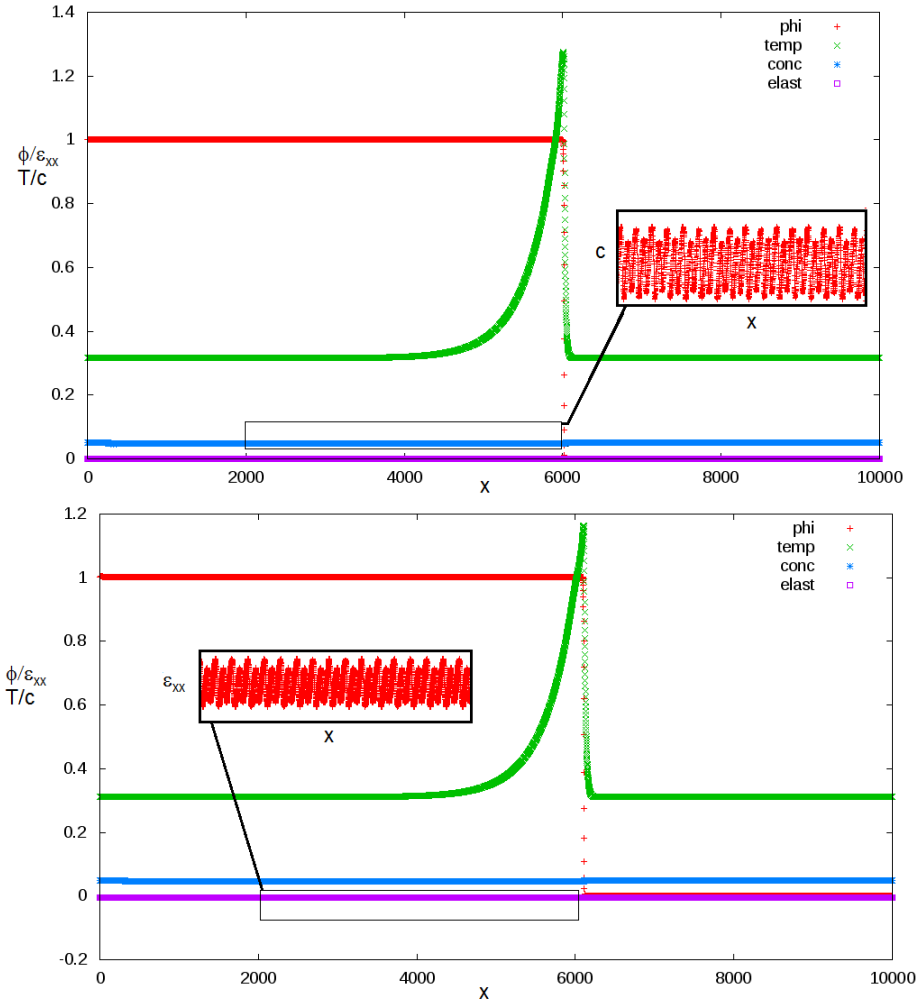

Figure 5.2: T, ϵ_{xx}, c, ϕ versus position, x, for $\eta = 0$ and $T_0 = 0.31575$ ((top frame)) and $\eta = 0.1$ and $T_0 = 0.311$ *bottom frame* at time step $t = 5000000$. x-axis is in units of $\Delta x (= 4.0)$. Inset shows close up of c *(top frame)* and ϵ_{xx} *(bottom frame)*.

Table 5.1: Table of Variables and Parameters for Explosive Crystallization PF Simulations

Parameters	Values
Simulation Dimensions N_x	10000
Grid Spacing and time increment Δx, Δt	4.0, 0.00016
mean concentration c	0.05
T_M, L, h, K	1.8,3,10,2000
R/v, $\Delta\epsilon$, K_c	0.025, 10, 0
M_T, Γ, q	2000, 0.02, 1
mismatch η	0, 0.1
T_0	$\sim 0.311 - 0.330$
M_{10}, ξ, M_{c0}	0.165, 5, 1

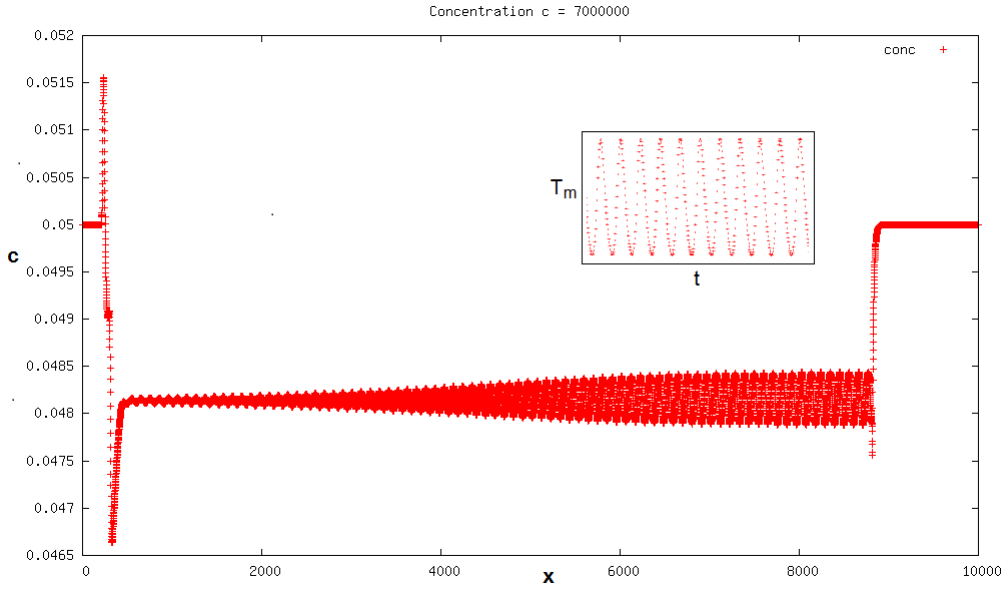

Figure 5.3: Concentration, c, change x resulting from maximum temperature, T_M, oscillation with time, t*(bottom frame)* for $T_0 = 0.317$. Inset - maximum temperature field, T_m as time progresses.

Fig. 5.6. It is noteworthy that even small changes in film temperature can significantly shift the propagating from temperature and, as shown below, concentration and velocity.

Controlling the wavelength of the oscillations is important because of applications to material processing and device manufacturing. The possible oscillation wavelengths for this set of parameters are shown in Table 5.2. The changes in wavelength are modest ($\sim 20\%$) for a given material and change by $\sim 4\%$ between the $\eta = 0$ and $\eta = 1$ runs. However, for futher period doubling, although the distance between successive maxima does not change, the wavelength of the pattern is larger because there are concentration peaks at different heights. Similar trends would exist for fields, such as density, crystallinity, film height [10, 78].

5.4.1 Elucidating the Effect of Mismatch

As stated above, by introducing mismatch between the atoms while keeping the other parameters constant (though the latent heat changes according to Eq. 5.8), the the behaviour of both systems

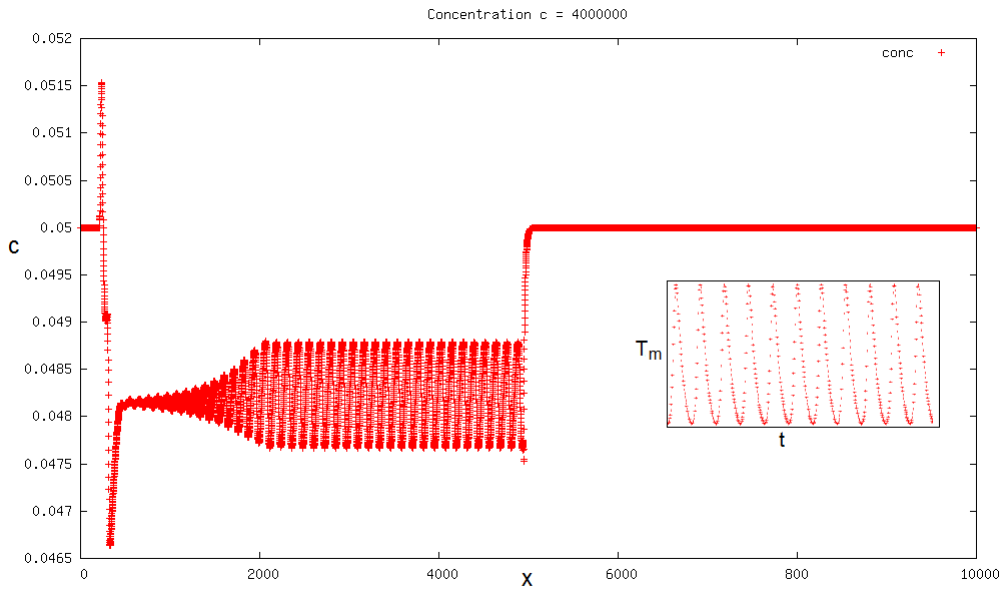

Figure 5.4: Concentration, c, change x resulting from maximum temperature, T_M, oscillation with time, *t(bottom frame)* for $T_0 = 0.316$. Inset - maximum temperature field, T_m as time progresses. Notice how the shape of the oscillations is different from those in Fig.5.3.

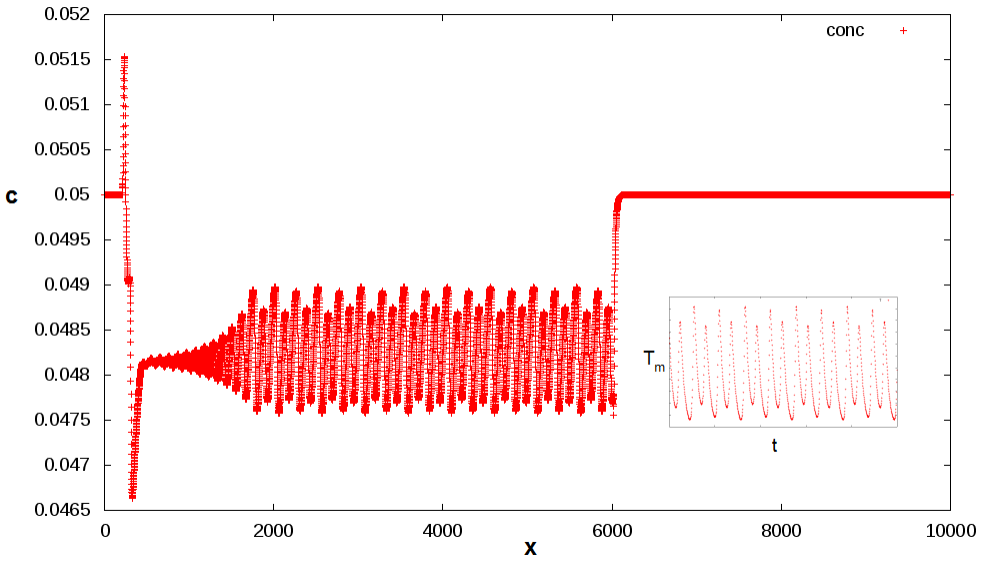

Figure 5.5: Concentration, c, change x resulting from maximum temperature, T_M, oscillation with time, *t(bottom frame)* for $T_0 = 0.31575$. Inset - maximum temperature field, T_m as time progresses. Note that 2 period doublings have occurred in between $T_0 = 0.31575$ and $T_0 = 0.316$ (Fig. 5.4).

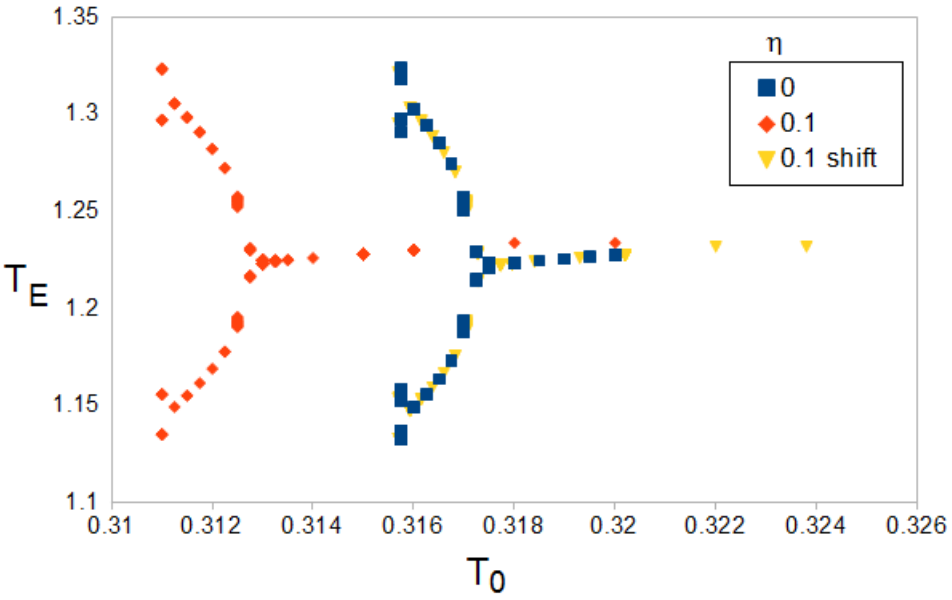

Figure 5.6: Extremal Temperatures, T_E vs. substrate temperatures, T_0, for simulations with *(*(red diamonds)) and without mismatch *(*(blue squares)). Shifted and stretched mismatch curve $((T_0, T_E) \rightarrow (0.9T_0 + 0.0358, T_E - .002))$ *(yellow triangles)* superimposed on no-mismatch curve.

Table 5.2: Table of Wavelengths for Oscillations

η	T_0	Distance between successive maxima	wavelength
0	0.31575	484	1736
0	0.316	484	484
0	0.317	408	408
0.1	0.311	504	1008
0.1	0.31125	480	480
0.1	0.313	392	392

remains qualitative the same as a function of substrate temperature. Fig. 5.6 shows that increasing mismatch shifts the birfucation point to lower substrate temperatures. It is noted that this observed behaviour is opposite to the analytical result performed in section 5.3.4, based on a relatively sharp interface analyis that incorporates a diffuses interface, and which assumes nearly complete solute trapping. That is because in the diffuse interface limit used, there were no low-order to capture the effects of the interfaces that emerge in the simulations. A second-order asymptotic analysis would be required to correct this.

One major difference between the theoretical analysis and the simulations is the dependence of velocity on peak temperature, T^b, as illustrated in Fig. 5.7. When the system is at a uniform temperature ($T^b = T_0 \sim 0.9 - 1.7$), that is, the temperature field is much wider than the interface, velocity relation Eq. 1.30. However, the actual relation of V_{ss} vs. T^b is almost a straight line for the simulations done in section 5.4, as opposed to an the nose-like curve on T^b of Eq. 1.30 ($T_0 \sim 0.31 - 0.8$). The main reason for this difference is that in the simulations only a small portion of the interface has a temperature near T^b, while the rest of the interface is at a much lower temperature, meaning that V is controlled by the speed of the portions of the interface at temperature

significantly less than T^b.

Progress can be made to understand the nature of misfit on oscillations analytically using the non-dimensional parameters parameterizing the stability derived in Ref. [10]. The parameters α and β given by Eqs. 1.37 and 1.38, which define the stability phase space, can be computed in terms of the steady state velocity, V_{ss} from the approximate interface temperature, which differs only by a couple percent from the simulated maximum temperature. The slopes of the lines of best fit in Fig. 5.7 are used to determine $\frac{dV}{dT}$, which also appears in the expression for α. Fig. 5.8 shows the path in (α, β) space of our simulations for different η, and how these cross the spatiality boundary.

5.5 Explosive Crystallization using Full PFC model

The phase field model simulations were also compared to simulations of the full PFC model. Explosive crystallization and the oscillatory patterning were similarly observed in the full PFC model. The free energy equation, Eq. 5.1, uses roughly the same parameters as in Table 5.1, with exceptions: $\Delta x = \pi/4$, which is needed to resolve individual atoms, $\Delta\epsilon = 0.04$, $R/v_M = 0.1$, $M_{c0} = 2000$, $K_c = 0.1$, $\Delta t = 0.001$, and $N_x = 32768$. Only $\eta = 0$ was studied for the full PFC comparison. Also, q, is rescaled by taking into account the magnitude of the order parameter. The order parameter used to describe the phase is the local root mean square density $< n^2 >$, which is obtained by filtering the fourier transform of n^2 by $\exp(-\zeta_n^2 k^2)$, where k is the magnitude of the wave vector of the mode. To ensure that the average density is nearly constant, a large $C(k = 0)$ term is used; that is, $C(k) = C_{PFC}(k) + C_0 \exp(-\zeta_0^2 k^2)$, where $\zeta_0 = \sqrt{12.5}$ and $C_0 = 5000000$. The equations of motion need to be generalized from Eqs. 2.23 and 2.24 to include the variable mobility of the n and c fields:

$$\begin{aligned} \frac{\partial n}{\partial t} &= \nabla \left[M_n(T) \cdot \nabla \left(\tfrac{\delta F_{PFC}}{\delta c} \right) \right] \\ \frac{\partial c}{\partial t} &= \nabla \left[M_c(T, \phi) c \cdot \nabla \left(\tfrac{\delta F_{PFC}}{\delta c} \right) \right] \end{aligned} \tag{5.19}$$

where $M_n(T) = M_0 \exp(-E_a/T)$ and $M_0 = 1.1$. These equations are simulated with a spectral method, using an algorithm in the appendix B. Because the elastic field only varies around the interface, the elastic interactions are short-ranged, meaning that second time derivaties need not be included to relax the elastic fields quickly in Eqs. 5.19. Also, the temperature field is simulated by coupling Eq. 5.5 with the aforementioned substution of ϕ with $< n^2 >$.

PFC simulations were done in 2D, where $N_y = 16$ so that fit a hexagonal lattice could be fit into the simulation window without straining the system. In Figs. 5.9 and 5.10 shows a image from the 2D density, 1D amplitude, 2D temperature and 1D temperature fields from a typical propagating steady state front. It is clear that the full PFC model is consistent in its salient features to the coarse-grained model studied above. We also observed the usual oscillatory solutions and bifurcation sequencing using the full PFC model. A portion of a bifurcation diagram obtained from direct PFC model simulations is shown in Fig. 5.11

5.6 Possible improvements to PF/PFC modelling of Explosive Crystallization

5.6.1 Considering multiple phases

In the above models, the amorphous phase was neglected. The full PFC model behaves very much like a PF model as shown in section 5.5. It can also be used to generate a complex amplitude model that incorporate elastic effects between solid phases and in 2D/3D possible grain boundary

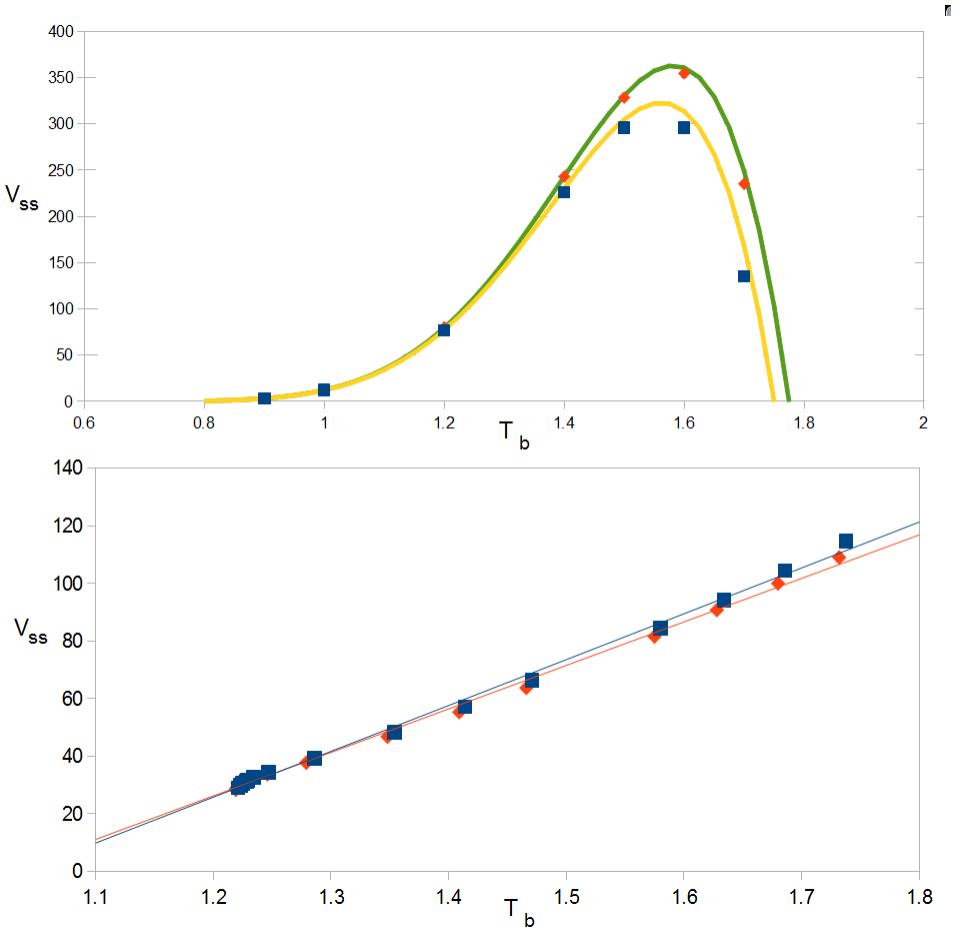

Figure 5.7: Simulations of velocity, V, versus interface temperature, T^b, relation for simulations with mismatch $\eta = 0.1$ *(blue squares)* and without *(red diamonds)*. Simulations in which $T(x) = T^b$ *(top frame)* resemble Eq. 1.30, while simulations with $q = 1$, $M_T = 2000$, $\Gamma = 0.02$, and $T_0 < T^b$ *(bottom frame)* do not. In top frame, reference curves are Eq. 5.17 with $f_l - f_s = L(T_M - T)/T_M$, with $T_M = 1.75$ and $C = 1/4000000$ *(yellow curve)*, $T_M = 1.775$ and $C = 1/4000000$ *(green curve)* and $L = 3$ and $E_a = 12.952$ *(both curves)*. In bottom frame, slope of blue line of best fit is 159 and is 151 for the red line.

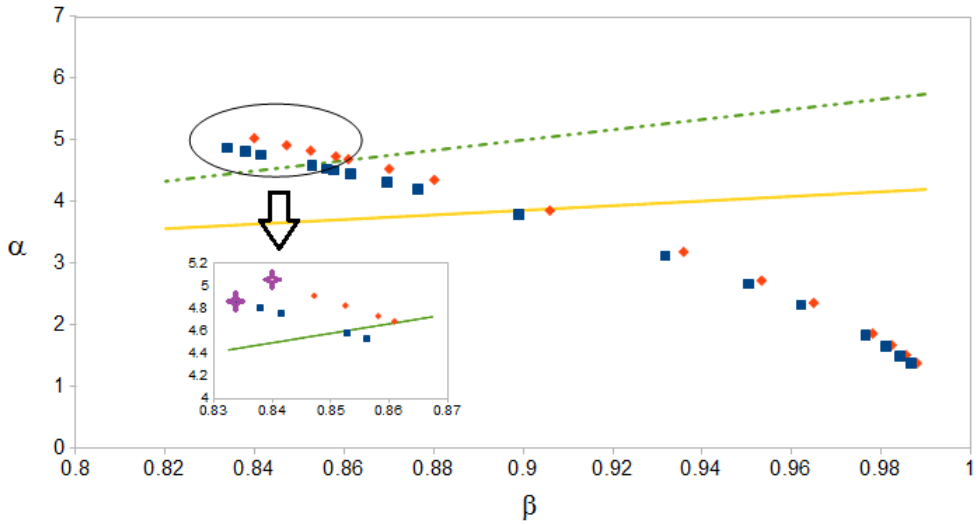

Figure 5.8: Phase space of oscillatory solutions is bounded by $\beta = (\alpha - \alpha^{-1})/4$ *(solid curve)* and $\beta = (\alpha + 1)^2/8\alpha$ *(dashed curve)*. Points represent corresponding simulations for two values of η: $\eta = 0$ *(blue square)* and $\eta = 0.1$ *(red diamond)*. Inset - close up of plots with oscillatory temperature field including those which have undergone period doubling (*stars*).

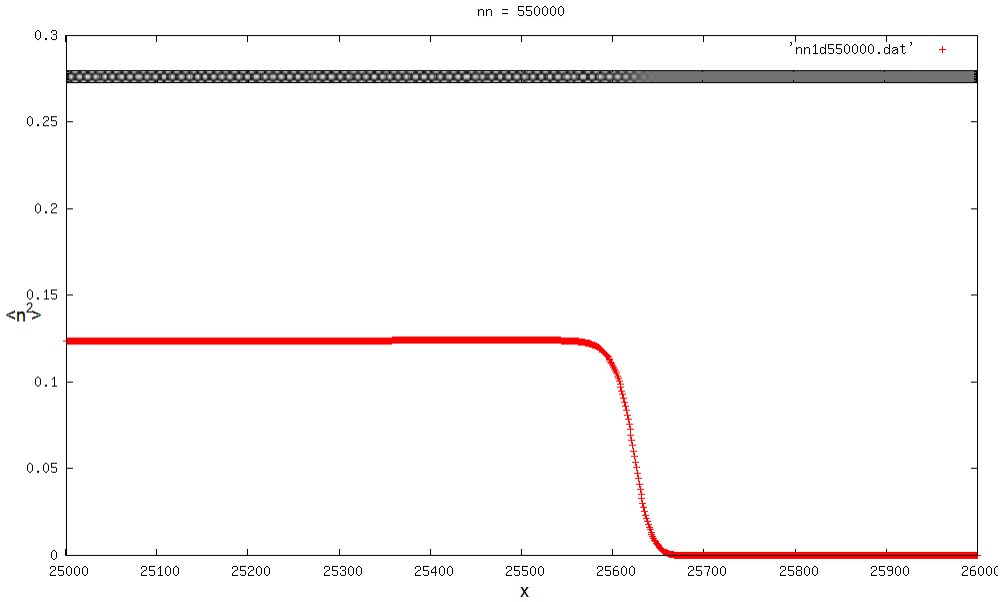

Figure 5.9: Illustration of density Field in 2D (top) and corresponding average phase field, $\phi =< n^2 >$ (bottom).

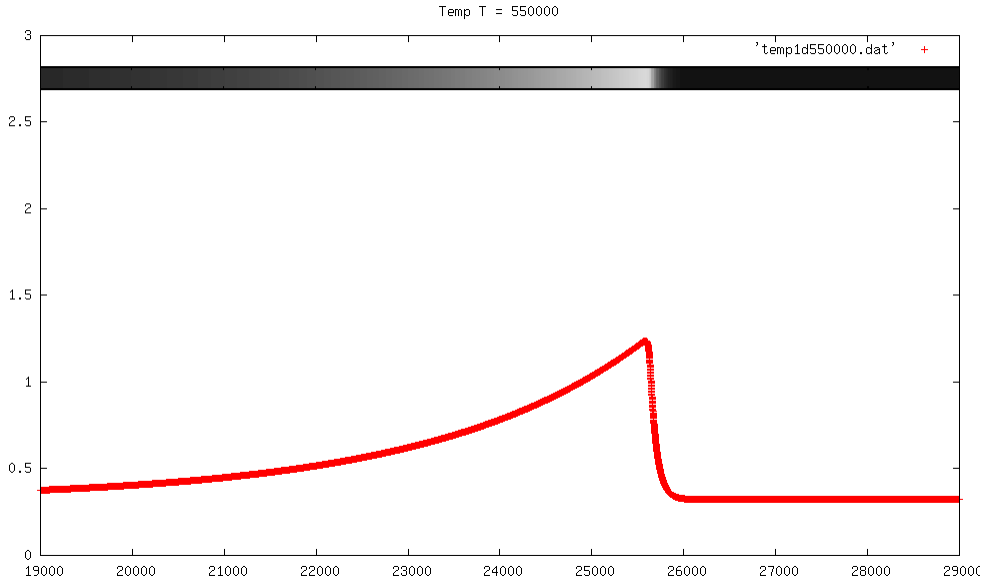

Figure 5.10: Illustration of temperature Field in 2D (top) and corresponding crosssectional average temperature field (bottom).

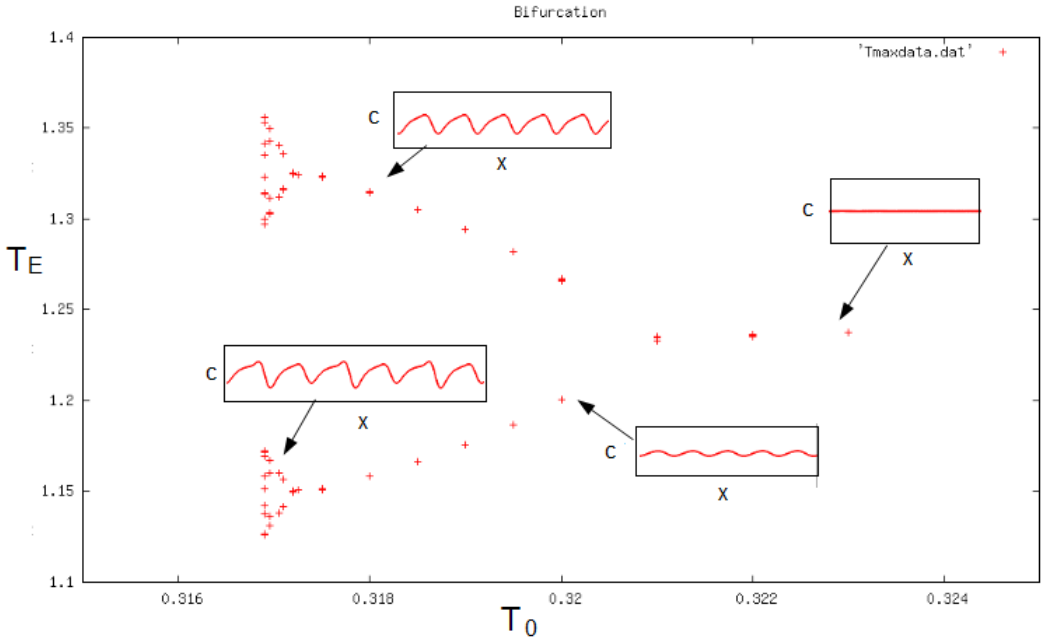

Figure 5.11: Extremal temperature in oscillation cycle, T_E, vs substrate temperature, T_0, for PFC model. Insets showing concentration profile due to oscillation of temperature field.

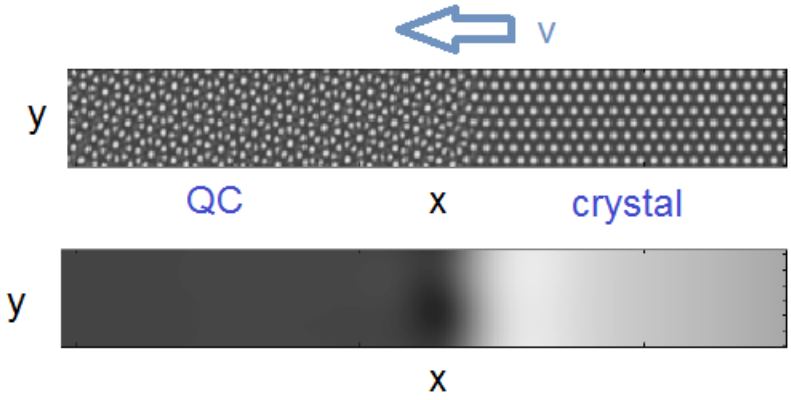

Figure 5.12: Density field *(top frame)* and corresponding temperature field *(bottom frame)* in 2D quasi-crystal with heat source simulation.

effects. However, with a full PFC-type model, it can also be used to elucidate the structure of the crystalline and amorphous phases engaged in crystallization, although it is unclear at present how the structure can be related to changes of temperature within the system. As in the case of Ref. [70], the amorphous material can be treated as a thermodynamic state of the system. By making this assumption, an order parameter can be constructed from some particular property of a crystal structure that is present and the temperature simulation can be modelled phenomenologically as was done in section 5.5. While it is not at present known how to define an amorphous phase in terms of amplitudes, we can illustrate the power of the PFC model by examining a related situation of crystallization of a quasi-crystalline (QC) state [147].

Some preliminary simulations were done using the XPFC model, tuned for a pure material with a QC and hexagonal crystal phase; that is, two families of peaks of the correlation function were kept with $q_2 = 0.5(1+\sqrt{5})q_1$ [147]. One slight difference in Eqs. 2.31 when using a typical XPFC model, is that the equations were linearized about $\sigma^2 = \sigma_0^2$. Thus, in Eq. 5.5, σ^2 replaces T and ϕ is replaced by a local $< n^2 > - < n_{QC}^2 >$. The solid mobility was kept costant, as the simulations were done to simply check mechanical effects from the interaction of the crystal and QC phases. A snapshot of a crystalline-quasicrystal from showing the temperature field and density field are shown in Fig. 5.12.

The QC state transforms into the crystalline state around regions of elevated temperature. Elastic softening might allow atoms to rearrange themselves. Also, the interface motion is jerky, which might be better described as the interface moving in stick-slip motion. It can even stop, thereby extinguishing the elevated temperature at the interface, which means that the reaction will not proceed further, unless the configuration is mechanically unstable in which case atoms will rearrange themselves, thereby restarting the reaction. These simple examples show that there is still work to be done to use the full power of the PFC approach to examine interface and defects on the crystallization of unstable phases.

5.6.2 Extension to Larger length scales

To study the effect of a diffuse interface, explosive crystallization can be studied in a pure material by simulating temperature fields of different widths. To simulate a pure material, Eqs. 5.4 and 5.5 are simulated while ignoring the concentration equation and setting $c = 0$. As well for all strain fields, $U_{ij} = 0$. Some premliminary simulations were done in which the width of the diffusion field was altered by changing M_T and Γ while keeping their product constant; M_T was varied from 20 to 2000; the timestep, Δt, needed to be controlled in proportion to this. The simluation parameters

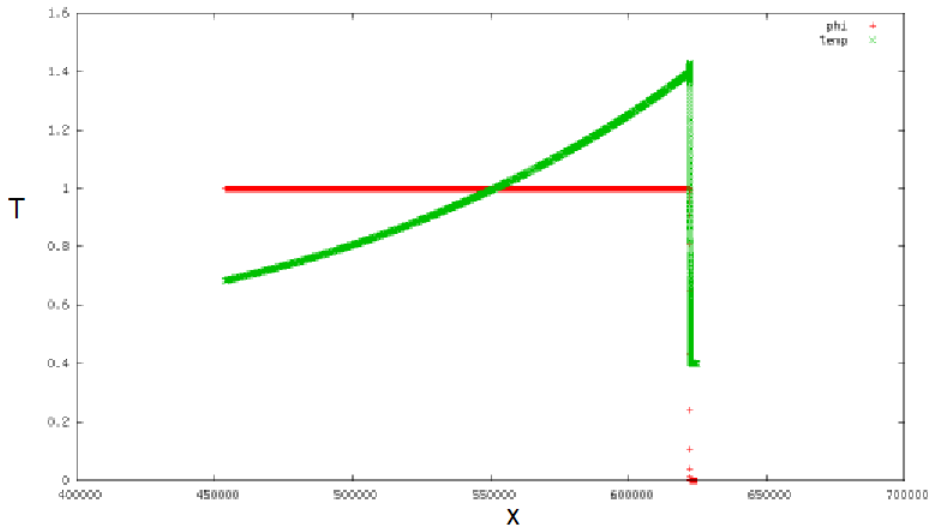

Figure 5.13: Phase field *(red crosses)* and temperature field *(green crosses)* in PF adaptive mesh simulation with $M_T = 2000$, $\Gamma = 0.0002$, and $T_0 = 0.395$.

constant throughout the runs are: $M_{10} = 0.165$, $E_a = 12.952$, $q = 1$, , $K = 4$ and $h = 1$.

As well, to fit the wide temperature diffusion field in the simulation, a variable-mesh comoving grid was used for the larger simulation sizes. This grid shfited by $1/8^{th}$ of the number of grid points whenever the phase field at $x = 7/8N_x$ became greater than $1/2$. Also, the grid spacing Δx was periodically doubled behind $5/8^{th}$ of the size of the grid as necessary to fit the diffusion tail. A snapshot of a simulation with $M_T = 10000$ is shown in Fig. 5.13. It should be noted that the simulated diffusion tail is $\sim O(100)$ times larger than those in Fig. 5.2.

As M_T was increased, a higher substrate temperature, T_0, was needed to to observe the propagation of the reaction front. Similarly, the oscillations could only be observed at higher substrate temperatures, though the trend has not been accurately quantified. These considerations can also be important for studying classically-sized systems with adaptive meshes, while keeping PFC-based parameters, so that links to the atomic properties can be made. That being said, the current model, studied in section 5.4, can be good for studying patterning with explosive crystallization at much smaller scales, if materials with suitable properties can be developed.

Chapter 6

Conclusions and Future Directions

In this dissertation, it was shown how the phase field crystal formalism can be used effectively to simulate elastic effects in systems in which interfacial physics is important because of the time and lengths scales involved in such problems. This formalism was applied to the examination of grain boundary thermodynamics in alloys, as well as cluster formation and explosive crystallization. The work found in this dissertation is another example demonstrating the robustness of the PFC-formalism.

Both PFC and XPFC models were shown to give physically-consistent descriptions of interfacial physics. For example, the Read-Shockley relation and Gibbs adsorption theorem was obeyed in PFC and XPFC alloys. With the PFC-type models, the effects of undercooling, average system concentration, attraction between different atomic species, and mismatch were elucidated by running different simulations and deriving an semi-empirical relation based on an Read Shockley theory. It was also discovered that the main effect on grain boundary energy in the traditional PFC model is undercooling, while the effect of solute segregation was rather small. In the XPFC model, the solute segregation had a larger and direct effect. Regarding premelting behaviour, it was discovered that the extension to alloys from previous pure material studies with PFC models was straightforward. Also, it was shown analytically that the addition of solute helps make the grain boundary more attractive. Furthermore, a possible mechanism for hysteresis in the premelting transition was identified in alloys.

The work on grain boundary thermodynamics and premelting can be extended by using coarse-graining procedures to connect the results of this study to larger scale models. This work can be extended in future PFC studies to grain boundary thermodynamics in multi-component systems. As well, the thermodynamic studies can be replaced by kinetic studies to determine more realstic properties of grain boundary thermodynamics and premelting in alloys because materials can be processed far from equilibrium in practical situations.

In terms of studying cluster formation, the XPFC formalism was used to elucidate the poorly understood mechanism of dislocation-facilitated precipitation in Al alloys. In particular, local strain was shown to stabilize these structures. With the XPFC model that takes into account bulk, surface, and dislocation effects, many of the qualitative features of the clustering process were predicted. The main effect of adding a third component was decreasing the local free energy increase in the system, thereby making it easier to form a cluster. Also, clustering in ternary materials appears to happen with a two step process in which the larger minority species moves to the dislocation along with the smaller solute species so that strain effects are lessened and once the cluster is big enough, the less prevalent minority species is expelled from the cluster.

There are a few directions on this topic that can be taken in the future. Some of the more straightforward are comparing with newer experimental studies and studying the effect of new components. Already in Ref. [64], the XPFC models mentioned in this dissertation have been extended to 3D. As

well, the 3D simulation results were compared to experiments done within the same research group in [64]. Also, other PFC-types models, such as the vacancy PFC (VPFC) model can be used to study the effects of vacancies and not just dislocations on this process.

Finally, the phase field crystal phenomenology was used to simulate explosive crystallization. The PFC formalism was connected to a PF model, which can be related to the reaction-diffusion model of Ref. [11] and to sharp-interface models of the phenomenon (e.g., Ref. [10]). The PF and PFC models can both exhibit the commonly found undulations in the temperature field. The paradigm was extended to binary alloys, which were simulated with both PF and PFC methods and were shown to leave periodic solute traces when temperature oscillations occurred. Such patterning can be applied to device manufacturing in the semi-conductor industry. The main new result of this chapter was to elucidate the role of atomic mismatch in the oscillation of the solute patterning of thin film alloys, as a function of substrate temperature.

Future PFC and PF-type models can be used to study explosive crystallization with adaptive meshes and coarse-graining approaches, which can inform the parameterizations used in larger-scale models. Also, various XPFC and VPFC type models can be used to study the phase transformation mechanisms on a smaller scale to directly determine the interactions between two different solid phases as explosive crystallization occurs.

Appendix A

An Alternate Method for Deriving Correlation Term in Amplitude Model

Obtaining a rotationally invariant amplitude model expansion of a specific free energy functional or dynamics equations in a number of conventional methods can be quite tedious as noted in [13]. However, there is a convenient short cut to obtain the appropriate derivative terms. This technique can be used for any isotropic pair correlation function, $C(r-r')$, provided a Taylor-expansion of the fourier transform of second-order correlation function, $\hat{C}(k)$ can be found in real-space, which is true for a large number of well-behaved functions. It involves writing $\hat{C}(k)$ as a Taylor expansion with respect to k^2, which is discussed in [12]. The work in this section was included in [13]

To start off with, consider how to write $\int(d\vec{\rho}C(r-\rho)n(\vec{\rho}))$ as a functional Taylor series. The Taylor expansion is done about $k^2=0$ (though any convenient wavenumber can be picked; this fact will be useful to note later on for the shortcut to this method).

$$\begin{aligned} C_2n(r) &\equiv \int(d\vec{\rho}c(r-\rho)n(\vec{\rho})) = \frac{1}{\sqrt{2\pi}}\int\int(d\vec{\rho}d\vec{k}\hat{C}(k)\exp(I\vec{k}\cdot(\vec{r}-\vec{\rho}))n(\vec{\rho})) \\ &= \frac{1}{\sqrt{2\pi}}\int d\vec{k}\hat{C}(k)\exp(I\vec{k}\cdot\vec{r})\hat{n}(\vec{k}) \\ &= \frac{1}{\sqrt{2\pi}}\int d\vec{k}\sum_l\frac{1}{l!}\left(\frac{\partial^l\hat{C}(k)}{\partial(k^2)^l}\right)_{k^2=0}(k^2)^l\exp(I\vec{k}\cdot\vec{r})\hat{n}(\vec{k}) \\ &= \sum_l\frac{1}{l!}\left(\frac{\partial^l\hat{C}(k)}{\partial(k^2)^l}\right)_{k^2=0}(-\nabla^2)^ln(\vec{r}) = C(\nabla^2)n(\vec{r}) \end{aligned} \tag{A.1}$$

Note that $I=\sqrt{-1}$. Although the above expansion can be used in either in the free energy functional or in the dynamics equations, the process is illustrated by substituting Eq.(A.1) into the dynamics equations and expanding the density as $n=\sum_m A_m\exp(I\vec{k}_m\cdot\vec{r})$. As in [148], note that the Laplacian operator maps to the following expression $\nabla^2\rightarrow-|k_j|^2+2I\vec{k}_j\cdot\nabla+\nabla^2\approx-|q_j|^2$ when operators containing Laplacians act on $A_l\exp(I\vec{k_l}\cdot\vec{r})$ (provided the $k=0$ mode is not being considered, in which case ∇^2 remains the same).

$$\frac{\partial n}{\partial t}=\nabla^2\left(C(\nabla^2)n+\frac{\partial f}{\partial n}\right)$$

$$\sum_l \frac{\partial A_l}{\partial t}\exp(I\vec{k}_l\cdot\vec{r}) \approx \sum_l(-|k_l|^2)\left(\frac{\partial f}{\partial A_l^\dagger}\exp(I\vec{k}_l\cdot\vec{r}) + C(\nabla^2)A_l\exp(I\vec{k}_l\cdot\vec{r})\right)$$

$$\sum_l \frac{\partial A_l}{\partial t}\exp(I\vec{k}_l\cdot\vec{r}) = \sum_l(-|k_l|^2)\times$$

$$\left(\frac{\partial f}{\partial A_l^\dagger}\exp(I\vec{k}_l\cdot\vec{r}) + \exp(I\vec{k}_l\cdot\vec{r})C(\nabla^2 + 2I\vec{k}_l\cdot\nabla - |k_l|^2)A_l\right) \quad \text{(A.2)}$$

where † respresents complex conjugate. To write the dynamics equations for the any Fourier component, the projection method found in [148] is applied:

$$\mathbf{P}_m\sum_l \frac{\partial A_l}{\partial t}\exp(I\vec{k}_l\cdot\vec{r}) =$$

$$\mathbf{P}_m\sum_l(-|k_l|^2)\left(\frac{\partial f}{\partial A_l^\dagger}\exp(I\vec{k}_l\cdot\vec{r}) + \exp(I\vec{k}_l\cdot\vec{r})C(\nabla^2 + 2I\vec{k}_l\cdot\nabla - |k_l|^2)\sum_l A_l\right)$$

$$\frac{\partial A_m}{\partial t} = (-|k_m|^2)\left(\frac{\partial f}{\partial A_l^\dagger} + C(\nabla^2 + 2I\vec{k}_m\cdot\nabla - |k_m|^2)A_m\right) \quad \text{(A.3)}$$

where projection, $\mathbf{P_m}$, is the following operation over a unit cell (size V), centred at point $\vec{\rho}$:

$$\mathbf{P}_m = \frac{1}{V}\int_V d\vec{r}\exp(-I\vec{k}_m\cdot\vec{r}) \quad \text{(A.4)}$$

$C(\nabla^2 + 2I\vec{k_m}\cdot\nabla - |k_m|^2)A_m$ can be written by by Taylor expanding the correlation function, as was done to derive A.1, noting that $\nabla^2 \to -|k_j|^2 + 2I\vec{k}_j\cdot\nabla + \nabla^2$:

$$C(\nabla^2 + 2I\vec{q}_m\cdot\nabla - |q_m|^2)A_m = \sum_{l=0}^{\infty}\frac{1}{l!}\left(\frac{\partial^l\hat{C}(k)}{\partial(k^2)^l}\right)_{k^2=0}(-\nabla^2 - 2I\vec{q}_m\cdot\nabla + |q_m|^2)^l A_m$$

$$= \sum_{l=0}^{\infty}\frac{1}{l!}\frac{\partial^l\hat{C}(k)}{\partial(k^2)^l}|q_m|^{2l}A_m - (2I\vec{q}_m\cdot\nabla + \nabla^2)\sum_{l=0}^{\infty}\frac{l+1}{(l+1)!}\frac{\partial^l\partial\hat{C}(k)}{\partial(k^2)^{l+1}}|q_m|^{2l}A_m$$

$$+(2I\vec{k}_m\cdot\nabla + \nabla^2)^2\sum_{l=0}^{\infty}\frac{(l+2)(l+1)}{l!2}\frac{\partial^{l+2}\hat{C}(k)}{\partial(k^2)^{l+2}}|q_m|^{2l}A_m + ...$$

$$= \sum_{p=0}^{\infty}\sum_{l=0}^{\infty}\left[(-2I\vec{q}_m\cdot\nabla - \nabla^2)^p\frac{1}{p!l!}\left(\frac{\partial^l}{\partial(k^2)^l}\frac{\partial^p\hat{C}}{\partial(k^2)^p}\right)_{k^2=0}|q_m|^{2l}A_m\right]$$

$$= \sum_{p=0}^{\infty}\left[(-2I\vec{q}_m\cdot\nabla - \nabla^2)^p\frac{1}{p!}\left(\frac{\partial^p\hat{C}}{\partial(k^2)^p}\right)_{k^2=q_m^2}A_m\right] \quad \text{(A.5)}$$

Finally, noting that the right hand side of A.3 $-|q_m|^2\frac{\delta F}{\delta A_m^\dagger}$ to obtain the free energy in terms of each of the amplitudes A_l, $\frac{\delta F}{\delta A_m^\dagger}$ needs to be integrated for each component to get an appropriate functional integral. Free energy term corresponding to the correlation function is:

$$F_{corr} = -\frac{1}{2}\int d\vec{r}\sum_m A_m^\dagger C(\nabla^2)A_m$$

$$= -\frac{1}{2}\int d\vec{r}\sum_m A_m^\dagger \sum_{p=0}^{\infty}\left[(-2I\vec{q}_m\cdot\nabla-\nabla^2)^p\frac{1}{p!}\left(\frac{\partial^p\hat{C}}{\partial(k^2)^p}\right)_{k^2=q_m^2}\right]A_m$$

$$\approx -\frac{1}{2}\int d\vec{r}\sum_m A_m^\dagger(\hat{C}(q_m^2))A_m + \frac{1}{2}\sum_m A_m^\dagger\left[(2I\vec{q}_m\cdot\nabla+\nabla^2)\left(\frac{\partial\hat{C}}{\partial(k^2)}\right)_{k^2=q_m^2}\right]A_m$$

$$-\frac{1}{4}\sum_m A_m^\dagger\left[(-4(\vec{q}_m\cdot\nabla)^2-4I\vec{q}_m\cdot\nabla\nabla^2+\nabla^4)\left(\frac{\partial^2\hat{C}}{\partial(k^2)^2}\right)_{k^2=q_m^2}\right]A_m \quad \text{(A.6)}$$

where just consider the energy up to the 2nd term in the sum is considered.

A.1 Short Cut Method

The short cut requires noting that for each amplitude A_m, the correlation function should be expanded about $k^2 = |q_m|^2$. In doing this, the Taylor expansion in Eq.(A.5) becomes:

$$C(\nabla^2+2I\vec{q}_m\cdot\nabla-|q_m|^2)A_m =$$
$$\sum_{l=0}^{\infty}\frac{1}{l!}\left(\frac{\partial^l\hat{C}(k)}{\partial(k^2)^l}\right)_{k^2=|q_m|^2}(-\nabla^2-2I\vec{q}_m\cdot\nabla+|q_m|^2-|q_m|^2)^lA_m$$

which is identical to the final result of Eq. (A.5).

Lead up to Short Cut Method in Energy Formalism

In this case, let us consider each term with respect to its contriubtion on the free energy. Let us substitute $n_=n_0+\sum_j A_j\exp(-I\vec{k}_j\cdot\vec{r})$ into equation (A.1) and look at each component, using the relations established above, relating Laplacians and derivatives of the correlation function in k-space:

$$C(\nabla^2)\left(n_0+\sum_j A_j\exp(-I\vec{k}_j\cdot\vec{r})\right) = C(\nabla^2)n_0 + C(\nabla^2)\sum_j A_j\exp(-I\vec{k}_j\cdot\vec{r})$$

For n_0:

$$\begin{aligned} C(\nabla^2)n_0 &= \textstyle\sum_{l=0}^{\infty}\frac{1}{l!}\left(\frac{\partial^l\hat{C}(k)}{\partial(k^2)^l}\right)_{k^2=0}(-\nabla^2)^ln_0 \\ &\approx (C(k=0)-\left(\frac{\partial^l\hat{C}(k)}{\partial(k^2)^l}\right)_{k^2=0}\nabla^2)n_0 \end{aligned}$$

Now, let us look at any arbitrary (m^{th}) mode (using the identity $C(\nabla^2)A_m\exp(I\vec{k_m}\cdot\vec{r}) = \exp(I\vec{k_m}\cdot\vec{r})C(\nabla^2+2I\vec{k}_m\nabla-|\vec{k}_m|^2)A_m$):

$$\begin{aligned} C(\nabla^2)(A_m) &= \exp(I\vec{k_m}\cdot\vec{r})C(\nabla^2+2I\vec{k}_m\nabla-|\vec{k}_m|^2)(A_m) \\ &= \exp(I\vec{k_m}\cdot\vec{r})\sum_{l=0}^{\infty}\frac{1}{l!}\left(\frac{\partial^l\hat{C}(k)}{\partial(k^2)^l}\right)_{k^2=0}(-\nabla^2-2I\vec{q}_m\cdot\nabla+|k_m|^2)^lA_m \end{aligned}$$

The above terms relate to the excess term in the free energy $nC(\nabla^2)n$. Let us coarse-grain this term, assuming n_0 an A_j are slowly varying. For n_0:

$$\frac{1}{V}\int_{unitcell}(n_0+\sum_j A_j\exp(I\vec{k}_j\cdot\vec{r}))C(\nabla^2)n_0 d\vec{r} = n_0C(\nabla^2)n_0$$
$$\approx n_0(C(k=0)-\left(\frac{\partial^l\hat{C}(k)}{\partial(k^2)^l}\right)_{k^2=0}\nabla^2)n_0 \tag{A.7}$$

Note that any $\int\exp(I\vec{k}_j\cdot\vec{r})n_0d\vec{r}$ term integrates to zero over the unit cell. For any A_m:

$$\frac{1}{V}\int_{unitcell}(n_0+\sum_j A_j\exp(I\vec{k}_j\cdot\vec{r}))C(\nabla^2+2I\vec{k}_m\nabla-4|\vec{k}_m|^2)A_m d\vec{r}$$
$$= A_{-m}C(\nabla^2+2I\vec{k}_m\nabla-4|\vec{k}_m|^2)A_m$$
$$= A_{-m}\sum_{l=0}^{\infty}\frac{1}{l!}\left(\frac{\partial^l\hat{C}(k)}{\partial(k^2)^l}\right)_{k^2=0}(-\nabla^2-2I\vec{k}_m\cdot\nabla+|k_m|^2)^lA_m \tag{A.8}$$

Also noting that $\int\exp(I\vec{k}_j\cdot\vec{r})\exp(I\vec{k}_m\cdot\vec{r})d\vec{r}$ term integrates to zero over the unit cell if $j\neq -m$. Eq. A.7 mathematically looks like Eq. A.8 (if truncated at the second term). This equality holds if all terms are kept. Furthermore, all manipulations on A.8 do not change this equivalence.

The next point is to demonstrate that each of the excess terms can be obtained by expanding the correlation function about the peak corresponding to the wavenumber of each mode. To do this, Eq. A.5 can be used, which gives the result right away.

A.2 Equivalence with Other PFC Expansions

As noted in [13], To demonstrate that Eq.(A.10) is identical to the correlation term in the previous sections, we simply apply chain rule to all $\partial^l_{k^2}C(k)$ taking them with respect to k instead of k^2:

$$\partial^l_{k^2}C(k) = (\frac{1}{2k}\partial^2_k)^lC(k) \tag{A.9}$$

noting that $\frac{\partial k}{\partial k^2}=\frac{1}{2k}$. Substituting the above equation into 2nd order expansion in Eq.(A.10) gives:

$$F_{corr} = -\frac{1}{2}\int d\vec{r}\sum_m A^\dagger_m(\hat{C}(q^2_m))A_m - \frac{1}{2}\sum_m A^\dagger_m\times$$
$$\left[(2I\vec{q}_m\cdot\nabla+\nabla^2)\left(\frac{1}{2k}\frac{\partial\hat{C}}{\partial(k)}\right)_{k=|q_m|}\right]A_m - \frac{1}{4}\sum_m A^\dagger_m\times$$
$$\left[(-4(\vec{q}_m\cdot\nabla)^2-4I\vec{q}_m\cdot\nabla\nabla^2+\nabla^4)\frac{1}{4k^2}\left(\frac{\partial^2\hat{C}}{\partial k^2}-\frac{1}{k}\frac{\partial\hat{C}}{\partial k}\right)_{k^2=q^2_m}\right]A_m \tag{A.10}$$

Appendix B

Numerical Method for Variable Mobility

B.1 Alternate form for diffusive dynamics

If a field, f, is governed by conserved dissipative dynamics, it obeys the following equation:

$$\frac{\partial f}{\partial t} = \nabla \cdot (M \nabla \mu_f) \tag{B.1}$$

where μ_f the chemical (diffusion) potential [65] and M is the mobility [65, 67]. If M depends on position (for example, by being dependent on another field), the above equation can be rewritten as:

$$\frac{\partial f}{\partial t} = M \nabla^2 \mu_f + (\nabla M) \cdot (\nabla \mu_f) \tag{B.2}$$

Noting that

$$2(\nabla M) \cdot (\nabla \mu_f) = \nabla^2 (M \mu_f) - \mu_f \nabla^2 M - M \nabla^2 \mu_f \tag{B.3}$$

makes

$$\frac{\partial f}{\partial t} = \frac{1}{2} \left(\nabla^2 (M \mu_f) + M \nabla^2 \mu_f - \mu_f \nabla^2 M \right) \tag{B.4}$$

When considering variable mobility, it can be decomposed into a constant part, M_0, and a variable part δM:

$$M = M_0 + \delta M \tag{B.5}$$

Substituting this into Eq. B.4 gives

$$\frac{\partial f}{\partial t} = M_0 \nabla^2 (\mu_f) + \frac{1}{2} \left(\nabla^2 (\delta M \mu_f) + \delta M \nabla^2 \mu_f - \mu_f \nabla^2 \delta M \right) \tag{B.6}$$

B.2 Numerical Method

In this section, a numerical method for sovling Eq. B.6 is outlined. Following the spectral technique elaborated on in Refs. [1, 38], Eq. B.6 can be rewritten in a discretized form and rearranged to solve for the Fourier component, k, of the field at the next timestep f_k^{t+1} from the data at the inital

timestep, t, as:

$$f_k^{t+1} = \exp(-M_0 k^2 L_k \Delta t) f_k^t + \frac{\exp(-M_0 k^2 L_k \Delta t) - 1}{M_0 k^2 L_k} N_k^t \tag{B.7}$$

where N_k^t is the fourier transform of the sum of the nonlinear terms in $M_0 \nabla^2 (\mu_f)$ along with along terms dependent on the variable mobility and L_k consists of the coefficients multiplying f_k and Δt is the timestep size. Another semi-implicit scheme can be obtained by Taylor-expanding the exponent terms and evaluating some of the linear terms at the $t + 1$ time step to give a method similar to the one found in Ref. [149]:

$$f_k^{t+1} = \frac{1}{1 + M_0 k^2 L_k \Delta t} \left(f_k^t + \Delta t N_k^t \right) \tag{B.8}$$

Similarly, variable temperature in PFC simulations can be simulated in a similar way by expanding variable relating into the temperature field, B^L, as $B^L(\vec{r}) = B_0^L + \delta B^L(\vec{r})$, where B_0^L is a constant and δB^L is variable. As a rule of thumb, the technique works well as long as the linear terms are as large as or larger than the nonlinear terms; for variable mobility simulations this is usually true when $\delta M < M_0$.

Appendix C

Stability Analysis of Explosive Crystallization Reaction Front

In this section, the stability analysis done in [10] is repeated. To simulate explosive crystallization in a pure material, the following equation is considered for the temperature, T, of the planar crystallization front in a co-moving reference frame moving at velocity V:

$$\frac{\partial T}{\partial t} = M_T \frac{\partial^2 T}{\partial x^2} + V\frac{\partial T}{\partial x} - \Gamma(T - T_0) + qV\delta(x) \tag{C.1}$$

where M_T is the thermal diffusivity of the substance (in my simulations, simplified to be the same in both phases, though I think the analysis does not require this), T_0 is the substrate temperature, Γ accounts for heat losses, $q = \frac{L}{\rho C}$, where L is the latent heat, C is the specific heat capacity of the substance, and ρ is the density of the substance.

C.1 Steady-State

For a steady state solution, we set $\frac{\partial T}{\partial t} = 0$. Simplify substituting a sample solution $T(x) = \Delta T \exp(\lambda x) + T_0$ into the above equation gives the following equation for λ:

$$\begin{aligned} 0 &= M_T\lambda^2 + V\lambda - \Gamma \\ \lambda &= \frac{-V \pm \sqrt{V^2 - 4M_T\Gamma}}{2M_T} \end{aligned} \tag{C.2}$$

Note that the boundary conditions at $\pm\infty$ are $T = T_0$, which means that

$$\lambda = \frac{-V + \sqrt{V^2 + 4M_T\Gamma}}{2M_T}, x < 0 \tag{C.3}$$

$$\lambda = \frac{-V - \sqrt{V^2 + 4M_T\Gamma}}{2M_T}, x > 0 \tag{C.4}$$

Integrating an infinitesimal distance around the delta function in the temperature equation gives the following boundary condition at x=0 :

$$0 = \left(M_T \frac{\partial T}{\partial x}\right)_{x=0-}^{x=0+} + qV \tag{C.5}$$

From by substituting in $T = T_0 + \Delta T \exp(\lambda x)$, the following solution for the steady state velocity ($V = V_{ss}$) in terms of $T(x = 0) = T_b$ is gotten:

$$\begin{aligned} 0 &= M_T \Delta T \frac{-V - \sqrt{V^2 + 4M_T\Gamma}}{2M_T} - M_T \Delta T \frac{-V + \sqrt{V^2 + 4M_T\Gamma}}{2M_T} + qV \\ qV &= \Delta T \sqrt{V^2 + 4M_T\Gamma} \\ (qV)^2 &= \Delta T^2 V^2 + 4M_T\Gamma\Delta T^2 \\ V^2\left(\frac{q^2}{\Delta T_b^2} - 1\right) &= 4M_T\Gamma \\ V_{ss} &= \frac{2\sqrt{M_T\Gamma}}{\sqrt{\left(\frac{q^2}{\Delta T_b^2} - 1\right)}} \end{aligned} \tag{C.6}$$

Combining this condition with Eq. 1.30 allows for both the steady state velocity and boundary temperature to be solved for.

C.2 Detecting Unstable solutions — finding the bifurcation point

Next, we search for the conditions under which the bifurcation happens. Consider what happens when the interface is perturbed slightly (note the slight change in notation with $T_b \to T^b$). Let $T^b(t) = T_s s^b + \epsilon \exp(2\omega t/\tau_m)$ and $V(t) = V_s s + \epsilon V' \exp(2\omega t/\tau_m)$ where $V' = \frac{dV}{dT^b}$ and $\tau_m = \frac{2}{\Gamma + V_{ss}^2/(4M_T)}$ Substituting the above equations into the definition of x (or rather implicitly defining a time variable τ through the position coordinate) to linearize the equation gives:

$$\begin{aligned} x &= -\int_{t-\tau}^{t} dt' V(T^b(t')) \\ -V_{ss}\tau &= -\int_{t-\tau}^{t} dt' V_s s + \epsilon V' \exp(2\omega t'/\tau_m) \\ -V_{ss}\tau &= V_{ss}(\tau) - \left(\frac{\epsilon V' \tau_m \exp(2\omega t'/\tau_m)}{2\omega}\right)_{t-\tau}^{t} \\ -V_{ss}\tau &= V_{ss}(\tau) - \frac{\epsilon V' \tau_m \exp(2\omega t/\tau_m)}{2\omega}(1 - \exp(2\omega - \tau/\tau_m)) \end{aligned} \tag{C.7}$$

The τ on both sides of the equation are not quite the same, so the difference will be denoted as $\delta\tau$:

$$\delta\tau = \frac{-\epsilon V' \tau_m \exp(2\omega t/\tau_m)}{2\omega V_{ss}}(1 - \exp(2\omega x/(\tau_m V_{ss}))) \tag{C.8}$$

Next, we need to linearize the Green's function (note that I should derive this), by substituting the linearized forms of V and T into the following equation:

$$\begin{aligned} \Delta T^b(t) = q\int_{-\infty}^{0} dx (4\pi M_T\tau)^{-1/2} \exp(-\Gamma\tau - x^2/(4M_T\tau)) \\ + \int_{-\infty}^{\infty} dx (4\pi M_T\tau)^{-1/2} \exp\left(-\Gamma t - \left(x - \int_0^t V(t')dt'\right)^2/(4M_T t)\right) \Delta T(x,0) \end{aligned} \tag{C.9}$$

where $\Delta T = T - T_0$. Far from the starting time, the effect of the initial temperature distribution is negligible; in fact the effect decays as $t^{-1/2}\exp(-2t/\tau_m)$. Therefore the second term is dropped in

the above expression. Linearized solutions with $Re(\omega) > -1$ are sought because they will persist longer than the transient solutions. Note that ϵ and therefore $\delta\tau$ is small, so that all second order and higher terms in $\delta\tau$ can be dropped:

$$\begin{aligned}
\Delta T^b(t) &= q\int_{-\infty}^{0} dx(4\pi M_T\tau)^{-1/2}\exp(-\Gamma\tau - x^2/(4M_T\tau)) \\
\Delta T_{ss} + \epsilon\exp(2\omega t/\tau_m) &= q\int_{-\infty}^{0} dx(4\pi M_T\tau_{ss})^{-1/2}\left(1-\frac{\delta\tau}{2\tau_{ss}}\right)\exp\left(-\frac{\Gamma\tau_{ss}-x^2}{4M_T\tau_{ss}}\right) \\
&\left(1-\delta\tau\left(\Gamma-\frac{x^2}{4M_T\tau_{ss}^2}\right)\right) \\
\epsilon\exp(2\omega t/\tau_m) &= q\int_{-\infty}^{0} dx(4\pi M_T\tau_{ss})^{-1/2}\exp(-\Gamma\tau_{ss} - x^2/(4M_T\tau_{ss})) \\
&\left(-\delta\tau\left(\Gamma+\frac{x^2}{4M_T\tau^2}-\frac{\delta\tau}{2\tau_{ss}}\right)\right)
\end{aligned} \tag{C.10}$$

Now an expression for $\delta\tau$ is substituted in and the following changes of variables are made $\tau_{ss} = -x/V_{ss}$ and $x = \frac{-yV_{ss}\tau_m}{2}$ as was done in Ref. [10]:

$$\begin{aligned}
\epsilon\exp(2\omega t/\tau_m) &= \frac{q\epsilon V'\exp(2\omega t/\tau_m)}{2\omega(2\pi M_T\tau_m)^{1/2}}\times \\
\int_0^\infty dy\,(1-\exp(-\omega y))\,\frac{1}{y^{3/2}}\exp(-y)&\left(\frac{1}{2}+y-\frac{V_{ss}^2}{4M_T}\tau_m y\exp(-\omega y)\right)
\end{aligned} \tag{C.11}$$

Once the integration is done, the expression becomes:

$$1 = \alpha\left(-\frac{2\beta}{\omega}+\left(1+\frac{2\beta}{\omega}\right)(1+\omega)^{-1/2}\right) \tag{C.12}$$

which results in this equation:

$$(1+\omega)^{1/2} = \frac{\omega+2\beta}{\omega/\alpha+2\beta} \tag{C.13}$$

Squaring the above equation, a third order polynomial in omega can be solved with the following solutions:

$$\begin{aligned}
\omega_0 &= 0 \\
\omega_\pm &= \frac{1+4\beta-\alpha^2}{2} \pm \frac{1}{2}\sqrt{((1-\alpha)^2[(1+\alpha)^2-8\alpha\beta]}
\end{aligned} \tag{C.14}$$

C.2.1 Type A solutions $\alpha > (1-\beta)^{-1}$

Type A solutions according to Van Saarloos' classification are unstable because $\omega_+ > 0$. Physically this corresponds to the the slope of the reaction rate curve with temperature being steeper than how the steady state velocity changes with steady state temperature:
$\frac{V}{T_b} > \frac{V_{ss}}{T_{ss}^b}$

C.2.2 Type B solutions $\alpha < (1-\beta)^{-1}$

Type B solutions according to Van Saarloos' Classification can be either stable or unstable. . However, unlike type A solutions, some of these solutions with $Re\omega > 0$ can also have an imaginary

component, which can be found in the region bounded by

$$\beta = \frac{\alpha - \alpha^{-1}}{4} \tag{C.15}$$

and

$$\beta = \frac{(\alpha + 1)^2}{8\alpha} \tag{C.16}$$

These are the parameters under which the temporal oscillations of the interface temperature can be observed.

C.2.3 Type C solutions $\alpha < 0$

These solutions are stable.

Bibliography

[1] K. R. Elder and Martin Grant. Modeling elastic and plastic deformations in nonequilibrium processing using phase field crystals. *Physical Review E*, 70(5):051605, November 2004.

[2] Joel Berry, K. R. Elder, and Martin Grant. Melting at dislocations and grain boundaries: A phase field crystal study. *Phys. Rev. B*, 77:224114, Jun 2008.

[3] N. Wang, R. Spatschek, and A. Karma. Multi-phase-field analysis of short-range forces between diffuse interfaces. *Phys. Rev. E*, 81(5):051601, May 2010.

[4] E Kroner and K H Anthony. Dislocations and disclinations in material structures: The basic topological concepts. *Annual Review of Materials Science*, 5(1):43–72, 1975.

[5] Jonathan Stolle and Nikolas Provatas. Characterizing solute segregation and grain boundary energy in a binary alloy phase field crystal modeling. 2012.

[6] John W Cahn. Nucleation on dislocations. *Acta Metallurgica*, 5(3):169 – 172, 1957.

[7] Adolf Götzberger. über die kristallisation aufgedampfter antimonschichten. *Zeitschrift fuŕ Physik*, 142(2):182–200, 1955.

[8] C.E. Wickersham, G. Bajor, and J.E. Greene. Impulse stimulated explosive crystallization of sputter deposited amorphous (in,ga)sb films. *Solid State Communications*, 27(1):17 – 20, 1978.

[9] A. Perio J. C. Pfister A. Izrael D. Bensahel, G. Auvert and P. Henoc. Impurity segregation during explosive crystallization of amorphous silicon. *Journal of Applied Physics*, 54(6):3485 – 3488, 1983.

[10] Wim Van Saarloos and John D. Weeks. Surface undulations in explosive crystallization: A nonlinear analysis of a thermal instability. *Physica D: Nonlinear Phenomena*, 12(13):279 – 294, 1984.

[11] Nikolas Provatas, Martin Grant, and K. R. Elder. Phase-field model for activated reaction fronts. *Phys. Rev. B*, 53:6263–6272, Mar 1996.

[12] K. R. Elder, Nikolas Provatas, Joel Berry, Peter Stefanovic, and Martin Grant. Phase-field crystal modeling and classical density functional theory of freezing. *Phys. Rev. B*, 75:064107, Feb 2007.

[13] Nana Ofori-Opoku, Jonathan Stolle, Zhi-Feng Huang, and Nikolas Provatas. Complex order parameter phase-field models derived from structural phase-field-crystal models. *Phys. Rev. B*, 88:104106, Sep 2013.

[14] Vahid Fallah, Jonathan Stolle, Nana Ofori-Opoku, Shahrzad Esmaeili, and Nikolas Provatas. Phase-field crystal modeling of early stage clustering and precipitation in metal alloys. *Phys. Rev. B*, 86:134112, Oct 2012.

[15] D.-H Yeon, Z.-F Huang, K.R Elder, and K Thornton. Density-amplitude formulation of the phase-field-crystal model for two-phase coexistence in two and three dimensions. *Philosophical Magazine*, 90:237–263, 2010.

[16] Jonathan Stolle and Nikolas Provatas. Characterizing solute segregation and grain boundary energy in binary alloy phase field crystal models. *Computational Materials Science*, In Press, 2013.

[17] Liz Rowan. The structural disjoining potential of grain boundary premelting in binary alloys using phase crystal model. Master's thesis, McMaster University, 2013.

[18] Vahid Fallah, Nana Ofori-Opoku, Jonathan Stolle, Nikolas Provatas, and Shahrzad Esmaeili. Simulation of early-stage clustering in ternary metal alloys using the phase-field crystal method. *Acta Materialia*, 61(10):3653 – 3666, 2013.

[19] Robert Spatschek and Alain Karma. Amplitude equations for polycrystalline materials with interaction between composition and stress. *Phys. Rev. B*, 81(21):214201, Jun 2010.

[20] Gregory S. Rohrer. Grain boundary energy anisotropy: a review. *J. Mater. Sci.*, 46:58815895, 2011.

[21] E.D. Hondros and M. P. Seah. *Physical Metallurgy*, pages 855–930. Amsterdam, 3rd rev. and enl. edition, 1983.

[22] A. P. Sutton and R. W. Balluffi. *Interfaces in Crystalline Materials*, pages 138–139, 152–163, 174–181, 253–272, 286–318, 349–359, 409–412, 414–423, 435–438, 449–450, 560–563. Oxford University Press, USA, March 1995.

[23] Pavel Lejcek and Siegfried Hofmann. Thermodynamics and structural aspects of grain boundary segregation. *Critical Reviews in Solid State and Materials Sciences*, 20(1):1, 1995.

[24] A. Kirchner and B. Kieback. Thermodynamic model of alloy grain boundaries. *Scripta Materialia*, 64(5):406 – 409, 2011.

[25] Yasushi Shibuta, Shinya Takamoto, and Toshio Suzuki. Dependence of the grain boundary energy on the alloy composition in the bcc iron-chromium alloy: A molecular dynamics study. *Computational Materials Science*, 44(4):1025 – 1029, 2009.

[26] S. G. Mayr and D. Bedorf. Stabilization of cu nanostructures by grain boundary doping with bi: Experiment versus molecular dynamics simulation. *Phys. Rev. B*, 76(2):024111, Jul 2007.

[27] J. J Hoyt. *Phase Transformations*, pages 180–190. McMaster Innovation Press, 2010.

[28] Jian Luo. Stabilization of nanoscale Quasi-Liquid interfacial films in inorganic materials: A review and critical assessment. *Critical Reviews in Solid State and Materials Sciences*, 32(1):67, 2007.

[29] Y. Mishin, W.J. Boettinger, J.A. Warren, and G.B. McFadden. Thermodynamics of grain boundary premelting in alloys. i. phase-field modeling. *Acta Materialia*, 57(13):3771 – 3785, 2009.

[30] Eva-Maria Steyskal, Bernd Oberdorfer, Wolfgang Sprengel, Michael Zehetbauer, Reinhard Pippan, and Roland Würschum. Direct experimental determination of grain boundary excess volume in metals. *Phys. Rev. Lett.*, 108:055504, Jan 2012.

[31] N.A Gjostein and F.N Rhines. Absolute interfacial energies of [001] tilt and twist grain boundaries in copper. *Acta Metallurgica*, 7(5):319 – 330, 1959.

[32] K.T. Aust and B. Chalmers. Metal interfaces. *American Society for Metals*, 1:153, 1952.

[33] W. T. Read and W. Shockley. Dislocation models of crystal grain boundaries. *Phys. Rev.*, 78(3):275–289, May 1950.

[34] Stephen M. Foiles. Evaluation of harmonic methods for calculating the free energy of defects in solids. *Phys. Rev. B*, 49(21):14930–14938, Jun 1994.

[35] D. Udler and D. N. Seidman. Grain boundary and surface energies of fcc metals. *Phys. Rev. B*, 54(16):R11133–R11136, Oct 1996.

[36] G. B. McFadden and A. A. Wheeler. On the gibbs adsorption equation and diffuse interface models. *Proceedings of the Royal Society of London. Series A: Mathematical, Physical and Engineering Sciences*, 458(2021):1129–1149, 2002.

[37] J.D. Rittner, D. Udler, and D.N. Seidman. Solute-atom segregation at symmetric twist and tilt boundaries in binary metallic alloys on an atomic-scale. *Interface Science*, 4(1-2):65–80, 1997.

[38] Jesper Mellenthin, Alain Karma, and Mathis Plapp. Phase-field crystal study of grain-boundary premelting. *Physical Review B*, 78(18):184110, 2008.

[39] K. R. Elder, Mark Katakowski, Mikko Haataja, and Martin Grant. Modeling elasticity in crystal growth. *Physical Review Letters*, 88(24):245701–1–4, 2002.

[40] A. Jaatinen, C. V. Achim, K. R. Elder, and T. Ala-Nissila. Thermodynamics of bcc metals in phase-field-crystal models. *Phys. Rev. E*, 80:031602, Sep 2009.

[41] Michael Greenwood, Chad Sinclair, and Matthias Militzer. Phase field crystal model of solute drag. *Acta Materialia*, 60(16):5752 – 5761, 2012.

[42] B. Straumal and B. Baretzky. Grain boundary phase transitions and their influence on properties of polycrystals. *Interface Science*, 12(2-3):147–155, 2004.

[43] A. M. Alsayed, M. F. Islam, J. Zhang, P. J. Collings, and A. G. Yodh. Premelting at defects within bulk colloidal crystals. *Science*, 309(5738):1207–1210, 2005.

[44] A.B. Straumal, B.S. Bokstein, A.L. Petelin, B.B. Straumal, B. Baretzky, A.O. Rodin, and A.N. Nekrasov. Apparently complete grain boundary wetting in cuin alloys. *Journal of Materials Science*, 47(24):8336–8343, 2012.

[45] Ryoichi Kikuchi and John W. Cahn. Grain-boundary melting transition in a two-dimensional lattice-gas model. *Phys. Rev. B*, 21:1893–1897, Mar 1980.

[46] M. Rappaz, A. Jacot, and W.J. Boettinger. Last-stage solidification of alloys: Theoretical model of dendrite-arm and grain coalescence. *Metallurgical and Materials Transactions A*, 34(3):467–479, 2003.

[47] G. Ciccotti, M. Guillopé, and V. Pontikis. High-angle grain-boundary premelting transition: A molecular-dynamics study. *Phys. Rev. B*, 27:5576–5585, May 1983.

[48] J. J. Hoyt, David Olmsted, Saryu Jindal, Mark Asta, and Alain Karma. Method for computing short-range forces between solid-liquid interfaces driving grain boundary premelting. *Phys. Rev. E*, 79:020601, Feb 2009.

[49] Saryu J. Fensin, David Olmsted, Dorel Buta, Mark Asta, Alain Karma, and J. J. Hoyt. Structural disjoining potential for grain-boundary premelting and grain coalescence from molecular-dynamics simulations. *Phys. Rev. E*, 81:031601, Mar 2010.

[50] H. Song, S.J. Fensin, M. Asta, and J.J. Hoyt. A molecular dynamics simulation of (1 1 0) surface premelting in ni. *Scripta Materialia*, 63(1):128 – 131, 2010.

[51] P.L. Williams and Y. Mishin. Thermodynamics of grain boundary premelting in alloys. ii. atomistic simulation. *Acta Materialia*, 57(13):3786 – 3794, 2009.

[52] David L. Olmsted, Dorel Buta, Ari Adland, Stephen M. Foiles, Mark Asta, and Alain Karma. Dislocation-pairing transitions in hot grain boundaries. *Phys. Rev. Lett.*, 106:046101, Jan 2011.

[53] Ari Adland, Alain Karma, Robert Spatschek, Dorel Buta, and Mark Asta. Phase-field-crystal study of grain boundary premelting and shearing in bcc iron. *Phys. Rev. B*, 87:024110, Jan 2013.

[54] R. Spatschek, A. Adland, and A. Karma. Structural short-range forces between solid-melt interfaces. *Phys. Rev. B*, 87:024109, Jan 2013.

[55] Tara Power. Structural disjoining potential of grain boundary premelting in aluminum-magnesium via monte carlo simulations. Master's thesis, McMaster University, 2013.

[56] J. W. Christian. *Phase-Field Methods in Materials Science*, pages 772–785. Pergammon, Oxford, 3rd edition, 2002.

[57] S. Esmaeili, D. Vaumousse, M. W. Zandbergen, W. J. Poole, A. Cerezo, and D. J. Lloyd. A study on the early-stage decomposition in the almgsicu alloy aa6111 by electrical resistivity and three-dimensional atom probe. *Philosophical Magazine*, 87(25):3797–3816, 2007.

[58] R.K.W. Marceau, G. Sha, R.N. Lumley, and S.P. Ringer. Evolution of solute clustering in alcumg alloys during secondary ageing. *Acta Materialia*, 58(5):1795 – 1805, 2010.

[59] R.K.W. Marceau, G. Sha, R. Ferragut, A. Dupasquier, and S.P. Ringer. Solute clustering in alcumg alloys during the early stages of elevated temperature ageing. *Acta Materialia*, 58(15):4923 – 4939, 2010.

[60] Aniruddha Biswas, Donald J. Siegel, C. Wolverton, and David N. Seidman. Precipitates in al-cu alloys revisited: Atom-probe tomographic experiments and first-principles calculations of compositional evolution and interfacial segregation. *Acta Materialia*, 59(15):6187 – 6204, 2011.

[61] J.B.M. Nuyten. Quenched structures and precipitation in al-cu alloys with and without trace additions of cd. *Acta Metallurgica*, 15(11):1765 – 1770, 1967.

[62] E Ozawa and H Kimura. Excess vacancies and the nucleation of precipitates in aluminum-silicon alloys. *Acta Metallurgica*, 18(9):995 – 1004, 1970.

[63] A. Somoza, M. P. Petkov, K. G. Lynn, and A. Dupasquier. Stability of vacancies during solute clustering in al-cu-based alloys. *Phys. Rev. B*, 65:094107, Feb 2002.

[64] Vahid Fallah, Andreas Korinek, Nana Ofori-Opoku, Nikolas Provatas, and Shahrzad Esmaeili. Atomistic investigation of clustering phenomenon in the al-cu system: three-dimensional phase field crystal simulation and hrtem-hrstem characterization. *Acta Materialia*, 61(17):6372 – 6386, 2013.

[65] F.C. Larché and J.W. Cahn. Overview no. 41 the interactions of composition and stress in crystalline solids. *Acta Metallurgica*, 33(3):331 – 357, 1985.

[66] Derek Hull and D. J. Bacon. *Introduction to Dislocations*, pages 71–73. Elsvier Science, Burlington, 5th edition, 2011.

[67] J. J Hoyt. *Phase Transformations*, pages 56–60. McMaster Innovation Press, 2010.

[68] K.C. King, P.W. Voorhees, G.B. Olson, and T. Mura. Solute distribution around a coherent precipitate in a multicomponent alloy. *Metallurgical Transactions A*, 22(10):2199–2210, 1991.

[69] J. J Hoyt. *Phase Transformations*, pages 71–102. McMaster Innovation Press, 2010.

[70] C. Grigoropoulos, M. Rogers, S. H. Ko, A. A. Golovin, and B. J. Matkowsky. Explosive crystallization in the presence of melting. *Phys. Rev. B*, 73:184125, May 2006.

[71] G. Gore. On a peculiar phnomenon in the electro-deposition of antimony. *Philosophical Magazine Series 4*, 9(56):73–74, 1855.

[72] C. C. Coffin and Stuart Johnston. Studies on explosive antimony. i. the microscopy of polished surfaces. *Proceedings of the Royal Society of London. Series A*, 146(858):564–570, 1934.

[73] H. S. Chen and D. Turnbull. Specific heat and heat of crystallization of amorphous germanium. *Journal of Applied Physics*, 40(10):4214 – 4215, 1969.

[74] Russell Messier Takeshi Takamori and Rustum Roy. New noncrystalline germanium which crystallizes "explosively" at room temperature. *Applied Physics Letters*, 20(5):201 – 203, 1972.

[75] H. J. Zeiger, John C. C. Fan, B. J. Palm, R. L. Chapman, and R. P. Gale. Amorphous-crystalline boundary dynamics in cw laser crystallization. *Phys. Rev. B*, 25:4002–4018, Mar 1982.

[76] A. Georges V. T. Nguyen P. Henoc F. Morin G. Auvert, D. Bensahel and P. Coissard. Influence of cw laser scan speed in solidphase crystallization of amorphous si film on si3n4/glass substrate. *Applied Physics Letters*, 38(8):613–615, 1981.

[77] G.L. Olson, S.A. Kokorowski, J.A. Roth, and L.D. Hess. Laser-induced solid phase crystallization in amorphous silicon films. *MRS Proceedings*, 13, 1 1982.

[78] Liliya Nikolova, Thomas LaGrange, Mark J. Stern, Jennifer M. MacLeod, Bryan W. Reed, Heide Ibrahim, Geoffrey H. Campbell, Federico Rosei, and Bradley J. Siwick. Complex crystallization dynamics in amorphous germanium observed with dynamic transmission electron microscopy. *Phys. Rev. B*, 87:064105, Feb 2013.

[79] Yohei Endo Shogo Nishizaki Keisuke Ohdaira, Tomoko Fujiwara and Hideki Matsumura. Explosive crystallization of amorphous silicon films by flash lamp annealing. *Journal of Applied Physics*, 106(4):044907, 2009.

[80] B. W. Reed M. J. Stern N. D. Browning G. H. Campbell J.-C. Kieffer B. J. Siwick L. Nikolova, T. LaGrange and F. Rosei. Nanocrystallization of amorphous germanium films observed with nanosecond temporal resolution. *Applied Physics Letters*, 97:203102, 2010.

[81] Wim van Saarloos and John D. Weeks. Surface undulations in explosive crystallization: A thermal instability. *Phys. Rev. Lett.*, 51:1046–1049, Sep 1983.

[82] Douglas A. Kurtze, Wim van Saarloos, and John D. Weeks. Front propagation in self-sustained and laser-driven explosive crystal growth: Stability analysis and morphological aspects. *Phys. Rev. B*, 30:1398–1415, Aug 1984.

[83] Douglas A. Kurtze. Stability of incomplete explosive crystal growth. *Phys. Rev. B*, 34:1770–1774, Aug 1986.

[84] Qiuming Yu, Michael O. Thompson, and Paulette Clancy. Solidification kinetics in sige alloys. *Phys. Rev. B*, 53:8386–8397, Apr 1996.

[85] Erik J. Albenze, Michael O. Thompson, and Paulette Clancy. Atomistic computer simulation of explosive crystallization in pure silicon and germanium. *Phys. Rev. B*, 70:094110, Sep 2004.

[86] Erik J. Albenze and Paulette Clancy. Interface response functions for amorphous and crystalline si and the implications for explosive crystallization. *Molecular Simulation*, 31(1):11–24, 2005.

[87] Erik J. Albenze, Michael O. Thompson, and Paulette Clancy. Molecular dynamics study of explosive crystallization of sige and boron-doped sige alloys. *Industrial & Engineering Chemistry Research*, 45(16):5628–5639, 2006.

[88] M. Posselt and A. Gabriel. Atomistic simulation of amorphous germanium and its solid phase epitaxial recrystallization. *Phys. Rev. B*, 80:045202, Jul 2009.

[89] W. Kurz and R. Trivedi. Overview no. 87 solidification microstructures: Recent developments and future directions. *Acta Metallurgica et Materialia*, 38(1):1 – 17, 1990.

[90] M. Carrard, M. Gremaud, M. Zimmermann, and W. Kurz. About the banded structure in rapidly solidified dendritic and eutectic alloys. *Acta Metallurgica et Materialia*, 40(5):983 – 996, 1992.

[91] Ivan L'Heureux. Oscillatory zoning in crystal growth: A constitutional undercooling mechanism. *Phys. Rev. E*, 48:4460–4469, Dec 1993.

[92] Alain Karma and Armand Sarkissian. Interface dynamics and banding in rapid solidification. *Phys. Rev. E*, 47:513–533, Jan 1993.

[93] A. Karma, W.-J. Rappel, B.C. Fuh, and R. Trivedi. Model of banding in diffusive and convective regimes during directional solidification of peritectic systems. *Metallurgical and Materials Transactions A*, 29(5):1457–1470, 1998.

[94] Massimo Conti. Transition from dendritic to planar growth and banded structure formation in rapidly solidified alloys. *Phys. Rev. E*, 58:6101–6108, Nov 1998.

[95] M. Conti. Interface dynamics, instabilities, and solute bands in rapid directional solidification. *Phys. Rev. E*, 58:2071–2078, Aug 1998.

[96] Alexander L. Korzhenevskii, Richard Bausch, and Rudi Schmitz. Capillary-wave description of rapid directional solidification. *Phys. Rev. E*, 85:021605, Feb 2012.

[97] Peter Stefanovic, Mikko Haataja, and Nikolas Provatas. Phase-field crystals with elastic interactions. *Phys. Rev. Lett.*, 96(22):225504, Jun 2006.

[98] Peter Stefanovic, Mikko Haataja, and Nikolas Provatas. Phase field crystal study of deformation and plasticity in nanocrystalline materials. *Phys. Rev. E*, 80(4):046107, Oct 2009.

[99] Heike Emmerich, Hartmut Löwen, Raphael Wittkowski, Thomas Gruhn, Gyula I. Tóth, György Tegze, and László Gránásy. Phase-field-crystal models for condensed matter dynamics on atomic length and diffusive time scales: an overview. *Advances in Physics*, 61(6):665–743, 2012.

[100] Akusti Jaatinen. *Modeling Materials with Phase Field Crystal Models*. PhD thesis, Aalto University, 2010.

[101] Kuo-An Wu and Alain Karma. Phase-field crystal modeling of equilibrium bcc-liquid interfaces. *Phys. Rev. B*, 76:184107, Nov 2007.

[102] Ari Adland, Alain Karma, Robert Spatschek, Dorel Buta, and Mark Asta. Phase-field-crystal study of grain boundary premelting and shearing in bcc iron. *Phys. Rev. B*, 87:024110, Jan 2013.

[103] N. Pisutha-Arnond, V. W. L. Chan, K. R. Elder, and K. Thornton. Calculations of isothermal elastic constants in the phase-field crystal model. *Phys. Rev. B*, 87:014103, Jan 2013.

[104] Gyula I. Tóth, György Tegze, Tamás Pusztai, Gergely Tóth, and László Gránásy. Polymorphism, crystal nucleation and growth in the phase-field crystal model in 2d and 3d. *Journal of Physics: Condensed Matter*, 22(36):364101, 2010.

[105] R Backofen and A Voigt. A phase-field-crystal approach to critical nuclei. *Journal of Physics: Condensed Matter*, 22(36):364104, 2010.

[106] Gyula I. Tóth, György Tegze, Tamás Pusztai, and László Gránásy. Heterogeneous crystal nucleation: The effect of lattice mismatch. *Phys. Rev. Lett.*, 108:025502, Jan 2012.

[107] Sami Majaniemi, M. Nonomura, and Martin Grant. First-principles and phenomenological theories of hydrodynamics of solids. *Eur. Phys. J. B*, 66:329, 2008.

[108] Kuo-An Wu, Ari Adland, and Alain Karma. Phase-field-crystal model for fcc ordering. *Phys. Rev. E*, 81:061601, Jun 2010.

[109] Kuo-An Wu, Mathis Plapp, and Peter W Voorhees. Controlling crystal symmetries in phase-field crystal models. *Journal of Physics: Condensed Matter*, 22(36):364102, 2010b.

[110] Michael Greenwood, Nikolas Provatas, and Jörg Rottler. Free energy functionals for efficient phase field crystal modeling of structural phase transformations. *Phys. Rev. Lett.*, 105:045702, Jul 2010.

[111] Michael Greenwood, Jörg Rottler, and Nikolas Provatas. Phase-field-crystal methodology for modeling of structural transformations. *Phys. Rev. E*, 83:031601, Mar 2011.

[112] Joel Berry, Nikolas Provatas, Jörg Rottler, and Chad W. Sinclair. Defect stability in phase-field crystal models: Stacking faults and partial dislocations. *Phys. Rev. B*, 86:224112, Dec 2012.

[113] Michael Greenwood, Nana Ofori-Opoku, Jörg Rottler, and Nikolas Provatas. Modeling structural transformations in binary alloys with phase field crystals. *Phys. Rev. B*, 84:064104, Aug 2011.

[114] Srevatsan Muralidharan and Mikko Haataja. Phase-field crystal modeling of compositional domain formation in ultrathin films. *Phys. Rev. Lett.*, 105:126101, Sep 2010.

[115] Srevatsan Muralidharan, Raika Khodadad, Ethan Sullivan, and Mikko Haataja. Multilayer thin film growth on crystalline and quasicrystalline surfaces: A phase-field crystal study. *Phys. Rev. B*, 85:245428, Jun 2012.

[116] Harith Humadi, Jeffrey J. Hoyt, and Nikolas Provatas. Phase-field-crystal study of solute trapping. *Phys. Rev. E*, 87:022404, Feb 2013.

[117] K.R. Elder, K. Thornton, and J.J. Hoyt. The kirkendall effect in the phase field crystal model. *Philosophical Magazine*, 91(1):151–164, 2011.

[118] Nana Ofori-Opoku, Vahid Fallah, Michael Greenwood, Shahrzad Esmaeili, and Nikolas Provatas. Multicomponent phase-field crystal model for structural transformations in metal alloys. *Phys. Rev. B*, 87:134105, Apr 2013.

[119] K. R. Elder, Zhi-Feng Huang, and Nikolas Provatas. Amplitude expansion of the binary phase-field-crystal model. *Phys. Rev. E*, 81(1):011602, Jan 2010.

[120] Badrinarayan P. Athreya, Nigel Goldenfeld, and Jonathan A. Dantzig. Renormalization-group theory for the phase-field crystal equation. *Phys. Rev. E*, 74:011601, Jul 2006.

[121] Badrinarayan P. Athreya, Nigel Goldenfeld, Jonathan A. Dantzig, Michael Greenwood, and Nikolas Provatas. Adaptive mesh computation of polycrystalline pattern formation using a renormalization-group reduction of the phase-field crystal model. *Phys. Rev. E*, 76:056706, Nov 2007.

[122] Zhi-Feng Huang, K. R. Elder, and Nikolas Provatas. Phase-field-crystal dynamics for binary systems: Derivation from dynamical density functional theory, amplitude equation formalism, and applications to alloy heterostructures. *Phys. Rev. E*, 82(2):021605, Aug 2010.

[123] Zhi-Feng Huang and K. R. Elder. Morphological instability, evolution, and scaling in strained epitaxial films: An amplitude-equation analysis of the phase-field-crystal model. *Phys. Rev. B*, 81:165421, Apr 2010.

[124] Sami Majaniemi and Nikolas Provatas. Deriving surface-energy anisotropy for phenomenological phase-field models of solidification. *Phys. Rev. E*, 79:011607, Jan 2009.

[125] Nikolas Provatas and Sami Majaniemi. Phase-field-crystal calculation of crystal-melt surface tension in binary alloys. *Phys. Rev. E*, 82:041601, 2010.

[126] Niloufar Faghihi, Nikolas Provatas, K.R. Elder, Martin Grant, and Mikko Karttunen. Phase field crystal model for magneto-elasticity in isotropic ferromagnetic solids. 2013.

[127] Joel Berry, K. R. Elder, and Martin Grant. Simulation of an atomistic dynamic field theory for monatomic liquids: Freezing and glass formation. *Phys. Rev. E*, 77:061506, Jun 2008.

[128] Pak Yuen Chan, Nigel Goldenfeld, and Jon Dantzig. Molecular dynamics on diffusive time scales from the phase-field-crystal equation. *Phys. Rev. E*, 79:035701, Mar 2009.

[129] Joel Berry and Martin Grant. Modeling multiple time scales during glass formation with phase-field crystals. *Phys. Rev. Lett.*, 106:175702, Apr 2011.

[130] M. J. Robbins, A. J. Archer, U. Thiele, and E. Knobloch. Modeling the structure of liquids and crystals using one- and two-component modified phase-field crystal models. *Phys. Rev. E*, 85:061408, Jun 2012.

[131] Hartmut Löwen. A phase-field-crystal model for liquid crystals. *Journal of Physics: Condensed Matter*, 22(36):364105, 2010.

[132] Heike Emmerich, László Gránásy, and H. Löwen. Selected issues of phase-field crystal simulations. *Eur. Phys. J. Plus*, 126:102/1, 2011.

[133] A J Archer. Dynamical density functional theory for dense atomic liquids. *Journal of Physics: Condensed Matter*, 18(24):5617, 2006.

[134] Nikolas Provatas and Ken Elder. *Phase-Field Methods in Materials Science*, pages 154–176. Wiley-VCH, Weinheim, Germany, 2010.

[135] Nikolas Provatas and Ken Elder. *Phase-Field Methods in Materials Science*, pages 177–186. Wiley-VCH, Weinheim, Germany, 2010.

[136] Ingo Steinbach. Phase-field models in materials science. *Modelling and Simulation in Materials Science and Engineering*, 17(7):073001, 2009.

[137] Michael Greenwood, Jeffrey J. Hoyt, and Nikolas Provatas. Competition between surface energy and elastic anisotropies in the growth of coherent solid-state dendrites. *Acta Materialia*, 57(9):2613 – 2623, 2009.

[138] Tara Power, Elizabeth Rowan, Jonathan Stolle, Jeff Hoyt, and Nikolas Provatas. Comparing monte carlo and phase field crystal models of grain boundary premelting, draft in progress.

[139] James M. Howe. *Interfaces in Materials: Atomic Structure, Thermodynamics and Kinetics of Solid-Vapor, Solid-Liquid and Solid-Solid Interfaces*, page 408. Wiley-Interscience, February 1997.

[140] James A. Warren, Ryo Kobayashi, Alexander E. Lobkovsky, and W. Craig Carter. Extending phase field models of solidification to polycrystalline materials. *Acta Materialia*, 51(20):6035 – 6058, 2003.

[141] A. Jaatinen, C. V. Achim, K. R. Elder, and T. Ala-Nissila. Phase eld crystal study of symmetric tilt grain boundaries of iron. 30(1-3):169 176.

[142] Jeff Hoyt. Private communication.

[143] John W. Cahn and John E. Hilliard. Free energy of a nonuniform system. i. interfacial free energy. *Acta Metallurgica*, 28:258 – 267, 1957.

[144] K. R. Elder, Martin Grant, Nikolas Provatas, and J. M. Kosterlitz. Sharp interface limits of phase-field models. *Phys. Rev. E*, 64:021604, Jul 2001.

[145] Nikolas Provatas. Private communication.

[146] Nikolas Provatas and Ken Elder. *Phase-Field Methods in Materials Science*, pages 23–27. Wiley-VCH, Weinheim, Germany, 2010.

[147] Jörg Rottler, Michael Greenwood, and Benedikt Ziebarth. Morphology of monolayer films on quasicrystalline surfaces from the phase field crystal model. *Journal of Physics: Condensed Matter*, 24(13):135002, 2012.

[148] K. R. Elder, Zhi-Feng Huang, and Nikolas Provatas. Amplitude expansion of the binary phase-field-crystal model. *Phys. Rev. E*, 81(1):011602, Jan 2010.

[149] György Tegze, Gurvinder Bansel, Gyula I. Tóth, Tamás Pusztai, Zhongyun Fan, and László Gránásy. Advanced operator splitting-based semi-implicit spectral method to solve the binary phase-field crystal equations with variable coefficients. *Journal of Computational Physics*, 228(5):1612 – 1623, 2009.